Volume 65C
Number 3
July–September 1961

Engineering and Instrumentation

U.S. DEPARTMENT OF COMMERCE

SECTION C

JOURNAL OF RESEARCH

NATIONAL BUREAU OF STANDARDS

Journal of Research

of the

National Bureau of Standards

C. Engineering and Instrumentation

JULY–SEPT. • 1961

VOLUME • 65C

NUMBER • 3

Editor: W. A. Wildhack

Associate Editors: G. F. Montgomery, R. B. Jacobs

Publication dates:
Feb. 15, May 15, Aug. 15, Nov. 15, 1961

JOURNAL OF RESEARCH

The National Bureau of Standards Journal of Research reports research and development in the fields of activity shown at right. Also included from time to time are survey articles on topics closely related to the Bureau's scientific and technical program.

The Journal is published in four separate sections as follows:

A. Physics and Chemistry

Contains papers of interest primarily to scientists working in these fields. Issued six times a year. Annual subscription: domestic, $4.00; foreign, $4.75

B. Mathematics and Mathematical Physics

Presents studies and compilations designed mainly for the mathematician and the theoretical physicist. Issued quarterly. Annual subscription: domestic, $2.25; foreign, $2.75.

C. Engineering and Instrumentation

Reports research and development results of interest chiefly to the engineer and the applied scientist. Issued quarterly. Annual subscription: domestic, $2.25; foreign, $2.75.

D. Radio Propagation

Reports work in radio propagation physics and upper atmospheric research. Issued six times a year. Annual subscription: domestic, $4.00; foreign, $4.75.

Functions and Activities

The functions of the National Bureau of Standards are set forth in the Act of Congress, March 3, 1901, as amended. These include the development and maintenance of the national standards of measurement and the provision of means and methods for making measurements consistent with these standards; the determination of physical constants and properties of materials; the development of methods and instruments for testing materials, devices, and structures; advisory services to Government agencies on scientific and technical problems; invention and development of devices to serve special needs of the Government; and the development of standard practices, codes, and specifications. The work includes basic and applied research, development, engineering, instrumentation, testing, evaluation, calibration services, and various consultation and information services. The Bureau also serves as the Federal technical research center in a number of specialized fields. The scope of activities of the National Bureau of Standards is suggested in the following listing of the divisions and sections engaged in technical work.

Washington, D.C.

Electricity. Resistance and Reactance. Electrochemistry. Electrical Instruments. Magnetic Measurements. Dielectrics.

Metrology. Photometry and Colorimetry. Refractometry. Photographic Research. Length. Engineering Metrology. Mass and Scale. Volumetry and Densimetry.

Heat. Temperature Physics. Heat Measurements. Cryogenic Physics. Equation of State. Statistical Physics.

Radiation Physics. X-Ray. Radioactivity. Radiation Theory. High Energy Radiation. Radiological Equipment. Nucleonic Instrumentation. Neutron Physics.

Analytical and Inorganic Chemistry. Pure Substances. Spectrochemistry. Solution Chemistry. Standard Reference Materials. Applied Analytical Research.

Mechanics. Sound. Pressure and Vacuum. Fluid Mechanics. Engineering Mechanics. Rheology. Combustion Controls.

Organic and Fibrous Materials. Rubber. Textiles. Paper. Leather. Testing and Specifications. Polymer Structure. Plastics. Dental Research.

Metallurgy. Thermal Metallurgy. Chemical Metallurgy. Mechanical Metallurgy. Corrosion. Metal Physics. Electrodeposition.

Mineral Products. Engineering Ceramics. Glass. Refractories. Enameled Metals. Crystal Growth. Physical Properties. Constitution and Microstructure.

Building Research. Structural Engineering. Fire Research. Mechanical Systems. Organic Building Materials. Codes and Safety Standards. Heat Transfer. Inorganic Building Materials.

Applied Mathematics. Numerical Analysis. Computation. Statistical Engineering. Mathematical Physics.

Data Processing Systems. Components and Techniques. Digital Circuitry. Digital Systems. Analog Systems. Applications Engineering.

Atomic Physics. Spectroscopy. Radiometry. Solid State Physics. Electron Physics. Atomic Physics.

Instrumentation. Engineering Electronics. Electron Devices. Electronic Instrumentation. Mechanical Instruments. Basic Instrumentation.

Physical Chemistry. Thermochemistry. Surface Chemistry. Organic Chemistry. Molecular Spectroscopy. Molecular Kinetics. Mass Spectrometry. Molecular Structure and Radiation Chemistry.

• Office of Weights and Measures.

Boulder, Colo.

Cryogenic Engineering. Cryogenic Equipment. Cryogenic Processes. Properties of Materials. Gas Liquefaction.

Ionosphere Research and Propagation. Low Frequency and Very Low Frequency Research. Ionosphere Research. Prediction Services. Sun-Earth Relationships. Field Engineering. Radio Warning Service.

Radio Propagation Engineering. Data Reduction Instrumentation. Radio Noise. Tropospheric Measurements. Tropospheric Analysis. Propagation-Terrain Effects. Radio-Meteorology. Lower Atmosphere Physics.

Radio Standards. High Frequency Electrical Standards. Radio Broadcast Service. Radio and Microwave Materials. Atomic Frequency and Time Interval Standards. Electronic Calibration Center. Millimeter-Wave Research. Microwave Circuit Standards.

Radio Systems. High Frequency and Very High Frequency Research. Modulation Research. Antenna Research. Navigation Systems. Space Telecommunications.

Upper Atmosphere and Space Physics. Upper Atmosphere and Plasma Physics. Ionosphere and Exosphere Scatter. Airglow and Aurora. Ionospheric Radio Astronomy.

U.S. DEPARTMENT OF COMMERCE
Luther H. Hodges, Secretary

NATIONAL BUREAU OF STANDARDS
A. V. Astin, Director

Order all publications from the Superintendent of Documents
U.S. Government Printing Office, Washington 25, D.C.

Use of funds for printing this publication approved by the Director of the Bureau of the Budget (June 19, 1961).

JOURNAL OF RESEARCH of the National Bureau of Standards—Engineering and Instrumentation
Vol. 65C, No. 3, July–September 1961

Prediction of Symptoms of Cavitation[1]

Robert B. Jacobs

(April 26, 1961)

An analysis which indicates some of the basic problems in cavitation and which may permit the prediction of cavitation characteristics of hydraulic equipment is presented. Some experimental results are discussed and are compared with the results of the analysis.

It is concluded that the analysis may be applicable to the prediction of symptoms of cavitation (changes in performance characteristics due to the presence of cavitation), but that more information related to metastability, nucleation, and vapor-phase dynamics is required.

1. Introduction

The prediction of cavitation in hydraulic equipment has been of interest to designers, manufacturers, and users for many years. Essentially all of the work in this area consists of testing which provides information that is applicable only to the fluid and equipment used in the tests. Investigations concerned with basic problems of cavitation have not been pursued as vigorously. The purpose of this paper is twofold: (1) To present an analysis which indicates some of the basic problems in cavitation and which may permit the prediction of cavitation characteristics, and (2) To discuss some experimental results which have been obtained and compare these with the results of the analysis.

Cavitation can occur in any type of hydraulic equipment in which the local static pressure can drop below the local vapor pressure, with a consequent formation of a vapor phase. It can occur in simple equipment such as a pipe and in the most complicated rotating machinery such as a pump or turbine.

Cavitation may be said to occur whenever a cavity forms in a liquid; in hydraulic equipment this cavity is usually filled with vapor from the surrounding liquid, or with a mixture of this vapor and gaseous impurities. Cavitation is frequently associated with certain symptoms. To some, cavitation exists as soon as one, or a very few, small vapor bubbles appear in the system; to others, cavitation exists if damage results; to a third group, cavitation exists when audible sounds are created. Clearly, the symptoms of interest must be specified if the concept of the "existence of cavitation" is to be significant.

This study will be concerned with cavitation that is sufficiently developed to cause a detectable alteration in the performance of equipment. Usually, an appreciable amount of vapor will form and there may be damage or noise. The symptoms of cavitation to be predicted are therefore changes in performance characteristics such as the head-capacity characteristics of a pump, and the calibration curve of a flow meter.

Examples of the empirical work concerning cavitation include that of Lindros [1],[2] Rankin [2], Weltmer [3], Hartman [4], and Wood [5]. In these investigations the application of the results is limited because an insight into the basic phenomena is not a primary objective of the experiments. A limited number of studies (e.g., Stahl and Stepanoff [6]) have attempted to gain more widely applicable information through more detailed considerations of the phenomena in systems where appreciable cavitation occurs. Here the influence of fluid properties on cavitation characteristics will be emphasized. (Fluids of significantly different properties are considered as different fluids, even though they have the same chemical composition.)

2. Analysis

Consider the device in figure 1, a piece of volumetric equipment such as a pump, venturi, or valve. Regardless of the liquid, the volume flow rates will be the same at the same non-cavitating operating point. Viscous and compressibility effects are assumed negligible (experiments by Richards [7], Purcell [8], and Martin [9] show that this assumption is acceptable). Under the same assumptions it follows (and experience confirms) that the static pressure gradients within the device (expressed in height of liquid) are essentially independent of the liquid. For example, in a non-cavitating pump operating at

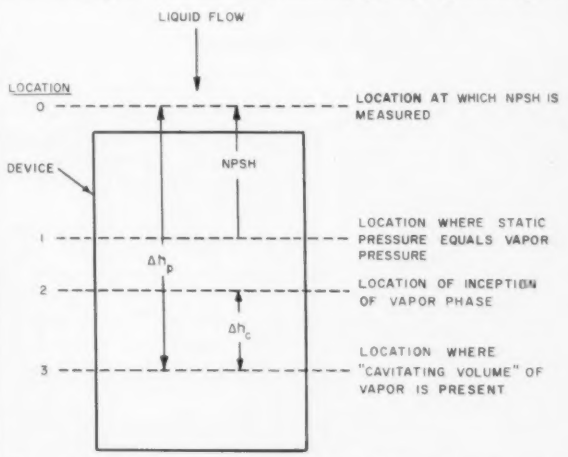

FIGURE 1. *Pertinent locations and head drops in a cavitating device.*

[1] Contribution from the Cryogenic Engineering Laboratory, National Bureau of Standards, Boulder, Colo.

[2] Figures in brackets indicate the literature references at the end of this paper.

a given speed and capacity, the static head-drop from the inlet to any point within the pump is independent of the liquid.

Consider the pressure level in the device to be lowered until a change in performance, due to cavitation, is incipient. This does not mean however that the vapor phase may not be well developed. Immediately before the symptoms of cavitation become evident the pressure and velocity distributions in the device (to location 2 in fig. 1 where the vapor phase is starting to form) do not depend upon the fluid. Thus, the differences in cavitation characteristics of different fluids, in the same device, are due to the differences in what occurs in those regions of the device that are downstream of the point of vapor inception. (Note that differences in nucleation characteristics of liquids can alter the location of the point of vapor inception for different fluids.) Attention is therefore focused on the differences in behavior of the fluids after the static pressure has dropped to, or perhaps somewhat below, the vapor pressure. The concern here is with what occurs between locations 2 and 3 in the device in figure 1; if stable equilibrium exists, locations 1 and 2 coincide.

The work of Stahl and Stepanoff [6] has the same purpose as this analysis, but the basic assumptions and therefore the final results of the two analyses differ. The major difference is that: In this analysis the head depression, below the pressure at which vaporization starts (not necessarily the vapor pressure), required to generate a "cavitating volume" of vapor is calculated, and it is assumed that differences in this head account for the variations in cavitation characteristics of different fluids. Stahl and Stepanoff calculate the vapor-to-liquid-volume ratio formed because of a given head depression, and assume that this ratio is an indication of cavitation characteristics. In addition, this analysis accounts for characteristics of the hydraulic device. Salemann [10] has discussed some aspects of the analysis presented here, as well as that of Stahl and Stepanoff.

2.1. Nomenclature

C=defined as $\left[C_{p_l}+v_l(1-T_l\beta_l)\left(\frac{dp}{dT}\right)\right]$, temperature coefficient for determining changes in the enthalpy of the liquid during the vaporization process.
C_p=isobaric specific heat of liquid.
h=specific enthalpy of fluid in region of cavitation.
N=pump speed.
p=pressure.
Q=pump capacity.
T=temperature.
u=mean fluid velocity in the region of cavitation.
V=volume of vapor per unit volume of mixture in region of cavitation when symptoms of cavitation are incipient.
v=specific volume.
x=quality of fluid in region of cavitation.
x_c=quality in the region of cavitation when symptoms of cavitation are incipient.
Δh_c=drop in head, measured in height of liquid, which is necessary to cause incipient symptoms of cavitation.
Δh_p=head drop experienced by a particle of fluid as it travels from the pump inlet to the region where cavitation is occurring.
Δp_c=pressure drop, after vaporization begins, necessary to cause sufficient flashing to produce incipient symptoms of cavitation.
β=coefficient of expansion, $\frac{1}{v}\left(\frac{\partial v}{\partial T}\right)_p$
δ=a function of ϕ and fluid properties, defined by eq (13).
λ=latent heat of vaporization.
ρ=density.
ϕ=defined as $V/(1-V)$, and is generally a function of design, operating point, and fluid.
χ=a function defined by eqs (7) and (8).

Subscripts: f refers to saturated liquid.
g refers to saturated vapor.
l refers to liquid.
v refers to vapor.
1, 2, 3, . . . n . . . used to identify fluids.

2.2. Derivation of Equations

Assuming that steady flow exists, heat transfer and shaft work are negligible during the flashing process, and that effects of force fields are negligible, the energy equation may be written

$$dh+d\left(\frac{u^2}{2}\right)=0.$$

Assume further that $h=h_l+x\lambda$, λ is constant, and that temperature is a function of pressure only. The energy equation becomes:

$$C\left(\frac{dT}{dp}\right)dp+\lambda dx+d\left(\frac{u^2}{2}\right)=0. \qquad (1)$$

The temperature coefficient, C, is defined as

$$\frac{dh_l}{dT}\equiv C\equiv\left[C_{p_l}+v_l(1-T_l\beta_l)\left(\frac{dp}{dT}\right)\right].$$

The derivative $\left(\frac{dT}{dp}\right)$ is the slope of the vapor-pressure curve *only if the liquid and vapor are in stable equilibrium;* generally, this is not the case, and the function $T(p)$ will depend upon those properties of the fluid which determine its ability to exist in metastable states. Also λ may not be exactly equal to the usual (stable equilibrium) latent heat of vaporization.

Assuming that steady state exists, and that viscous drag, changes in cross-sectional area, and changes in flow direction can be neglected during the flashing

process, the momentum equation can be written

$$dp+d(\rho u^2)=0. \tag{2}$$

The limitations introduced by the preceding assumptions may be relaxed in the application of the results of this analysis because the characteristics of different fluids passing through the same device are to be compared; it is anticipated that the fluid properties will be important and that the geometrical effects will tend to cancel out.

Using the previous assumptions, the continuity equation may be written

$$d(\rho u)=0. \tag{3}$$

Assuming that $1/\rho=[(1-x)v_l+xv_v]$ and that $x<<1$ or $v_l<<v_v$, and combining equations 1, 2, and 3, we have

$$dp=\frac{\lambda dx}{\left[v_l+xv_v-C\left(\frac{dT}{dp}\right)\right]}.$$

Note that v_l and v_v are the specific volumes of saturated liquid and vapor *only if the fluid is in stable equilibrium*. Assume that v_l, v_v, C, and $\left(\frac{dT}{dp}\right)$ are not functions of x. The preceding expression can then be integrated. Evaluating the constant of integration from the condition that $\Delta p=0$ when $x=0$, we obtain

$$\Delta p=\frac{\lambda}{v_v}\ln\left\{1+\frac{xv_v}{\left[v_l-C\left(\frac{dT}{dp}\right)\right]}\right\}. \tag{4}$$

It is important to note that the pressure at which $\Delta p=0$ is not the local vapor pressure, but depends upon the metastability and nucleation characteristics of the liquid. As these characteristics vary from liquid to liquid, it follows that the initial pressure, and hence the region in the device at which eq (4) is to be applied (i.e., between locations 2 and 3) depends upon the fluid. Equation (4) gives the change in pressure (Δp) which must occur if a fraction x of pure liquid is to vaporize by flashing.

Recall the basic premise that the symptoms of cavitation will occur when a "cavitating volume" of vapor forms in some region of the device. The location of the region and the volume of vapor depend upon the design of the device, the operating point, and probably upon the fluid; the location can be in the eye of an impeller, in a small localized low pressure region, or across a flow passage. If x_c is the quality in the cavitating region, then x_cv_v is the volume of vapor per unit mass of mixture in the region. Therefore

$$\Delta p_c=\frac{\lambda}{v_v}\ln\left\{1+\frac{x_cv_v}{\left[v_l-C\left(\frac{dT}{dp}\right)\right]}\right\}, \tag{5}$$

where Δp_c is the pressure drop, after vaporization begins, necessary to cause sufficient flashing to produce symptoms of cavitation.

Note that x_cv_v is the volume of vapor formed per unit *mass* of mixture. As equal volumes, not equal masses, of fluid flow through the device per unit time, we should be concerned with cavitating volumes of vapor per unit *volume* of mixture. Because of previous assumptions, we may write $(x_cv_v)\approx v_l[V/(1-V)]$, where V is the volume of vapor per unit volume of mixture in the cavitating region. (This V is the same as V' mentioned by Salemann [10].)

In eq (5), Δp_c is expressed in pressure units; i.e., force/area. This quantity could be directly compared from fluid to fluid if it were expressed in height of the flowing liquid. Substituting for (x_cv_v) and Δp_c in eq (5), we obtain

$$\Delta h_c=\frac{\lambda v_l}{v_v}\ln\left\{1+\frac{\frac{V}{(1-V)}}{\left[1-\frac{C}{v_l}\left(\frac{dT}{dp}\right)\right]}\right\}. \tag{6}$$

Equation (6) gives the drop in head Δh_c, measured in height of liquid, which would accompany the formation of a volume, V, of vapor per unit volume of mixture in the cavitating region, and which is therefore *necessary to initiate symptoms of cavitation.*

One is tempted to say that, for a given device and operating point (e.g., for a given speed, N, and capacity, Q, in a pump) the vapor volume ratio, V, may be the same for all fluids. In view of what has been said previously concerning metastability, nucleation, and vapor-phase dynamics, V is probably also a function of the fluid. Defining a function

$$\phi\ (\text{operating point, fluid})\equiv\frac{V}{(1-V)},$$

we have

$$\Delta h_c=\frac{\lambda v_l}{v_v}\ln\left\{1+\frac{\phi}{\left[1-\frac{C}{v_l}\left(\frac{dT}{dp}\right)\right]}\right\}, \tag{7}$$

where the function ϕ is to be determined either experimentally or by further analysis. The analysis presented by Wu [11] is an example of a theoretical approach which can predict the vapor volume ratio, V. Wu determines the effect of an attached region of vapor upon the lift and drag coefficients of a body in the flow passage. When the volume of this region is great enough to appreciably effect the lift and drag of the body, the performance of the device (e.g., pump) will be affected; this computed volume will then be the "vapor volume" in the cavitating region.

If no information is available regarding metastability, nucleation, and vapor-phase dynamics, the functions $T(p)$ and C cannot be predicted. In addition, if the fluids to be compared do not cavitate similarly (i.e., ϕ depends upon the fluid) eq (7) may be written in the form

$$\Delta h_c = \frac{\lambda v_l}{v_v} \chi \text{ (operating point, fluid)}, \quad (8)$$

where the function χ must be obtained by cavitation tests on the device at different operating points and with different fluids.

2.3. Application to Pumps

In order to indicate how the results obtained in the preceding section can be used, and to indicate some of the unresolved problems, the application of the results to the prediction of symptoms of cavitation in pumps will be discussed.

First it is necessary to relate the head drop, Δh_c, with some measurable quantity which is related to cavitation characteristics. The relations formulated here are primarily for illustrative purposes; their predictions compare poorly with the available experimental data. Possible reasons for this will be indicated as the formulation develops. Because of its wide use in pumping, the net positive suction head (NPSH) (i.e., the difference between the total pressure and the vapor pressure at the pump suction) will be used as the measurable quantity. During the remainder of this discussion, the term (NPSH) will mean the minimum NPSH required to suppress symptoms of cavitation.

One way to set up the required relationship is as follows: Consider the drop in head, Δh_p, experienced by a particle of liquid as it travels from the region where the NPSH is measured to the region where the cavitation is occurring. (See fig. 1.) For a given pump and given operating point, Δh_p is assumed to be about the same for all fluids if the pump is not cavitating. (It has been implied that the location of the cavitation does not depend upon the fluid, which is not generally true.) Assume that

$$\Delta h_p = (\text{NPSH}) - \Delta h_c. \quad (9)$$

(Both Δh_p and (NPSH) are positive, while Δh_c is negative.) Noting that NPSH represents the head drop from the inlet to the vapor pressure, and that Δh_c is reckoned, not from the vapor pressure, but from the pressure at which vaporization begins (refer to fig. 1), it is apparent that eq (9) is not exact. In addition, the alteration of the flow pattern within the pump due to the presence of the cavitating fluid is ignored. If, in spite of these limitations, Δh_p is assumed independent of the fluid being pumped, it follows that

$$(\text{NPSH})_1 - (\Delta h_c)_1 = (\text{NPSH})_2 - (\Delta h_c)_2 = (\text{NPSH})_n - (\Delta h_c)_n = \text{const.}, \quad (10)$$

where the subscripts 1, 2, . . . n . . . designate different fluids.

If the required fluid properties (λ, v_l, v_v, $T(p)$, etc.) are known, the prediction of the NPSH requirements for a given pump with any fluid by means of the results of this analysis requires the determination of two functions, Δh_p and ϕ (or χ). If both functions can be predicted theoretically no experimental work is required; this will probably not be the case.

A second relationship between NPSH and Δh_c is presented here because it approximately predicts some NPSH's which have been measured with liquid hydrogen, liquid nitrogen and liquid oxygen; its use has not yet been justified on any other basis. Because (NPSH) should decrease as $(-\Delta h_c)$ increases, we assume that

$$(\text{NPSH})(\Delta h_c) = a \text{ constant}. \quad (11)$$

Thus,

$$(\text{NPSH})_2 = (\text{NPSH})_1 \left\{ \frac{(\Delta h_c)_1}{(\Delta h_c)_2} \right\}. \quad (12)$$

The comments made above in connection with eqs (9 and 10), concerning the determination of the unknown functions, apply here also. Equations (7 or 8) and either (9, 10, 11, or 12) constitute pairs of relations which are examples of results of this analysis.

Due to the form of eq (7), the computation of the function ϕ from eq (10 or 12) involves the solution of a transcendental equation. In order to simplify computations an approximation to eq (7), based upon the assumption that

$$\phi < \left| \left[1 - \frac{C}{v_l} \left(\frac{dT}{dp} \right) \right] \right|$$

will be derived. The error introduced by the assumption is not more than a few percent, the magnitude of the error depending upon the magnitude of the function ϕ. Define:

$$\delta \equiv \frac{\phi}{\left[1 - \frac{C}{v_l} \left(\frac{dT}{dp} \right) \right]}. \quad (13)$$

If $|\delta| < 1$, we can write

$$\Delta h_c = \frac{\lambda v_l}{v_v} \delta \left[1 - \frac{1}{2}\delta + \frac{1}{3}\delta^2 - \ldots \frac{1}{n+1}\delta^n \ldots \right]. \quad (14)$$

The limitations of this restriction (i.e., $\delta < 1$) must be determined through numerical computation. As there is no information available describing a fluid which deviates from stable equilibrium, stable equilibrium properties must be used in the computations; $\left(\frac{dT}{dp} \right)$ is then the slope of the vapor pressure curve, and the other properties are for saturated liquid and vapor. The data required for the computation and the results for three important cryogenic fluids at atmospheric pressure are given in table 1. The computations show that the upper limit imposed upon the volume fraction of vapor in the cavitating region, V, to ensure the validity of eq (14) is very high. It is higher than any values for V computed from the cryogenic data obtained by the author, and much higher than any values computed by Salemann

[10]. This limit permits more than 99 percent of the cavitation region, with nitrogen or oxygen, to be filled with vapor, and more than 95 percent of the region to be filled with vapor in the case of hydrogen. Therefore this limitation on V (or ϕ) is probably unimportant.

Replacing eq (7) by eq (14) does not simplify computations because the transcendental function is merely replaced by its infinite series representation. A further development, which answers the following question, must be made: How many terms in eq (14) can be neglected without introducing unacceptable errors? The simplest computation results if only the first term is used. The maximum error introduced in the computed value of Δh_c by neglecting all terms except the first is $(1/2)\delta$; this error is plotted as a function of V in figure 2. Curves are shown for hydrogen, nitrogen, and oxygen at their normal boiling points, and for water at 70 °F. The error with water is negligible, even when 95 percent of the cavitation region is filled with vapor. With nitrogen and oxygen the error is only 6 percent when 95 percent of the cavitation region is filled with vapor, and is less than 1 percent when there is less than 75 percent vapor. The largest error, with hydrogen, is less than 10 percent when the volume of vapor is less than 82 percent. The values of V computed from our data and those computed by Salemann [10] indicate that the use of only the first term in eq (14) will yield reasonably accurate values of Δh_c. Therefore Δh_c will be computed from

$$\Delta h_c = \frac{\lambda v_l}{v_v}\,\delta = \frac{\lambda v_l}{v_v}\,\frac{\phi}{\left[1-\frac{C}{v_l}\left(\frac{dT}{dp}\right)\right]}. \qquad (15)$$

Substitution of eq (15) in eqs (10 and 12) gives the simplified formulations for the prediction of NPSH:

$$(\mathrm{NPSH})_2 = (\mathrm{NPSH})_1 + \left\{\frac{\lambda v_l}{v_v}\,\frac{\phi}{\left[1-\frac{C}{v_l}\left(\frac{dT}{dp}\right)\right]}\right\}_2 - \left\{\frac{\lambda v_l}{v_v}\,\frac{\phi}{\left[1-\frac{C}{v_l}\left(\frac{dT}{dp}\right)\right]}\right\}_1, \qquad (16)$$

and

$$(\mathrm{NPSH})_2 = (\mathrm{NPSH})_1 \frac{\left\{\frac{\lambda v_l}{v_v}\,\frac{\phi}{\left[1-\frac{C}{v_l}\left(\frac{dT}{dp}\right)\right]}\right\}_1}{\left\{\frac{\lambda v_l}{v_v}\,\frac{\phi}{\left[1-\frac{C}{v_l}\left(\frac{dT}{dp}\right)\right]}\right\}_2}. \qquad (17)$$

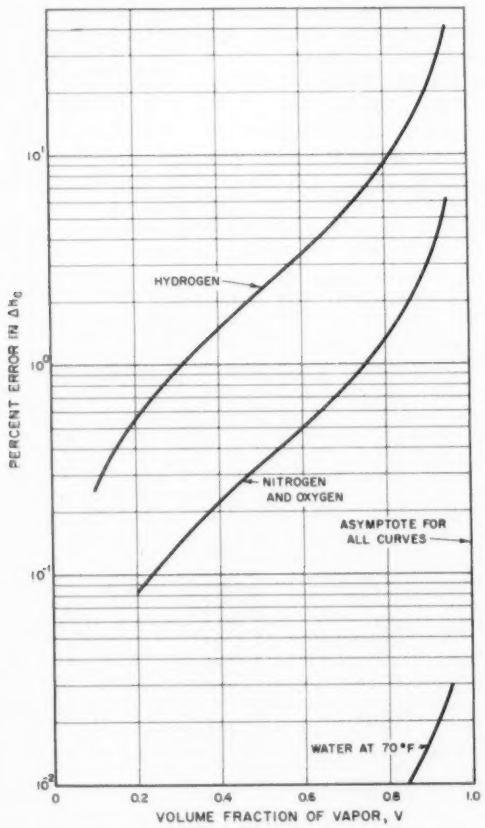

FIGURE 2. *Percent error in Δh_c due to use of only the first term in eq (14) versus the volume fraction of vapor (V) in the region of cavitation.*

TABLE 1. *Cryogenic fluid properties and data*

Quantity	Hydrogen	Nitrogen	Oxygen
Boiling point, °K	20.4	77.32	90.13
Latent heat of vaporization, λ, cal/g	106.5	47.6	50.8
Isobaric specific heat, C_p, cal/g °K	2.50	0.489	0.400
Specific volume of liquid, v_l, cm³/g	14.11	1.237	.871
Thermal expansion coefficient, β_l, 1/°K	0.0175	0.00580	.00738
Ratio of specific volume of saturated vapor to that of saturated liquid, v_g/v_l	50	183	265
Slope of vapor pressure curve $\left(\frac{dT}{dp}\right)_{v.p.}$ °K cm³/cal	132	383	336
Upper limit on V for eq (14) to be valid	0.958	0.994	0.994
Minimum NPSH required to suppress symptoms of cavitation, ft	0.167	7.0	10.6 to 15.7

Equation (16 or 17) would permit the prediction of the NPSH required to prevent symptoms of cavitation with fluid 2 if the NPSH requirements for fluid 1, the required fluid properties, the ϕ-functions were known, and if the assumed relations between NPSH and Δh_c (eqs 9 or 11) were valid.

If it is further assumed that ϕ is not a function of the fluid properties, eqs (16 and 17) simplify to

$$(\mathrm{NPSH})_2=(\mathrm{NPSH})_1+\phi(N,Q)\left\{\left[\frac{\lambda\frac{v_l}{v_v}}{1-\frac{C}{v_l}\left(\frac{dT}{dp}\right)}\right]_2-\left[\frac{\lambda\frac{v_l}{v_v}}{1-\frac{C}{v_l}\left(\frac{dT}{dp}\right)}\right]_1\right\} \quad (18)$$

and

$$(\mathrm{NPSH})_2=(\mathrm{NPSH})_1\frac{\left[\frac{\lambda\frac{v_l}{v_v}}{1-\frac{C}{v_l}\left(\frac{dT}{dp}\right)}\right]_1}{\left[\frac{\lambda\frac{v_l}{v_v}}{1-\frac{C}{v_l}\left(\frac{dT}{dp}\right)}\right]_2}\equiv(\mathrm{NPSH})_1\left(\frac{\tau_2}{\tau_1}\right), \quad (19)$$

respectively, where τ has been called the "cavitation tendency". The greater the cavitation tendency, the greater the required NPSH. The assumptions involved in the derivation of eqs (18 and 19) must be emphasized: the location of the cavitation region in a pump is independent of the fluid; the volume of vapor in this region, when cavitation symptoms arise, is independent of the fluid. The NPSH requirements which are to be compared are at the same operating points (i.e., the speed (N) and flow (Q) are the same for both fluids). In applying eq (18), the function, $\phi(N,Q)$ must be known, while application of eq (19) does not require a knowledge of the function.

3. Experimental Comparison

3.1. Centrifugal Pumping

In this section some experimental results which are pertinent to the analysis presented in the preceding section will be discussed. These indicate that the effects of the existence of metastable states, nucleation characteristics, and vapor-phase dynamics, are significant.

Only a meager amount of data is available to check the validity of eqs (18 and 19); some data have been reported by Salemann [10], and some have been obtained by the author. As no information is available concerning the deviation of the fluids from states of stable equilibrium during the tests, properties of saturated fluids are used in making comparisons.

One of the more drastic assumptions in the derivation of eq (18) is that ϕ is independent of the fluid being pumped. A straightforward way to check the equation is to substitute measured values of the minimum required NPSH and known values of fluid properties into the equation, and to determine if $\phi(N,Q)[=V/(1-V)]$ is constant. Salemann [10] did this for trichloromonofluoromethane, water, butane, and benzene, and found that ϕ varied from 0.25 to 1.

In order to compare eq (19) with the data, we shall rewrite it as

$$\frac{(\mathrm{NPSH})_2}{(\mathrm{NPSH})_1}=\frac{\tau_2}{\tau_1}=\left(\frac{\lambda_1}{\lambda_2}\right)\left(\frac{\left[\frac{v_v}{v_l}\right]_2}{\left[\frac{v_v}{v_l}\right]_1}\right)\left(\frac{\left[1-\frac{C}{v_l}\left(\frac{dT}{dp}\right)\right]_2}{\left[1-\frac{C}{v_l}\left(\frac{dT}{dp}\right)\right]_1}\right). \quad (20)$$

The validity of this expression can be checked by comparing the left-hand side (the experimental NPSH ratios) with the right-hand side (the theoretical cavitation-tendency ratios computed from fluid properties). The results of this comparison, using some of Salemann's data, are given in table 2. It is apparent that Salemann's data indicate that eqs (18 and 20) are not quantitatively valid, although the second equation may predict relative NPSH requirements for different fluids.

During the development of a hydrogen pumping system at this laboratory some crude NPSH data for hydrogen, nitrogen, and oxygen were obtained in a centrifugal pump designed for water. These data will be compared with eqs (18 and 20). Figure 3 is a schematic of the test apparatus used to obtain the data. The pump was a 10-stage submersible water pump rated at 3,450 rpm, 9.7 gpm, and 100 ft discharge head. The NPSH was determined by adding the liquid level above the pump suction,

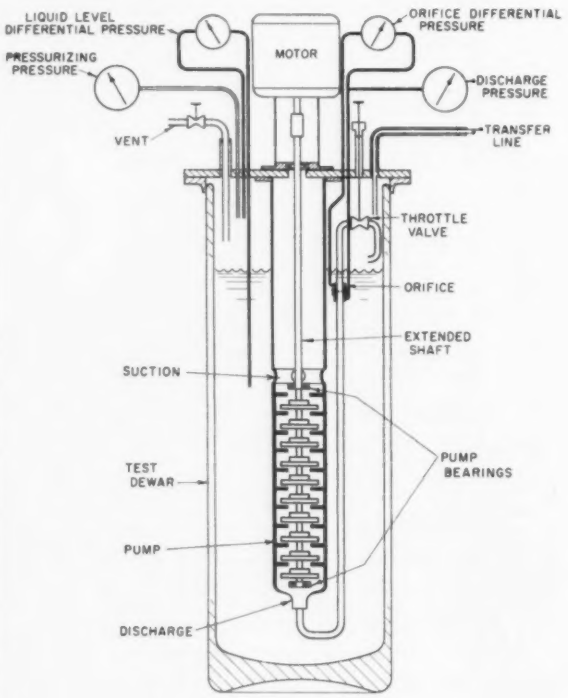

FIGURE 3. *Pump test setup.*

measured with a hydrostatic device, to the pressure in the vapor space above the liquid. Readings were taken immediately after pressurization to minimize the rise in temperature of the fluid. The pressure in the vapor space was reduced to atmospheric between each set of readings so that the temperature would drop to the saturation temperature. (In a later apparatus the NPSH was determined by a vapor-pressure device [12] and the state of the fluid at the pump suction was controlled by a heat exchanger and a standpipe.) As the liquid in the test Dewar was very agitated, its temperature was assumed to be uniform at the saturation temperature corresponding to atmospheric pressure.

TABLE 2. *Comparison of NPSH ratios to cavitation-tendency ratios for some of Salemann's [10] data*

Fluids	Experimental (NPSH) ratio	Theoretical cavitation tendency ratios
Freon-11 at 85 °F / Freon-11 at 120 °F	1.21	2.96
Water at 250 °F / Water at 300 °F	1.28	4.10
Water at 250 °F / Freon-11 at 120 °F	1.31	1.80

The minimum NPSH's required to suppress symptoms of cavitation were obtained by plotting suction-head depression curves: for a given operating point the capacity and discharge head were plotted as functions of NPSH. Above the minimum required NPSH both the capacity and discharge head are independent of NPSH, while below this value both quantities decrease very rapidly (with decreasing NPSH). The breaks in both curves occurred at the same NPSH and were readily located on the graphs. The symptom of cavitation was taken to be the break in the curves; the minimum NPSH required to suppress symptoms of cavitation is defined as the NPSH adjacent to, and above, the breaks in the suction-head depression curves. (Figure 4 is included to indicate the type of data obtained.)

The measured values of minimum NPSH required to suppress symptoms of cavitation are given in table 1. The low value for hydrogen has since been verified on other pumps by the author and by other investigators [13]. The minimum NPSH required for oxygen could only be bracketed between 10.6 ft and 15.7 ft because the tests were terminated when it was discovered that the liquid oxygen was eroding the pump.

Using data in table 1, we can compute values of ϕ from eq (18), and then values of V from the definition of ϕ. Equation (18) satisfies our hydrogen and nitrogen data if the volume fraction of vapor, V, is 0.053. It satisfies our nitrogen and oxygen data if the volume fraction of vapor is between 0.848 and 0.930. Thus, these data lead to the same conclusion as the data of Salemann: that the formulation expressed by eq (18) (in which ϕ is assumed to be independent of the fluid being pumped) will not predict NPSH requirements.

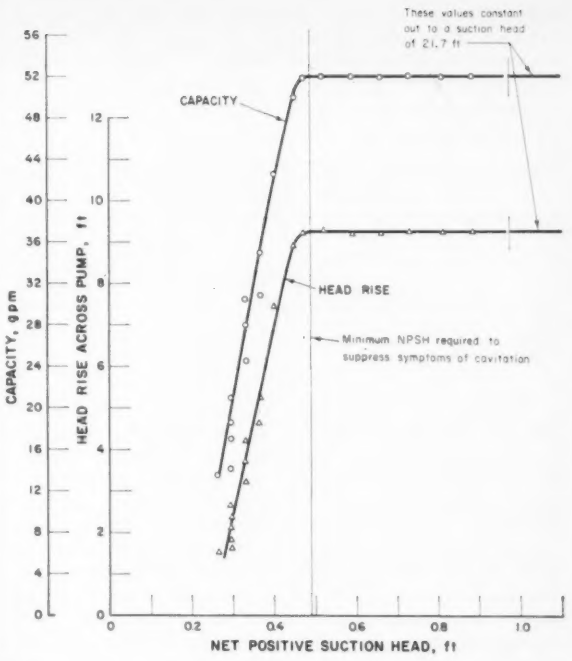

FIGURE 4. *Suction head depression run for liquid hydrogen in a single-stage, submerged booster pump.*

Speed: 5,450 rpm.
Rated flow.

The comparison between the cryogenic data and eq (20) is given in table 3. The theoretical predictions are in qualitative agreement with the experimental results. It is not possible to say whether more refined experiments would produce better or worse agreement.

Thus, both Salemann's data and the cryogenic data indicate that eq (18) is invalid, while both sets of data indicate that eq (20) may have some value in predicting NPSH requirements. It should be pointed out that Salemann's experimental (NPSH) requirements were those which permitted a 3 percent drop in discharge head, not those required to prevent symptoms of cavitation entirely. The less satisfactory correlation of Salemann's data with eq (20) may be due, in part, to the possibility that a 3 percent decrease in performance appreciably affects the flow throughout the whole pump, and thus seriously violates assumptions made in the derivation of the equation. It should be noted that the assumptions that Δh_p and ϕ are independent of fluid characteristics are very drastic, and may be responsible for the poor correlations presented above.

3.2. Flow Measurement

It has long been known (e.g., see Benjamin and Miller [14]) that even though a liquid passes through a region in which the static pressure falls below the vapor pressure, symptoms of cavitation need not occur. This means that even if the pressure at the

vena contracta of an orifice or at the throat of a venturi is below the vapor pressure, such devices may still be accurate flow meters. As this situation exists in many applications it is desirable to be able to predict when cavitation will affect the performance of a flow meter.

TABLE 3. *Comparison of NPSH ratios to cavitation tendency ratios for cryogenic liquids*

Fluids	Experimental (NPSH) ratio	Theoretical cavitation tendency ratios
Nitrogen: hydrogen	42	55
Oxygen: nitrogen	1.51 to 2.24	1.37
Oxygen: hydrogen	64 to 94	75.5

During an investigation to determine the behaviors of sharp-edged orifices with water, liquid nitrogen, and liquid hydrogen [7], it was not possible to produce cavitation symptoms as long as pure liquid entered the orifices. With liquid nitrogen, the pressures at the venae contractae were as much as 170 in. of liquid (4.9 psi) below the vapor pressure, while with liquid hydrogen the pressures at the venae contractae were as much as 192 in. of liquid (0.49 psi) below the vapor pressure. (These were the lowest pressures attainable with the apparatus.) The only way that symptoms of cavitation could be produced was to have two-phase flow entering the orifices; in many tests, even when two-phase flow entered the orifices, cavitation symptoms were not evident. Figure 5 is included here to show the results of some of the tests. Notice that only about one half of the nitrogen test points for which the upstream static pressure was below the vapor pressure show evidence of the presence of two-phase flow. Neither of the hydrogen points with upstream pressures below the vapor pressure appears to be affected by the two-phase flow. It is also interesting that orifice calibration curves obtained with water may be quite satisfactory for use with liquid nitrogen and liquid hydrogen.

The absence of cavitation symptoms when the static pressure is below the vapor pressure is due to the fact that appreciable time is required to form a significant vapor phase and that the fluid elements are not in the low pressure region for the required length of time. The time depends upon the ability of the fluid to persist in metastable states, on nucleation characteristics, and on bubble dynamics including heat and mass transfer. Thus the same basic problems are involved here as with cavitation in pumps, and the analysis presented in section 2 may be applicable.

3.3. Two-Phase Flow

Except in the region where the vapor phase is initiated, two-phase single-component fluid flow is not normally associated with cavitation. However, as metastability is one of the basic phenomena associated with cavitation and as it has been observed that metastable states can exist throughout two-phase, single-component fluid flows, some observations of these flows are presented here. The purpose in this section is to show that fluids can exist in metastable states for relatively long times; therefore, information of the types discussed in preceding sections would also be useful in this area.

The observations reported here were made in an apparatus designed to study steady, two-phase, single-component, fluid flow. This apparatus, described by Hatch [15], employs trichloromonofluoromethane. The curves in figure 6 show the existence of metastable states in the test section. The "measured temperature" curves were obtained from actual temperature measurements, while the "saturation temperature" curves were obtained from the saturation temperatures (taken from tables of thermodynamic data) corresponding to the measured pressures. It is obvious that the measured temperature lagged behind the saturation temperature, resulting in a superheated fluid. Here again, it can be concluded that vaporization does not occur rapidly enough to permit the attainment of stable equilibrium.

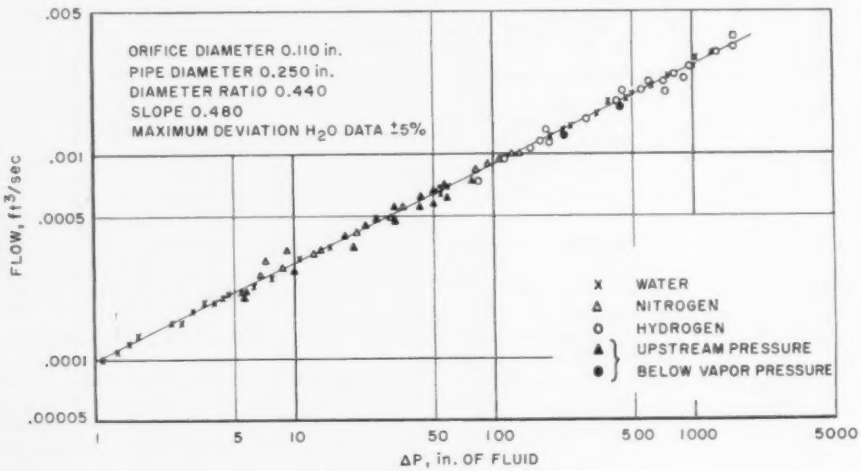

FIGURE 5. *Calibration curve.*

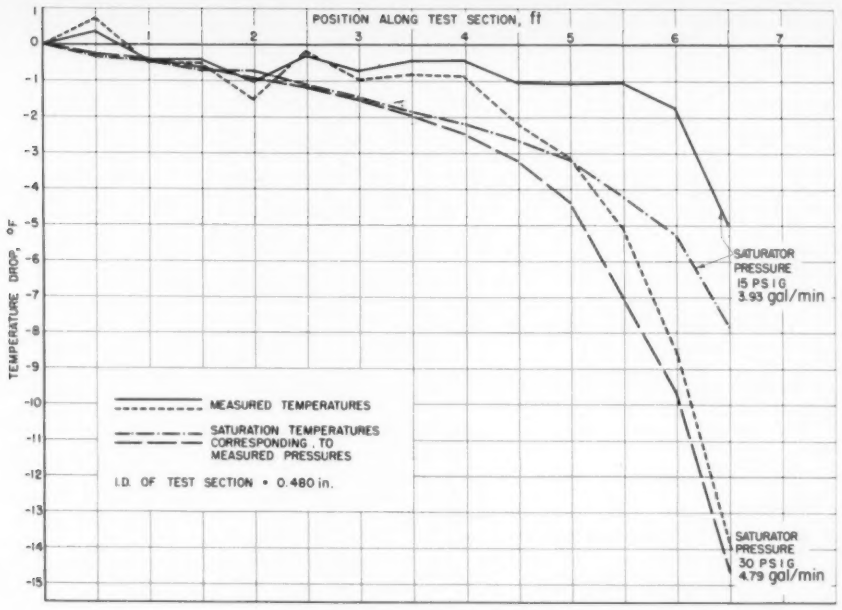
POSITION ALONG TEST SECTION, ft
TEMPERATURE DROP, °F
MEASURED TEMPERATURES
SATURATION TEMPERATURES CORRESPONDING TO MEASURED PRESSURES
I.D. OF TEST SECTION = 0.480 in.
SATURATOR PRESSURE 15 PS I G 3.93 gal/min
SATURATOR PRESSURE 30 PS I G 4.79 gal/min

FIGURE 6. *Two-phase flow data.*

Measurements indicating differences between measured and saturation temperatures of more than 3 °F were common. If the two-phase pressure drops are computed from the Martinelli and Nelson [16] correlation, the existence of these metastable states can cause errors up to 15 percent. These observations stress once again the desirability of research into metastable equilibria. (It should be pointed out that the spatial oscillations of the measured temperatures in figure 6 are believed to actually occur; no fault could be found with the thermometry. They may be due to the nozzle at the inlet to the test section.)

4. Conclusions

Observations of hydraulic equipment in which cavitation occurs show that the existence of metastable equilibrium states, nucleation characteristics, and vapor-phase dynamics can be important in the prediction of cavitation characteristics. Investigations of fluid characteristics which influence such behavior are therefore necessary if cavitation symptoms are to be predicted.

The meager data available indicate that an approach of the type presented in section 2 may be fruitful in predicting symptoms of cavitation. In addition to the types of investigations suggested in the preceding paragraph, theoretical and experimental studies concerned with the determination of the ϕ-function (or volume fraction of vapor in the cavitating region, V) should be continued. These studies should include work concerned with detailed pressure distribution within the equipment and the influence of the vapor region upon the detailed fluid mechanics of the equipment involved.

The qualitatively accurate predictions of the "Cavitation Tendency" concept suggest a desirability for further evaluation and refinement of this concept. However, the assumption that the ϕ-function is not dependent upon fluid properties appears to be too drastic and eqs (16) and (17) should be used instead of eqs (18) and (19) whenever the ϕ-function is known. As eq (16) was logically developed, while eq (17) was not, the former formulation is to be preferred; its poor correlation with available data may be due to the drastic assumption (i.e., ϕ independent of fluid) mentioned above. Finally it is suggested that, when sufficient information is available, eq (9) (and eqs (10) and (16)) should be modified to account for the delay in vapor formation which occurs between locations 1 and 2 in figure 1.

5. References

[1] E. E. Lindros, Actual NPSH requirements of centrifugal pumps compared to NPSH requirements as determined by laboratory tests, Presented at the ASME Cavitation Symposium, March 6–9, 1960, Rice Hotel, Houston, Texas.

[2] D. R. Rankin, Effect of varying available NPSH on the head-capacity curve of high specific speed pumps, Presented at the ASME Cavitation Symposium, March 6–9, 1960, Rice Hotel, Houston, Texas.

[3] W. W. Weltmer, The effects of air on the determination of critical NPSH, Presented at the ASME Cavitation Symposium, March 6–9, 1960, Rice Hotel, Houston, Texas.

[4] M. J. Hartmann and R. F. Soltes, Observation of the cavitation in a low hub-tip ratio axial flow pump, Paper No. 60–HYD–14, Presented at the ASME Cavitation Symposium, March 6–9, 1960, Rice Hotel, Houston, Texas.

593949—61——2

[5] G. M. Wood, J. S. Murphy, and J. Farquhar, An experimental study of cavitation in a mixed flow pump impeller, Paper No. 60–HYD–7, ASME Cavitation Symposium, March 6–9, 1960, Rice Hotel, Houston, Texas.

[6] H. A. Stahl and A. J. Stepanoff, Thermodynamic aspects of cavitation in centrifugal pumps, Trans. ASME **78,** 1691 (1956).

[7] R. J. Richards, R. B. Jacobs, and W. G. Pestalozzi, Measurement of flow of liquefied gases with sharp-edged orifices, Adv. Cryogenic Eng. **4,** 272–285 (Plenum Press, Inc., New York, N.Y., 1960).

[8] J. R. Purcell, A. F. Schmidt, R. B. Jacobs, The venturi tube as a liquefied gas flow measuring device, Adv. Cryogenic Eng. **5,** 282–288 (Plenum Press, Inc., New York, N.Y., 1960).

[9] K. B. Martin, R. B. Jacobs, R. J. Hardy, Performance of pumps with liquefied gases, Adv. Cryogenic Eng. **2,** 295–302 (Plenum Press, Inc., New York, N.Y., 1960).

[10] V. Salemann, Cavitation and NPSH requirements of various liquids, Trans. ASME, J. Basic Eng., p. 167 (June 1959).

[11] T. Y. Wu, The theory of cavitating flow, Presented at the Cavitation and Turbomachinery Conference, May 20, 1960, California Institute of Technology, Pasadena, Calif.

[12] R. B. Jacobs, K. B. Martin, and R. J. Hardy, Direct measurement of net positive suction head, Trans. ASME, J. Basic Eng., p. 147 (June 1959).

[13] G. H. Caine, L. J. Schafer, D. A. Burgeson, Pumping of liquid hydrogen, Adv. Cryogenic Eng. **4,** 241–254 (Plenum Press, Inc., New York, N.Y., 1960).

[14] M. W. Benjamin and J. G. Miller, The flow of saturated water through throttling orifices, Trans. ASME **63,** 419 (July 1941).

[15] M. R. Hatch, R. B. Jacobs, R. J. Richards, R. N. Boggs, G. R. Phelps, Prediction of pressure drop in two-phase, single-component fluid flow, Adv. Cryogenic Eng. **4,** 357–377 (Plenum Press, Inc., New York, N.Y., 1960).

[16] R. C. Martinelli and D. B. Nelson, Prediction of pressure drop during forced-circulation boiling of water, Trans. ASME **70,** 695 (August 1948).

(Paper 65C3–65)

JOURNAL OF RESEARCH of the National Bureau of Standards—C. Engineering and Instrumentation
Vol. 65C, No. 3, July–September 1961

Heating and Cooling of Air Flowing Through an Underground Tunnel*

B. A. Peavy

(April 25, 1961)

Fresh or outside air needed for ventilating underground installations is introduced through shafts or tunnels. For a shaft or tunnel in continuous use, heat is transferred from the air to the rock in summer and from the rock to the air in the winter, thereby reducing the seasonal cooling and heating loads of the underground installation. The possible benefit of this tempering effect in reducing the size and operating cost of the air cooling and heating system of the installation cannot be realized in the design stage without a reliable means of estimating the influence of the tunnel. In this paper, equations and functions for computing the tempering effect are developed by mathematical analysis of the problem, assuming a sinusoidal variation of the outside air temperature, and are shown to be in substantial accordance with experimental results obtained in tests made in a small-scale model tunnel.

1. Introduction

When outside air for ventilating an underground chamber, or for other purposes, is drawn continuously through a long tunnel or airway in rock, heat interchange between the rock and the flowing air considerably reduces, by the time the air reaches the far end, the fluctuations of temperature to which the entering outside air was subject as a result of diurnal and seasonal changes. The tempering thus effected by the rock in cooling summer air and heating winter air may have an important benefit in reducing the design size and operating cost of the air cooling and heating systems of an underground installation. Mine and tunnel air ventilation studies [1, 2] [1] have shown qualitatively the reduction of the fluctuations of temperature of outside air flowing into mines, but have ventured no analysis of this process for prediction of temperatures and heat flow quantities.

This paper presents the results of a mathematical analysis of the heat transfer between the air and the rock, assuming that the temperature of the entering air varies periodically and sinusoidally. For the case of long tunnels in rock, diurnal and short-time climatic fluctuations are quickly attenuated and damped out in the first part of the tunnel. Consequently, the significant fluctuation is the seasonal or annual periodic variation in outdoor air temperature, which is known to approximate a sinusoidal oscillation [3].

The mathematical solutions obtained are for the case of dry air. Efforts to take account of heat exchanges between the air and rock due to condensation of moisture from the air, or its evaporation from the rock, introduce mathematical complexities that preclude analytic solutions. However, the results obtained for dry air are conservative in regard to the amounts of heat transferred between the air and rock, as the effect of latent heat transfer is to increase the total heat exchanges to values greater than those given by the equations for dry air conditions.

To determine the validity of the analytical treatment for design purposes, experiments were conducted on a small-scale model underground tunnel, and the data thus obtained were compared with the results predicted by the analytical method.

2. Analysis

To obtain a mathematical expression for the heat-transfer characteristics of the rock surrounding an air-intake tunnel, let us assume that the tunnel takes the form of a hollow cylinder. Let us further assume that the temperature T_0 of the air entering the tunnel varies periodically about its mean annual value T_i in accordance with the following relationship:

$$(T_0-T_i)=(T_{0(\max)}-T_i)\cos \omega t$$

where the angle ωt increases by 2π radians (360°) in 1 year.

For convenience in the development, we will use a subrogated temperature θ, defined as $(T-T_s)$, where T_s is the steady temperature of the rock remotely surrounding the tunnel. On this basis, the subrogated annual mean temperature θ_i of the entering air is (T_i-T_s); the amplitude of entering air temperature variation $(T_{0(\max)}-T_i)$ is designated as Δ. Accordingly, the equation above becomes:

$$T_0-T_s=\theta_0=\theta_i+\Delta \cos \omega t. \quad (1)$$

The hollow cylinder has a radius, a, but is otherwise unbounded. The surrounding solid has a conductivity K, specific heat c, and thermal diffusivity α. The air flows in the cylinder at a velocity V in the direction of the positive x-axis. It is assumed that in the surrounding rock, heat is conducted radially but not parallel to the axis of the cylinder, and the thermal properties are independent of temperature.

*This work was supported by the Protective Structures Branch, Office of the Chief of Engineers, U.S. Army.

[1] Figures in brackets indicate the literature references at the end of this paper.

Let M' be the mass of air in contact with unit surface area of the cylinder, c' the specific heat of the air, θ_x the air temperature at a distance x and time t, and h the coefficient of heat transfer between the air and the cylinder surface. The heat balance equation satisfied by the temperature of the air at distance x is then:

$$M'c'\left[\frac{d\theta_x}{dt}+V\frac{d\theta_x}{dx}\right]+h(\theta_x-\theta_{a,x})=0 \qquad (2)$$

where $\theta_{a,x}$ is the temperature at the surface of the cylinder at distance x. The heat transfer at a distance x along the cylinder surface is:

$$-K\left(\frac{d\theta_{a,x}}{dr}\right)=h(\theta_x-\theta_{a,x}). \qquad (3)$$

Equations (1), (2), and (3) provide the boundary conditions for the differential equation for conduction of heat in the solid:

$$\frac{\partial^2\theta_{r,x}}{\partial r^2}+\frac{1}{r}\frac{\partial\theta_{r,x}}{\partial r}-\frac{1}{\alpha}\frac{\partial\theta_{r,x}}{\partial t}=0.$$

A closely approximate solution for the temperature of the air at distance x, assuming steady periodic heat flow, is:

$$T_x-T_z=\theta_x=e^{-AA'}[\Delta\cos(\omega t-AB')+\theta_i\cos AB'] \qquad (4)$$

where A involves x, and A' and B' involve h.

The derivation of eq (4) is given in section 8.1. The symbols are defined in section 8.3. The functions A' and B' are plotted on figure 1 for a useful range of the variables $z(=a\sqrt{\omega/\alpha})$ and $n(=ah/K)$.

3. Model Underground Tunnel

The model underground tunnel (see fig. 2) was cylindrical, 6 in. in diameter and 33.7 ft long, surrounded by 18 in. of 1:4 cement-sand mortar. Several thicknesses of ½-in. hair-felt insulation were placed on the outside of the mortar. Air was drawn through the tunnel by a blower and its rate of flow was measured by means of an orifice in the sheet metal duct connecting the tunnel and the blower. At the entrance to the tunnel was a sheet metal duct containing chilled water coils and electric strip heaters. The chilled water coils were used to cool the air to a temperature below the lowest temperature to be encountered at the entrance to the tunnel. The electric strip heaters were governed by a program controller that modulated the heat input to the air so that the entering air temperature varied sinusoidally as a function of time. Thermocouples were located at the entrance and exit and at various locations in the tunnel, and in the surrounding cement mortar, as shown in figure 2. The thermal properties of the cement-sand mortar were determined from samples obtained during pouring operations.

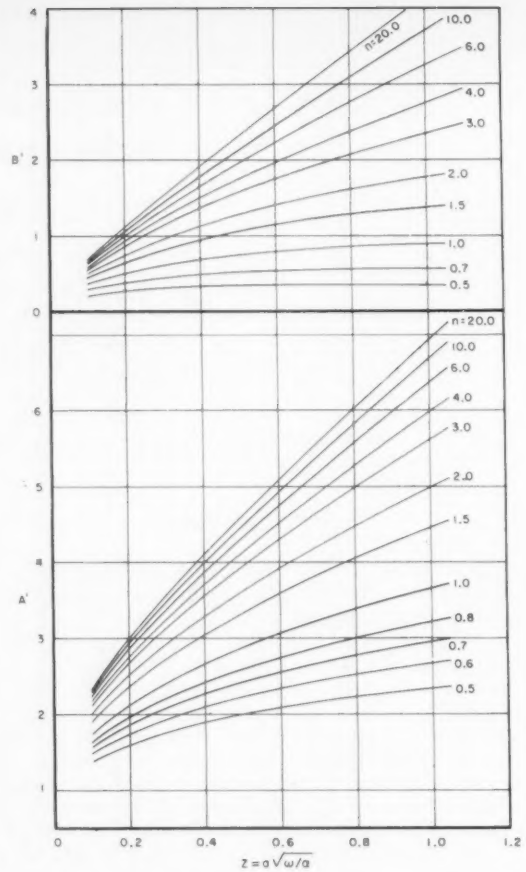

FIGURE 1. *Values of* A′ *and* B′ *as functions of* z(=a√ω/α) *and* n(=ah/K) *for use in eq (4).*

Each test consisted of four cycles of temperature variation with a period of 16 hr and an amplitude of about 20 °F. Because the transients due to the initial nonperiodic condition were virtually eliminated in the first two cycles, the last two cycles were used for test results.

4. Results

Three tests, in which weight rate of air flow, W', was varied, were carried out on the model underground tunnel. The parameters for these tests are given in table 1.

TABLE 1. *Test parameters*

Angular velocity, ω	0.3927 radian/hr
Tunnel radius, a	.25 ft
Tunnel length, L	33.7 ft
Thermal conductivity (mortar), K	0.747 Btu/hr-ft-°F
Thermal diffusivity (mortar), α	.031 ft²/hr
Specific heat (air), c'	.24 Btu/lb-°F
$z=a\sqrt{\omega/\alpha}$	.89

Pertinent test data are given in table 2. The observed entering air temperatures were substan-

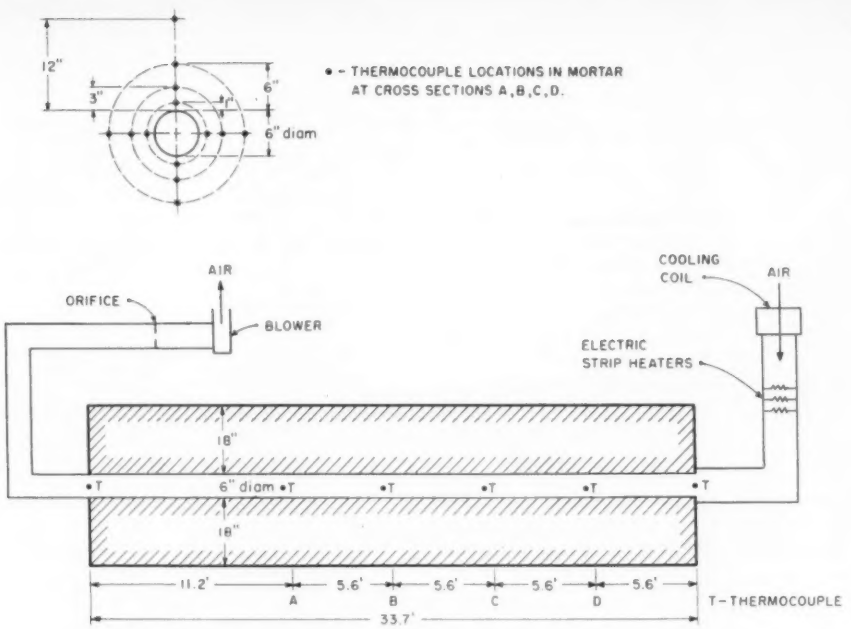

FIGURE 2. *Diagrammatic sketch of model underground tunnel.*

tially sinusoidal and conformed very closely to the equations (within ± 0.25 °F), of the form of eq (1), set forth in table 3. The observed values of air temperature at the exit of the tunnel ($L=33.7$ ft) were found to lag in phase those of the entering air by about 0.14 radian. All experimental quantities involved in eq (4) were determined directly, except the coefficient of heat transfer, h. Since θ_x is a maximum when $(\omega t - AB')$ equals zero, eq (4) serves for computing A', from which the values of h were obtained. The values of h thus computed are presented in table 2 and are compared with values of the forced convection heat transfer coefficient calculated from an equation given by McAdams [4] which, with appropriate properties for the model tunnel and air substituted, is

$$h=0.016(W')^{0.8}. \tag{5}$$

TABLE 2. *Data and results from tests on model underground tunnel*

Test No.	1	2	3
Entering air temps., T_0, °F:			
Maximum	109.4	101.4	100.8
Minimum	65.2	60.0	60.0
Mean, T_0	87.3	80.7	80.4
Amplitude, Δ	22.1	20.7	20.4
Leaving air temps., T_L, °F:			
Maximum	95.0	90.2	91.5
Minimum	75.0	71.0	71.2
Mean	85.0	80.6	81.35
Mean remote temp. of solid (mortar), T_s, °F	83.2	80.3	82.2
$\theta_i = T_i - T_s$, °F	4.2	0.4	−1.8
Air flow rate, W', lb/hr	336.4	367.9	451.2
Coefficient of heat transfer h, Btu/hr-ft²-°F:			
From eq (4)	1.76	1.85	2.22
From eq (5)	1.69	1.82	2.14

TABLE 3. *Applied entering and predicted leaving air temperatures*

	Entering air (eq. 1)	Leaving air, $L=33.7$ (eq. 4)
Test 1	$T_0=87.4+22.2\cos\omega t$	$T_L=85.1+10.0\cos(\omega t-0.1417)$
Test 2	$T_0=80.7+20.7\cos\omega t$	$T_L=80.5+9.7\cos(\omega t-0.1425)$
Test 3	$T_0=80.4+20.4\cos\omega t$	$T_L=81.3+10.2\cos(\omega t-0.1457)$

Substituting the derived values of h, and observed values of Δ, θ_i, and the parameters from table 1 in eq (4), for $L=33.7$ ft, we obtain the time variation of the leaving air temperature as given by the equations in table 3. When these equations were plotted, the curves followed the experimental data within ± 0.25 °F.

The tempering effect of the tunnel on the air is shown by referring to test No. 3, table 3, where the amplitude of the air which was 20.4 °F at the entrance, was reduced to 10.2 °F at the exit.

Although the experimental data on air temperature satisfied the analytical solution of the problem, it was felt that further substantiating information was desirable. Equations for the time-variation of temperatures at various radii in the surrounding cement-sand mortar were therefore computed from eq (12) for test No. 3, as shown in table 4. Plots of these equations with associated experimental data appear in figure 3.

TABLE 4. *Temperatures in the cement-sand mortar for test No. 3 at cross-section* $x=22.7$ *ft, as predicted by eq (12) of section 8.1*

At radius $r=0.33$ ft	$T_{x,r}=82.0+3.1\cos(\omega t-0.733)$
At radius $r=0.50$ ft	$T_{x,r}=82.1+1.7\cos(\omega t-1.169)$
At radius $r=0.75$ ft	$T_{x,r}=82.2+0.7\cos(\omega t-1.815)$
At radius $r=1.25$ ft	$T_{x,r}=82.2\pm 0.1$

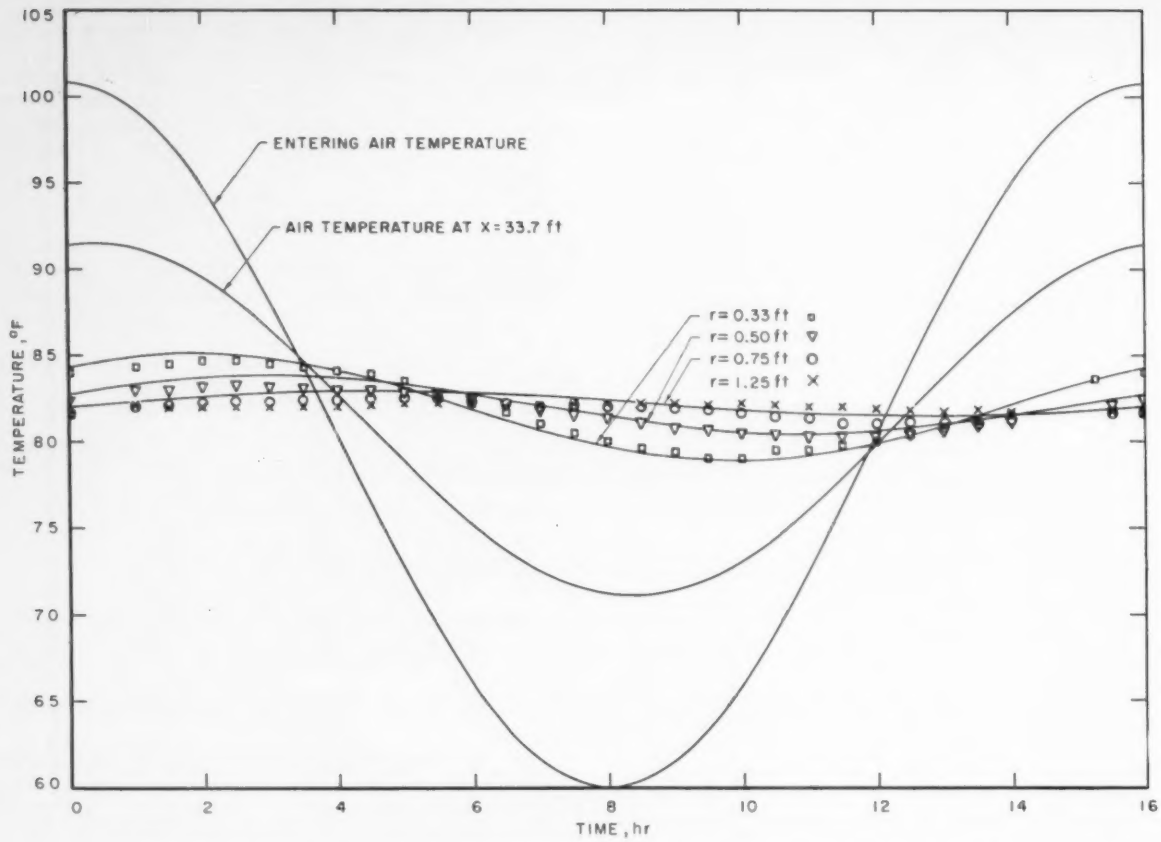

FIGURE 3. *Air and mortar temperature history for model underground tunnel (test No. 3, table 2).*
Experimental data for temperatures in mortar at various radii from center of tunnel are denoted by symbols.

5. Discussion

For the model tunnel, values of the coefficient of heat transfer were computed from eq (4) and the temperature amplitudes of the leaving air by the method outlined in section 4. A comparison of these coefficients with those determined from eq (5) shows agreement within 5 percent, which is within the probable accuracy of the thermal properties of cement-sand mortar as determined by tests on a few samples.

For tunnels or shafts probable in underground installations, the diameters are likely to be greater than 3 ft. Values of the coefficient of heat transfer are not found in the literature for airways of this size and would be particularly difficult to predetermine for the rough and irregular surfaces usually resulting from the excavating process. However, reasonable values may be estimated from compromise considerations of values determined for air flow in small cylinders and air flow parallel to planes, and with an allowance for roughness of surfaces.

Substitution of the parameters and the derived values of h into eq (4) gave the equations for the leaving air temperatures given in table 3. These equations showed differences less than 0.3 °F when plotted with the experimental data. Differences less than 0.5 °F were found between observed temperatures in the surrounding solid (mortar), and those computed by eq (12), as shown in figure 3.

Because the experimental data agree closely with values computed by eqs (4) and (12), the analytic approach developed in this paper should be applicable for determining temperatures in tunnels of larger size.

6. Application to a Practical Problem

To design heating and air conditioning equipment for an underground installation, it is necessary to predict the maximum and minimum temperatures of the air when it is delivered at the installation. From eq (4), the maximum and minimum temperatures occur when $\omega t = AB'$ and $\omega t = \pi + AB'$, respectively. Using eq (4), these extreme values may be written

$$(\theta_L)_m = e^{-AA'}(\pm\Delta + \theta_i \cos AB'). \qquad (6)$$

Figure 1 is a plot of A' and B' as functions of n and z computed for a range of values expected in a practical problem.

For a sample hypothetical problem, consider a square tunnel with nominal dimensions 7 ft by 7 ft by 2000 ft long, continuously delivering air to an underground installation at a rate of 50,000 cubic feet per minute, or 228,000 pounds per hour. For noncircular cross sections, the equivalent cylindrical radius, a, is equal to 2 (cross sectional area)/(perimeter). Assumed parameters for substitution in eq (6) are given in table 5.

TABLE 5. *Parameters for hypothetical problem*

Thermal conductivity of surrounding rock	K=1.2 Btu/hr-ft-°F
Thermal diffusivity of surrounding rock	α=0.035 ft²/hr
Angular velocity (period one year)	ω=0.000717 radian/hr
Coefficient of heat transfer	h=3.43 Btu/hr-ft²-°F
Equivalent radius of tunnel	a=3.5 ft
Amplitude of outside air	Δ=45 °F
Mean temperature of outside air	Ti=52 °F
Remote rock temperature	T_s=55 °F
Specific heat of air	c'=0.24 Btu/lb-°F
Weight rate of air flow	W′=228,000 lb/hr
θ_i	$T_i-T_s=-3$ °F
n	$ah/K=10$
z	$a\sqrt{\omega/\alpha}=0.5$
A' (function of n and z) figure 1	=4.48
B' (function of n and z) figure 1	=2.15
A	$KL/c'W'=0.0439$

The extreme values predicted by eq (6) are

$$(\theta_L)_m=+34 \text{ and } -39 \text{ °F}.$$

Because θ is a subrogated temperature based on a zero value equal to the remote temperature of the surrounding rock, the maximum and minimum air temperatures at the end of the tunnel (L=2000 ft) are 55+34=89 °F and 55−39=16 °F, respectively. The maximum and minimum outside air temperatures (eq (1)) are 97 °F and 7 °F, respectively. The maximum and minimum air temperatures at the end of the tunnel lag those at the entrance by an angle equal to AB', which in this case equals 0.094 radian, equivalent to a time-lag of 5.5 days.

Although the rates of heat loss and gain of the air in a tunnel were not discussed in the experimental portion of this paper, they are of considerable interest in the application to practical problems. For the hypothetical problem, the average rate of cooling by the rock during the cooling season (eq (14), section 8) is 251,000 Btu/hr, or an equivalent of about 21 tons of refrigeration. The average rate of heating by the rock in the heating season is 309,000 Btu/hr, equivalent to the heating effected by burning about 3.35 gallons of fuel oil per hour. The maximum cooling and heating rates are substantially greater than the average, as indicated by eq (13).

7. Conclusions

Mathematical equations are derived for computing the tempering effect of a long tunnel in reducing the amplitude of climatic temperature variation of outside air flowing through a tunnel. Results of experiments support the application of the developed equations for design purposes.

The functions necessary for design use of the equations have been evaluated for a useful range of the parameters and are presented graphically.

In the design for heating and air conditioning systems, fresh or outside air necessary for ventilation of an underground installation represents a portion of the heating and cooling load for the installation. Without a means for determining the temperature of the air at the end of its passage through tunnels or shafts, the designer is forced to rely upon the outside air temperatures for design conditions. The hypothetical problem of section 6 shows that the heating and cooling loads for design purposes are considerably reduced when the temperature of air at the end of a tunnel is predicted by the derived equations. These equations are included in a design manual for military installations [5].

An assumption has been made which develops a degree of uncertainty toward the use of the equations. An effective coefficient of heat transfer value "h" suitable for a particular application may, in most cases, only be determined as an educated guess, because no predictable values for large size tunnel airways are available from literature.

8. Appendix

8.1. Solution of Heat Transfer Problem

With the boundary conditions as set forth in eqs (1), (2), and (3) of section 2, eq (4) may be obtained by assuming that the temperature in the surrounding solid at a cross section at a distance x from the entrance is

$$\theta_{r,x}=Fe^{i\omega t}, \text{ where } F=f(r) \tag{7}$$

and also that the temperature of the flowing air is:

$$\theta_x=Ge^{i\omega t}, \text{ where } G=f(x). \tag{8}$$

By substituting the appropriate derivatives of eq (7) in the differential equation for conduction of heat radially in a cylindrical system having angular symmetry:

$$\frac{\partial^2\theta}{\partial r^2}+\frac{1}{r}\frac{\partial\theta}{\partial r}-\frac{1}{\alpha}\frac{\partial\theta}{\partial t}=0$$

the latter becomes

$$F''+\frac{1}{r}F'-\frac{i\omega F}{\alpha}=0.$$

This is the modified Bessel equation of zero order, for which the general solution given in terms of the modified Bessel functions I_0, K_0, is

$$F=DI_0\left(r\sqrt{\frac{i\omega}{\alpha}}\right)+CK_0\left(r\sqrt{\frac{i\omega}{\alpha}}\right).$$

For F to be finite as r approaches infinity, D=0, and a particular solution is:

$$F=CK_0\left(r\sqrt{\frac{i\omega}{\alpha}}\right)$$

and from eq (7),

$$\theta_{r,z}=Ce^{i\omega t}K_0\left(r\sqrt{\frac{i\omega}{\alpha}}\right). \tag{9}$$

Differentiating,

$$\left(\frac{d\theta}{dr}\right)_{r=a}=-Ce^{i\omega t}\sqrt{\frac{i\omega}{\alpha}}K_1\left(a\sqrt{\frac{i\omega}{\alpha}}\right). \tag{10}$$

Substituting eqs (9) and (10) in eq (3), and solving for C, eq (10) becomes:

$$\left(\frac{d\theta}{dr}\right)_{r=a}=\frac{-\theta_x\frac{h}{K}\sqrt{\frac{i\omega}{\alpha}}K_1\left(a\sqrt{\frac{i\omega}{\alpha}}\right)}{\sqrt{\frac{i\omega}{\alpha}}K_1\left(a\sqrt{\frac{i\omega}{\alpha}}\right)+\frac{h}{K}K_0\left(a\sqrt{\frac{i\omega}{\alpha}}\right)}. \tag{10a}$$

Simplify by letting

$$z=a\sqrt{\omega/\alpha}$$

$$K_0(z\sqrt{i})=N_0(z)e^{i\phi_0(z)}$$

$$\sqrt{i}\,K_1(z\sqrt{i})=N_1(z)e^{i\left\{\phi_1(z)+\frac{3\pi}{4}\right\}}$$

$$n=ah/K$$

$$P=z\frac{N_1(z)}{N_0(z)}$$

$$\mu=\phi_1(z)+\frac{\pi}{4}-\phi_0(z).$$

Where values of the functions of $N_0(z)$, $N_1(z)$, $\phi_0(z)$, and $\phi_1(z)$ are given by McLachlen and Meyers [6], eq (10a) becomes

$$-\left(\frac{d\theta}{dr}\right)_{r=a}=\frac{(\theta_x)}{a}\frac{nPe^{i(\mu+\pi/2)}}{n+Pe^{i(\mu+\pi/2)}}.$$

Rationalizing and further simplifying, eq (3) becomes

$$-K\left(\frac{d\theta}{dr}\right)_{r=a}=\frac{K\theta_x}{a}\frac{P-n\sin\mu+in\cos\mu}{\frac{n}{P}+\frac{P}{n}-2\sin\mu}$$

$$=\frac{K\theta_x}{2\pi a}(A'+iB')=h(\theta_x-\theta_{a,x})$$

where

$$A'=\frac{2\pi(P-n\sin\mu)}{\frac{P}{n}+\frac{n}{P}-2\sin\mu},\ \text{(fig. 1)}$$

$$B'=\frac{2\pi n\cos\mu}{\frac{P}{n}+\frac{n}{P}-2\sin\mu},\ \text{(fig. 1)}.$$

Substituting the above in eq (2)

$$V\frac{d\theta_x}{dx}+\frac{d\theta_x}{dt}+\frac{K\theta_x}{2\pi M'c'a}(A'+iB')=0.$$

Substituting from eq (8),

$$VG'+i\omega G+\frac{GK}{2\pi M'c'a}(A'+iB')=0.$$

Letting $A=\frac{Kx}{2\pi aVM'c'}=\frac{Kx}{W'c'}$

the solution of the differential equation is:

$$G=Je\left[-\frac{i\omega x}{V}-A(A'+iB')\right].$$

Substituting in eq (9),

$$\theta_x=Je\left[i\omega t-\frac{i\omega t}{V}-A(A'+iB')\right].$$

Equation (1) states:

$$\theta_0=\theta_i+\Delta e^{i\omega t}$$

then

$$J=\Delta+\theta_i e^{i\omega t}.$$

Making this substitution,

$$\theta_x=e^{-AA'}\left[\Delta e^{i\left(\omega t-\frac{\omega x}{V}-AB'\right)}+\theta_i e^{-i\left(\frac{\omega x}{V}+AB'\right)}\right].$$

Considering only the real part,

$$\theta_x=e^{-AA'}\left[\Delta\cos\left(\omega t-\frac{\omega x}{V}-AB'\right)+\theta_i\cos\left(\frac{\omega x}{V}+AB'\right)\right].$$

For frequencies ω under consideration, the term $\omega x/V$ is negligible and a closely approximate solution is

$$\theta_x=e^{-AA'}[\Delta\cos(\omega t-AB')+\theta_i\cos AB']. \tag{4}$$

Without giving the derivation from eq (9), the temperature at radius, r, in the solid surrounding the tunnel is:

$$\theta=\Delta e^{-AA'}\frac{N_0(R)}{N_0(z)}\frac{\cos(\omega t+S-\tau)+\frac{\theta_i}{\Delta}\cos(S-\tau)}{\sqrt{\left(\frac{P}{n}\right)^2+1-2\frac{P}{n}\sin\mu}} \tag{12}$$

where

$$R=r\sqrt{\omega/\alpha}=rz/a$$

$$S=\phi_0(R)-\phi_0(z)-AB'$$

$$\tau=\tan^{-1}\frac{\cos\mu}{\frac{n}{P}-\sin\mu}.$$

8.2. Air Heat Exchange

At any time, t, the rate at which heat is lost by the flowing air is:

$$q=W'c'(\theta_0-\theta_x).$$

The maximum rates of cooling and heating of the air are given by

$$q_m=W'c'[\pm\Delta\sqrt{1+e^{-2AA'}-2e^{-AA'}\cos AB'} + \theta_i(1-e^{-AA'}\cos AB')].$$

If it is assumed that $\cos AB'\cong 1.0$, then

$$q_m=W'c'(1-e^{-AA'})(\pm\Delta+\theta_i). \qquad (13)$$

The average rate of heat flow for a given cooling or heating cycle is:

$$q_{av}=W'c'(1-e^{-AA'})\left(\pm\frac{2\Delta}{\pi}+\theta_i\right). \qquad (14)$$

8.3. Symbols

Unless otherwise labeled, quantities are dimensionless when consistent units are used:

$A=Kx/W'c'$,

$A'=\dfrac{2\pi(P-n\sin\mu)}{\dfrac{n}{P}+\dfrac{P}{n}-2\sin\mu}$, plotted on figure 1 as a function of n and z,

a=radius of hollow cylinder, ft,
=2(cross section)/(perimeter), for noncircular cylinders,

$B'=\dfrac{2\pi n\cos\mu}{\dfrac{n}{P}+\dfrac{P}{n}-2\sin\mu}$, plotted on figure 1 as a function of n and z,

c=specific heat of surrounding solid, Btu/lb-°F,
c'=specific heat of air flowing in cylinder, Btu/lb-°F,
e=base of Naperian (natural) logarithms,
h=coefficient of heat transfer between air and surface of cylinder, Btu/hr-ft²-°F,
K=thermal conductivity of surrounding solid, Btu/hr-ft-°F,
M'=weight of fluid (air) per unit of surface area of cylinder, lb/ft²,
$n=ah/K$,
$P=zN_1(z)/N_0(z)$,
q=heat flow rate from air to tunnel wall, Btu/hr,
r=radius, ft,
T=temperature, °F. T_0 is temperature of air entering tunnel; T_i is annual mean value of T_0. T_s is the steady temperature of the deep underground rock remotely surrounding the tunnel,
t=time, hr,
V=velocity in tunnel, ft/hr,
W'=weight rate of air flow, lb/hr,
x=distance from entrance of tunnel, ft,
$z=a\sqrt{\omega/\alpha}$,
α=thermal diffusivity of surrounding solid, ft²/hr,
Δ=amplitude of annual variation of T_0 about the mean value T_i, °F,
$=(T_{0(\max)}-T_i)=1/2(T_{0(\max)}-T_{0(\min)})$,
$\mu=\phi_1(z)+\pi/4-\phi_0(z)$,
θ=subrogated temperature, equal to $(T-T_s)$, °F,
θ_i=subrogated annual mean entering air temperature, equal to (T_i-T_s), °F,
ω=angular velocity, radian/hr.

Temperatures at various positions are indicated by the subscripts:

0=at tunnel inlet ($x=0$, $r<a$),
x=at distance x from tunnel inlet ($r<a$),
L=at tunnel outlet ($x=L$, $r<a$),
r,x=at radius r at distance x from tunnel inlet ($r\geq a$),
a,x=at tunnel surface ($r=a$) at distance x from inlet.

The subscript m denotes a maximum or minimum value.

9. References

[1] G. E. McElroy, Ventilation of the large copper mines of Arizona, U.S. Bur. Mines Bull. **330,** 138 (1931).
[2] G. E. McElroy, Engineering factors in the ventilation of metal mines, U.S. Bur. Mines Bull. **385,** 90 (1935).
[3] J. M. Craddock, The representation of the annual temperature variation over central and northern Europe by a two-term harmonic form, Quart. J. Roy. Met. Soc. **82,** 275 (1956).
[4] W. H. McAdams, Heat transmission, Section Edition, 170, Equation (4f) (McGraw-Hill Book Co., Inc., New York, N.Y.).
[5] Heating and air conditioning of underground installations, EM 1110-345-450, Office of the Chief of Engineers, U.S. Army, 49 (Nov. 30, 1959).
[6] N. W. McLachlen and A. L. Meyers, The polar form of the ker and kei functions with applications to eddy current heating, Phil. Mag. **120,** 610 (1934).

(Paper 65C3–66)

JOURNAL OF RESEARCH of the National Bureau of Standards—C. Engineering and Instrumentation
Vol. 65C, No. 3, July–September 1961

Stress-Corrosion Cracking of the AZ31B Magnesium Alloy

Hugh L. Logan

(April 28, 1961)

Both the incubation period prior to stress-corrosion cracking and its initiation in the AZ31B magnesium alloy were studied using electrochemical solution potential-time and extension-time oscillographic curves obtained simultaneously. From these data it is postulated that the crystals most favorably oriented for slip were deformed, on initial stressing of the specimen, to such an extent that they were resistant to further extension and the protective films on their surfaces, destroyed in the early deformation, were repaired. Subsequent extension occurred as the result of stresses concentrated in relatively more resistant crystals with strain rates as high as 1 percent/sec at limited sites rupturing the protective surface film. This exposed metal was anodic to very much larger areas on which the film had been repaired and cracks developed by electrochemical processes.

Stress-corrosion cracks were initiated on planes that made large angles with the basal crystallographic plane of the magnesium alloy and in crystals of a polycrystalline aggregate that were unfavorably oriented for basal slip.

1. Introduction

The stress-corrosion cracking of magnesium-base alloys has been the subject of several studies at NBS. A study of the relative susceptibility of the various wrought magnesium alloys then available was made during World War II and the results were subsequently published [*1*].[1] A service failure that led to the initiation of that study proved to be an isolated case. Stress-corrosion cracking of magnesium alloys in service has not been a problem. However, magnesium alloys lend themselves particularly well to general studies of stress-corrosion cracking in that complete failures, for example, of the FS–1 alloy, can be obtained in the laboratory in less than 5 min. Studies since the war years have been made with the objective of increasing our understanding of the mechanism of stress-corrosion cracking.

A paper published in 1958 [*2*] gave the results of an investigation initiated to answer certain questions that had been raised but never answered during the war work. In that investigation [*2*] it was shown that if the specimen was strained in the corrodent at a rate in excess of 500×10^{-6}/min, measured 1 min after the stress [2] was applied, failure could be expected in less than 5 min. On the other hand if the strain rate was less than 500×10^{-6}/min the specimen would most probably not fail even in 1000 min. Further, it was found on examining many specimens that there was no evidence of cracking for the first 40 sec after the stress was applied even though failures occurred in 2½ min. A short hypothesis was presented to explain this incubation period. In the present paper, experiments designed to verify some of the ramifications of that hypothesis are described and the hypothesis is expanded. The crystallographic planes on which stress-corrosion cracks originated were also determined.

2. Experimental Procedure

Specimens for this investigation were prepared from sheet and extruded AZ31B magnesium alloy stock. The chemical compositions of these materials were well within the tolerances of ASTM Specification B–90–58 for this alloy.[3]

Sheet tensile specimens, having a ½-in. reduced section, were machined from 1/16 and ⅛-in. thick sheet material originally obtained for the earlier work [*1*]. Most of the specimens used in the present investigation were in the annealed condition although a few were from "hard-rolled" sheet.

A very few notched specimens were machined from ½-in. diam extruded rod. The specimens contained a 90° notch ⅛ in. deep. The diameter at the root of the notch was 0.250 in. and the root radius 0.005 in.

Specimens used in determining the crystallographic planes on which the stress-corrosion cracks originated were also machined from the extruded rod. The reduced sections of these specimens were about 2 in. long with a square cross section ¼ in. on a side. They were similar in design to the low carbon steel specimens used by the author in another investigation [*3*]. After machining, the specimens were annealed for 30 min at 400 °C, cooled to room temperature, strained 0.3 to 0.5 percent, and subsequently heated slowly to 520 °C. The resulting specimen was multigrained, with individual grains

[1] Italicized figures in brackets indicate the literature references at the end of this paper.

[2] A stress in excess of 95.5 percent of the yield strength of the annealed material was required to produce stress-corrosion cracking of this alloy in the corrodent used.

[3] The nominal composition of the AZ31B alloy is Al 3.0 percent, Zn 1.0 percent, Mn 0.20 min, with maximum values for Si, Cu, Fe, Ni, and Ca of 0.10 percent, 0.05 percent, 0.005 percent, 0.005 percent, and 0.04 percent respectively.

sufficiently large that their crystal orientations could be determined by the conventional back reflection X-ray technique.

The sheet specimens were insulated from the corrodent, except for a 2 in. gage length, by means of plastic tape. All of the notched specimens were also insulated with tape except over the notched areas. One set of the notched specimens was exposed to the corrodent with the entire notched area exposed. In the other set the notch was covered with lacquer and after the lacquer had dried it was cut through with a razor blade to expose the metal at the root of the notch.

All specimens were contained in glass cells of the type described earlier [*1*]. The corrodent was the conventional NaCl, K_2CrO_4 solution (35 g NaCl and 20 g K_2CrO_4/liter) at approximately 30 °C. The specimens were stressed in tension by dead loading with a lever system. In all cases care was exercised to avoid impact in applying the stress. If the specimen strain was to be followed, the lever was supported by a hydraulic jack until the load, etc., were adjusted. The jack was then released, applying the stress at a rapid rate.

The strain or extension of the specimen was followed by measuring the movement of the end of the loading lever (lever ratio 25 to 1). This was done by reading a dial gage (smallest division 1/10,000 in.) or by recording the unbalance of a bridge circuit, one arm of which contained wire strain gages actuated by the motion of the end of the lever. In a few instances wire strain gages cemented onto the specimen itself (but insulated from the solution) were incorporated in the bridge circuit.

The electrochemical solution potentials of the sheet and notched specimens were determined against a calomel electrode of the saturated KCl type. Connection between the electrode and the corrodent was made by means of a salt bridge. The electrochemical solution potential and the extension of the specimen (as determined by the unbalance of the bridge circuit) were recorded simultaneously on a two-channel oscillograph.

No extensions nor electrochemical solution potentials were determined for the large-grained specimens on which the crystallographic orientation of the plane of fracture was determined. The stress was removed from some of these specimens after cracks had developed but before the final fracture had occurred. If fracture was complete, no attempt was made to determine the plane on which this fracture occurred, but analyses were made to determine the planes of origin of other cracks that formed but had not led to complete failure.

Visual observations showed that cracks generally originated at a corner of the specimen where adjacent surfaces met. Hence, the crystallographic planes on which the cracks originated were determined from the angles that the cracks made on the adjacent faces with the corners of the specimen [*4*].

The orientation of the tension axis of the specimen with respect to the crystallographic axes was determined for the grains containing cracks and also for a number of grains free from cracks.

3. Results and Discussion

3.1. Extension Time and Electrochemical Solution Potential Curves

The idealized curves shown in figure 1 were based on a study of simultaneous oscillographic records of the strain and accompanying changes in electrochemical solution potentials for a number of specimens. The extension increased very rapidly upon initial loading of the specimen. It continued to increase but at a diminishing rate for 40 to 50 sec. The rate then increased again, with the development of stress-corrosion cracks, to final failure of the specimen after about 150 sec exposure. The electrochemical solution potential changed about 90 mv in the anodic direction on the initial loading of the specimen. This was attributed to the rupturing of the protective film on the surface. The further marked change of potential in the anodic direction with the exposure of bare metal, on the failure of the specimen, substantiated this idea. The total change in potential from the unstressed condition amounted to approximately 200 mv, a value that is in good agreement with previously published data [*5*]. It should be noted that once failure had occurred and the metal was no longer being strained the potential changed very abruptly, probably within 1 sec, to a value only about 20 mv more active than that of the specimen in the original condition. The extremely rapid rate of change in potential after the fracture of the specimen indicated that a protective film was being formed on the surface of what had been bare metal.

The yield strength of the annealed alloy can be increased about 50 percent by cold work. From the extension curve, figure 1, it is to be expected that the alloy is being cold worked. It is postulated that

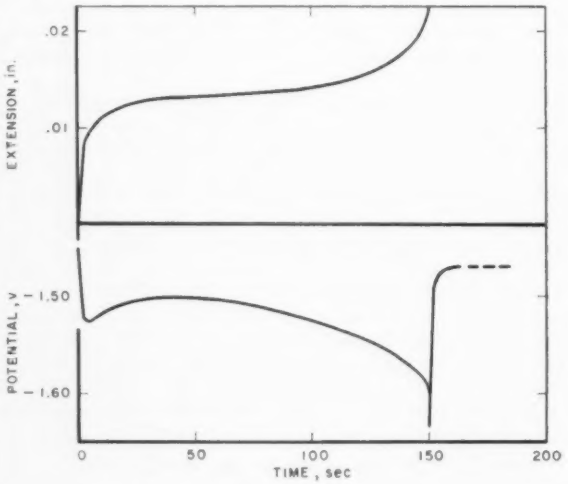

FIGURE 1. *Idealized extension-time and potential-time curves for the AZ31 alloy specimen that failed in about 150 sec.*

with the application of stress, those grains most favorably oriented with respect to the stress pattern were deformed by basal slip, kinking, etc., and were hardened to the point where further deformation occurred only very slowly. Specifically, dislocations moved through the material until they were blocked at barriers such as grain boundaries, subgrain boundaries, inclusions, etc. Stress concentrations were built up as a result of this dislocation pileup and slip then occurred in some of these grains that had previously resisted deformation. This process would be repeated as stresses concentrated in successively more resistant grains and produced deformation. The delayed strain in these relatively resistant grains thus accounted for the slow increase in extension after the initial deformation. While the deformation of individual grains was postulated to be a discontinuous process, the average effect over many grains was recorded as a continuous process.

The increase in the potential (in the active direction) on the initial loading of the specimen is postulated, as was indicated above, to be due to the rupturing of the protective film on those grains that were most readily plastically deformed.

The data obtained at the final fracture of the specimen would indicate that as a given grain was work hardened to the point where it became resistant to further strain, i.e., where the strain rate was low, the protective film was repaired on its surface. As the ratio of grains being strained at a rate sufficient to rupture the film decreases with respect to those on which the film had been repaired, the potential would change in the noble direction. This would account for the change in potential, after the initial extension of the specimen. If the average extension rate of the specimen, determined 40 or 60 sec after the stress was applied, was below some critical value, the potential would continue to change in the noble direction until it approached the value obtained prior to stressing the specimen.

If the average strain rate exceeds this critical value, stress concentrations at a few sites will deform the specimen surface at a sufficient rate to prevent the film from reforming. If these sites are localized for a sufficient time, cracks will be initiated by an electrochemical process. As was indicated earlier, the bare metal is at least 200 mv anodic to the film-covered surface in the corrodent used. If a relatively large area is film-free, attack will be of the pitting type. If the film-free area is very small and is surrounded by a large film-covered area, the condition of a small anode and large cathode will exist; this is an ideal condition for rapid corrosion of the anode. Such corrosion on a small area will form a sharp pit or trench that will further concentrate the stresses, preventing the film from reforming at its apex, and will lead to the initiation of stress-corrosion cracks.

Once cracking is initiated, the continuous exposure of bare metal at the tips of the cracks will change the potential of the specimen in the anodic direction. A very marked change occurred, as was pointed out earlier, with the exposure of a considerable surface of bare metal at the failure of the specimen.

3.2. Strain-Rate Associated With Initiation of Cracks

The extension of many specimens was followed by readings, at stated intervals, of the dial gage in contact with the end of the lever system. This method was highly sensitive and although it was not possible to measure the extension of the specimen during the first 10 to 20 sec of exposure, data was obtained subsequently from which extension rate—time curves could be drawn. Three such curves are shown in figure 2. Breaks in curves A and B resulted from the development of stress-corrosion cracks in those specimens. No cracks developed in specimen C which extended at a slower rate than either A or B. Cracks began to develop in specimens extending at the approximate rate shown for B after about 40 sec exposure in the corrodent [*2*]. If the strain at sites where cracks will develop is postulated to account for the difference in the strain rates of specimens B and C after 40 sec, if certain assumptions are made as to the width of the regions in which cracks will develop, and if the number of cracks that develop per inch of specimen length is determined, an estimate can be made of the strain rate at these crack sites. It was found that approximately 25 crack sites develop for each inch of gage length. Assume that the strain is confined to a region 1000 times the "*a*" parameter of the magnesium lattice; then the average strain rate in the areas where cracks were being initiated can be calculated to have been approximately 1×10^{-2}/sec (1%/sec). This value seems reasonable within one order of magnitude. It is comparable with the value of 5 percent/sec reported by Hoar and West [*6*] as the strain rate necessary to prevent polarization that would have stifled development of cracks in austenitic stainless steel specimens.

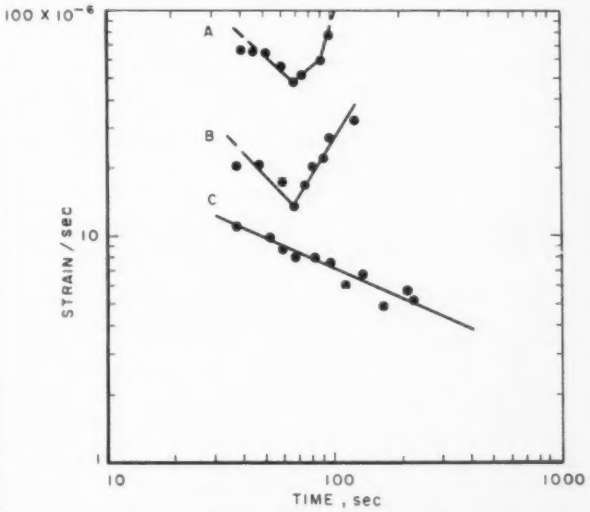

FIGURE 2. *Relations between time and strain rate for specimens stressed above and below the critical strain rate at which stress-corrosion cracks develop.*

Breaks in curves A and B indicate the development of stress-corrosion cracks No cracks developed in the specimen from which curve C was obtained.

3.3. Effect of Ratio of Cathode to Anode Areas on Incubation Period

Several notched specimens were exposed to the corrodent at a stress of approximately 46,000 lb/in.^{2}; this stress [4] could produce failures by stress-corrosion cracking in 60 sec or less. As was indicated above, all of the metal in the notched areas of some of these specimens was exposed to the corrodent while only the metal at the root of the notch was exposed in other specimens.

All specimens failed at the stress level used. However, the incubation period (exposure period before there were indications that cracks were initiated) was about six times as long for specimens that were completely insulated except at the root of the notch, as for those specimens where the whole notched area was exposed to the corrodent.

The stresses concentrated at the roots of the notches of these latter specimens limited all strains of any appreciable magnitude to those regions. The protective film will be ruptured only at the root of the notch. The sides of the notch (when exposed to the corrodent) will be film-covered, cathodic to the root of the notch, and very much larger than the anodic (film-free) area at the root of the notch. Thus there exists the condition of a very small anode and large cathode that is ideal for rapid corrosion by electrochemical processes.

In specimens on which only the roots of the notches are exposed to the corrodent there will be some small areas where the strain rate is higher than others, that is, on which the protective film will be ruptured. Conversely, there will be some areas where there will be more opportunity for the film to repair than on others. The resulting anodic and cathodic areas may be nearly the same size and while electrochemical corrosion may occur and cracking eventually develop, the rate will be much slower than if a large cathode-small anode relationship exists.

The evidence [*7*, *8*] indicated that once cracks have penetrated into the metal, the sides of the cracks become the cathodic areas; whether or not the sides of the notches are insulated is then of little further importance.

3.4. Crystallographic Data on Crystals Containing, and Free From, Stress-Corrosion Cracks

The poles of the planes on which stress-corrosion cracks were initiated are shown in a single stereographic triangle in figure 3. In every case these planes make large angles with the basal plane. If the same condition exists in this alloy as has been reported for relatively pure magnesium [*9*], namely, that the basal planes of the crystals in an extrusion are approximately parallel to the direction of extrusion, then the fact that the poles of the stress-corrosion cracks make high angles with the pole of the basal plane is to be expected.

[4] Stresses of this magnitude will produce a true strain of approximately 0.03; this included a deviation from the modulus line of about 0.015.

With the exception of C–2, C–8, and possibly C–11, the planes of fracture do not lie close to any low-index crystallographic planes. These results agree in a general way with those obtained by Meller and Metzger [*10*] on single crystals of an AZ61 alloy and do not agree with those reported by Priest [*7*] for the same alloy.

It is well recognized that the planes of stress-corrosion cracks are generally approximately normal to the stress axis. The data obtained in this investigation further confirm that observation. The resolved tensile stress normal to the plane of the stress-corrosion crack is proportional to the cosine of the angle between the tension axis and the normal to the plane of the stress-corrosion crack. These angles for the various stress-corrosion cracks are given in column 2 of table 1. The corresponding cosines are listed in column 3. The component of the stress normal to the stress-corrosion crack is in no case smaller than 0.934 times the tensile stress.

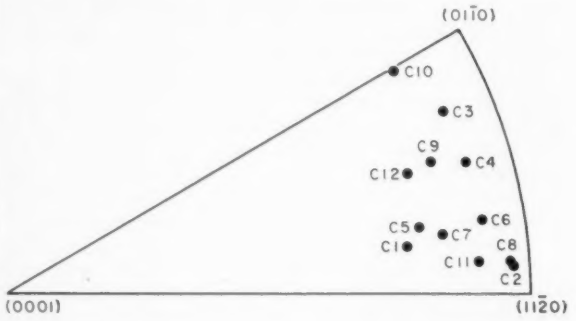

FIGURE 3. *Poles of planes on which stress-corrosion cracks were initiated.*

TABLE 1. *Components of stress normal to the plane of stress-corrosion cracks, and probability of slip at a constant stress, $f(\phi, \lambda)$, for crystals (C) containing and crystals (N) free from stress-corrosion cracks.*

$f(\phi, \lambda) = \sin \phi \cos \lambda$, where ϕ and λ are angles between the stress axis and the slip plane and slip direction, respectively.

Crystal	Angle between tension axis and normal to stress-corrosion crack	Component of the tensile stress normal to stress-corrosion crack	Probability of slip at constant stress
	deg		*sin ϕ cos λ*
C 1	12	0.978	0.000
C 2	2	.999	.008
C 3	21	.934	.028
C 4	18	.951	.031
C 5	10	.985	.043
C 6	9½	.98	.071
C 7	16	.961	.071
C 8	4½	.997	.071
C 9	7½	.991	.074
C 10	10	.985	.078
C 11	16½	.959	.079
C 12	15	.966	.114
N 1			.023
N 2			.091
N 3			.149
N 4			.150
N 5			.162
N 6			.201
N 7			.342
N 8			.365
N 9			.405
N 10			.472

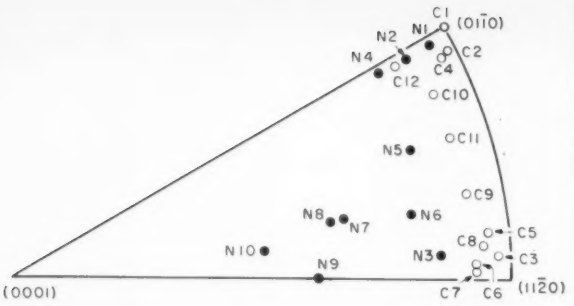

FIGURE 4. *Tension axes for crystals "C" in which cracking occurred and for crystals "N" in which no cracks were found.*

The ease with which slip will occur in a given crystal is dependent, in part at least, on the magnitude of the product $\sin\phi \cos\lambda$, where ϕ is the angle between the stress axis and the slip plane and λ is the angle between the stress axis and the slip direction. The slip plane is (0001) and the slip direction is [11$\bar{2}$0] for polycrystalline magnesium [9] and it is to be expected that they are the same for the AZ31 alloy. The values of $\sin\phi \cos\lambda$ have been calculated for each of the 12 crystals in which cracks were analyzed and for 10 crystals, from some of the same specimens, in which no cracks were found. These data are given in column 4 of table 1. The tension axis, with respect to each crystal, is plotted in a single stereographic triangle, in figure 4.

Data in table 1 and figure 4 indicate that crystals in which cracking occurred were generally less favorably oriented for slip than those crystals analyzed in which no cracks were found. It is recognized that in polycrystalline specimens the neighboring crystals may be the determining factor in whether or not slip occurs in a particular crystal. However, the fact that the stress-corrosion cracks occurred in the crystals least favorably oriented for slip is in agreement with the mechanism postulated earlier for the initiation of stress-corrosion cracking in the magnesium alloy.

4. Summary

1. Idealized curves were prepared showing the simultaneous changes in extension and electrochemical solution potential for AZ31B magnesium alloy specimens that were exposed under constant tensile load in an aqueous solution of NaCl and K_2CrO_4 until failures by stress-corrosion cracking occurred.

2. Initiation of stress-corrosion cracking, after an incubation period, is postulated to occur in grains that were deformed as the result of stress-concentrations built up by the initial deformation and the hardening of those grains that were favorably oriented for initial plastic extension.

3. Making several assumptions, the strain rate (in microscopic sections) associated with, and most probably required for, the initiation of stress-corrosion cracking was calculated to be of the order of 1 percent/sec.

4. The incubation period (period prior to initiation of cracking) was much longer for specimens on which the passive (film covered) and active (film free) areas were approximately the same than for those on which the passive area was many times larger than the active area.

5. Stress-corrosion cracks made large angles with the basal crystallographic plane in large-grained specimens but were not generally associated, at their initiation, with any low-index crystallographic plane.

6. Stress-corrosion cracks were generally approximately normal to the stress axis and occurred in grains unfavorably oriented for slip.

This project has been sponsored jointly by the Corrosion Research Council and the National Bureau of Standards. The author appreciates the assistance of Joan Calvert, June Chung Fugh, James G. Early, Jr., Joseph E. Himes, and Howard T. Yolken in the experimental work in this investigation.

5. References

[1] H. L. Logan and H. Hessing, J. Research NBS **44,** 233 (1950) RP2074.
[2] H. L. Logan, J. Research NBS **61,** 503 (1958) RP2919.
[3] H. L. Logan, Physical metallurgy of stress corrosion fracture, Edited by Thor Rhodin, p. 298 (Interscience publishers, New York, N.Y., 1959).
[4] C. S. Barrett, Structure of metals, p. 40 (McGraw-Hill Book Co., New York, N.Y., 1952).
[5] H. L. Logan, J. Research NBS **48,** 99 (1952) RP2291.
[6] T. P. Hoar and J. M. West, Nature **181,** 835 (1958).
[7] D. K. Priest, F. H. Beck, and M. G. Fontana, Trans. ASM **47,** 473 (1955).
[8] R. D. Williams, Motion picture film of stress-corrosion cracking of magnesium alloy produced by Aluminum Company of America Research Laboratories.
[9] F. E. Hauser, C. D. Starr, L. Tietz, and J. E. Dorn, Trans. ASM **47,** 102 (1955).
[10] F. Meller and M. Metzger, US NACA Tech. Note (1957) No. 4019.

(Paper 65C3–67)

JOURNAL OF RESEARCH of the National Bureau of Standards—C. Engineering and Instrumentation
Vol. 65C, No. 3, July–September 1961

Coatings Formed on Steel by Cathodic Protection and Their Evaluation by Polarization Measurements

W. J. Schwerdtfeger and Raul J. Manuele.*

(March 2, 1961)

Three steel specimens were continuously exposed in the laboratory for almost 5 years in city water to which was added 3 percent by weight of sodium chloride. Two of these specimens were under continuous cathodic protection, one by current from a zinc anode, and the other by current from a rectifier through a carbon anode. The third specimen was left to corrode freely.

As a result of the cathodic protection, carbonates and silicates formed protective coatings which eventually reduced the current density required for protection from about 5 to 0.02 ma/ft². A coated specimen, after being without protective current for 32 days (including 12 days out of the salt water), required only 0.3 ma/ft² for initial protection.

The instantaneous corrosion rates on the coated specimens (scratched and unscratched) while without protective currents were measured by changes-in-slope (breaks) in polarization curves. The currents at which breaks occurred in the cathodic curves were found to be related to $\Delta V/\Delta I$ values from the curves which values in turn bore a relation to the corrosion rates as measured by weight loss.

1. Introduction

When cathodic protection is mentioned in conjunction with coatings for protecting steel structures against corrosion, the coatings referred to are invariably organic in nature. Relatively little is said of the benefits of the inorganic or natural coatings such as carbonates or silicates which can be deposited as a result of cathodic protection and which the authors have found to be quite corrosion-resistant in a salt water environment. Although the protective character of such coatings, not necessarily in connection with cathodic protection, has been emphasized by other investigators it is believed that the present discussion will be of additional value and interest because the very nature of cathodic protection when properly applied is such as to automatically keep these coatings in a state of repair.

Speller [1] [1] states that silicious and carbonaceous coatings are sometimes formed on metal surfaces by adsorption in the atmosphere, underwater, and in soils, and often act as the main natural agency opposing corrosion.

Evans [2] in talking about the behavior of zinc-coated steel continually immersed in water has suggested that the carbonate electrochemically deposited on the steel, when the zinc goes into solution, may persist even after all the zinc has disappeared.

In some of the early NBS soil corrosion tests, Logan [3] attributed the protective effect of the zinc coating on galvanized pipe specimens to a protective film found on the surface of the zinc rather than in cathodic protection by the zinc. Later, Denison and Romanoff, [4] in reporting on the behavior of galvanized steel specimens exposed to corrosive soils for 13 yr, tentatively attributed their remarkable corrosion resistance in alkaline soils to a film or coating, probably silicious in nature, that was deposited cathodically by galvanic action between the remaining zinc coating and the alloy layer on the underlying steel. The protection of the steel was obvious even though the outer zinc coating had been virtually removed by corrosion.

Hoar [5] in a private communication suggested that the protection produced by the cathodic deposition of calcium carbonate on a metal surface can persist in many cases long after the cathodic current is stopped.

Pearson [6] associates the useful ampere-hour effect of cathodic protection on ferrous materials underground with a film formed by the precipitation of insoluble carbonates. He describes the "film" formed as being effective even when barely visible and building up with time.

This paper describes the effects observed by cathodically protecting cold-rolled steel rods exposed to city water to which was added 3 percent by weight of sodium chloride. It is shown how the effectiveness of the coatings formed on the steel surfaces can be evaluated by the means of polarization measurements. The applied currents associated with changes-in-slope of the current-potential curve during cathodic polarization are shown to be related to the corrosion caused by physically disturbing the uniformity of a coating. The study extended over a period of almost 5 yr.

*Professor of Chemistry, University of La Plata, La Plata, Argentine Republic.

[1] Figures in brackets indicate the literature references at the end of this paper.

2. Experimental Procedure

The experiments to be described started out as a simple demonstration of cathodic protection for students spending their vacations working on various projects at NBS. A ½-in. diam rod of cold-rolled steel was coupled to a zinc rod through a milliammeter and exposed to Washington City water to which had been added 3 percent by weight of sodium chloride. The steel rod was protected by tape at the water line and had approximately 0.1 ft^2 of surface (9 in. of its length) exposed to about 17 liters of the salt water contained in an open Pyrex jar. Henceforth, all currents will be expressed as apparent current densities in ma/ft^2 or ma/dm^2. During initial exposure, the galvanic current rapidly diminished from 200 ma/ft^2 to 10 ma/ft^2 and after 3 weeks of exposure was down to 6.0 ma/ft^2 at which time the rod was removed from the water, washed under running water, and examined. A white chalklike coating which could readily be scratched off was noticeable on the lower end of the rod. The rod was put back into the water and again coupled to the zinc. As time went on, the galvanic current became smaller until, after 1 yr of exposure, it was 0.5 ma/ft^2. During the exposure period it was observed that the potential of the steel, with reference to a saturated calomel half cell (used throughout this investigation), was about −1.0 v when read immediately after breaking the galvanic circuit. After the circuit had been broken for 1 min, the potential of the steel was still between −0.85 and −1.0 v. At the end of the year, the rod was uniformly covered with the chalky deposit (2 to 3 mils thick) containing zinc silicate as shown by the X-ray diffraction powder pattern analyses. Figure 1 is a photograph of the rod showing the white coating. On this occasion, no rust was in evidence, anywhere, even under the tape laps.

Upon the conclusion of the foregoing experiment 3 additional weighed steel specimens, prepared as the one previously described, were individually exposed in 3 Pyrex jars each containing 17 liters of city water to which had been added 3 percent by weight of sodium chloride. One specimen, No. 1, was left to corrode freely and act as a control. Specimen No. 2 was connected galvanically to zinc and specimen No. 3 received protective current from a ½-in. diam carbon rod fed by a copper oxide rectifier. Here again, the specimens were set up primarily for demonstration purposes, but protective currents were measured from time to time as were the potentials of specimens Nos. 2 and 3 under cathodic protection. The water level in the open jars was never permitted to drop below the tape line, makeup city water being added weekly to compensate for evaporation loss.

After 12 months the 3 specimens were removed from the jars, cleaned and reweighed. The specimens were put back into the same jars and electrolyte from which they had been removed. The specimens were not removed from the electrolyte again, except for brief periods, until the 56th month and finally

FIGURE 1. *Inorganic coating formed on steel cathodically protected by zinc for one year in a 3 percent sodium chloride solution.*

for chemical analysis of the coatings formed on the specimens under cathodic protection, and for cleaning and reweighing after 57 months of exposure.

Until the 55th month, specimens Nos. 2 and 3 were continually under cathodic protection except for relatively brief periods which will be discussed later. The potential of specimen No. 2 (connected to the zinc) was always well within the protective range because of the good conductivity of the electrolyte, while the potential of specimen No. 3 was always at least at −0.77 v and usually more electronegative. After 34 months exposure, a potentiometer was shunted across the secondary of the rectifier supplying specimen No. 3 and the applied voltage adjusted to a value consistent with maintaining a minimum protective potential of approximately −0.77 v. By this time, a uniform natural coating was in evidence on specimen No. 3 and it was found on further reductions in the current applied to No. 3, after 52 months, that it was easily possible to maintain a polarization potential of −0.77 v with 0.1 ma/ft^2. In fact, even with this low-current density the potential of specimen No. 3 was usually more electronegative than −0.77 v.

During the last 3 months of exposure cathodic polarization curves were obtained on specimens Nos. 2 and 3. Curves were also obtained on specimen No. 1 (freely corroding) before and after the removal of the heavy accumulation of corrosion products. After cleaning, curves were obtained during a 14-day exposure period to provide data on the initial corrosion rate of the unprotected rod and for comparison with the curves obtained on specimens 2 and 3.

Potential checks were made with a 200,000 ohms/v voltmeter. Polarization data were obtained with a two-pen (current and potential) strip chart electronic recorder. The polarizing current was varied by linear increments in the applied voltage which were obtained with a synchronously driven 10-turn potentiometer. The Holler null circuit described in a previous paper [7] was used in conjunction with the recorder but IR-drop compensation was unnecessary in the low-resistivity electrolyte.

3. Electrical Measurements and Observations

The more important information in this study pertains to the significance of the polarization data and the discussion later pertaining to the formation of the natural coatings and their importance in cathodic protection. Before discussing the polarization data, however, some of the prior observations on specimens Nos. 1, 2, and 3 or in order.

The potentials, currents and other observations pertaining to these specimens during the first 12 months of exposure are of interest. Until the end of the first month specimens Nos. 2 and 3 each received 5.0 ma/ft^2 of protective current, with the potential of No. 2 around −0.97 v and No. 3 at −0.90 v. After the first month, the protective galvanic current on specimen No. 2 rapidly diminished to 0.6 ma/ft^2 for at least 6 months of the year and never exceeded 1.2 ma/ft^2. On the other hand, the current applied to specimen No. 3 usually varied between 5 and 13 ma/ft^2. The potentials for specimen No. 2 varied during the year between −0.97 v and −1.0 v while the potential for specimen No. 3 varied between −0.80 v and −0.97 v, averaging about −0.85 v. All potentials were read while the anode was momentarily disconnected. During the year, the voltage applied between the carbon anode and specimen No. 3 was very close to 2 v, so it can be assumed safely that the driving voltage was greater than the driving voltage between the zinc anode and specimen No. 2, even allowing for considerable anodic polarization of the carbon anode. At the end of the year, the 3 specimens were removed for examination, cleaning and reweighing. Specimen No. 1 was cathodically cleaned in salt water at a current density of 1 amp/ft^2 for 3 hr and then wire-brushed by hand to the bare metal. The specimen lost 4185 mg during the first 12 months which is equivalent from Faraday's Law (assuming 100% corrosion efficiency) to an average corrosion current density of about 4.6 ma/ft^2. Specimens Nos. 2 and 3 were washed under hot running water and examined. Number 2 had a fairly adherent coating, similar to that formed on the preliminary demonstration specimen exposed earlier. Although no rust was visible, the specimen was subjected to a cathodic current density of 1 amp/ft^2 for 1 hr. After considerable wire-brushing and reweighing, specimen No. 2 weighed 110 mg more than before exposure. The increase in weight was attributable to the coating which was still visible after the wire-brushing. Similar treatment of specimen No. 3, also without evidence of corrosion, revealed an increase in weight of only 10 mg. Before cleaning, specimen No. 3 had a dark-green appearance. Thus, during the first year, the coating formed on specimen No. 2 was apparently superior to that on specimen No. 3. This explains the lower current density required to protect specimen No. 2.

After the 3 specimens were cleaned and reweighed they were put back into their respective jars with no other changes. Currents and potentials were about the same during the next year as they had been previously. After 24 months of exposure, specimen No. 3 was taken out of the salt water for a few hours. It was brushed under hot running water with a brass-bristle brush, permitted to dry and then weighed. The coating now weighed about 25 mg and its appearance was the same as after 12 months. The specimen was put back into the salt water with cathodic protection. After 33 months of total exposure time the protective current, which was 3 ma/ft^2 at the time, was temporarily removed from specimen No. 3. Immediately after opening the circuit, the potential was around −1 v. After 5 min, the potential was −0.82 v and after 35 min with no protective current the potential was −0.77 v. The protective current was then restored at an arbitrarily reduced value of 1 ma/ft^2 which soon polarized the steel to −0.8 v. The next day the potential was −0.84 v and the current 0.5 ma/ft^2, a condition that persisted for the next 7 days. The applied voltage between the carbon anode and the steel specimen was further reduced to 1.45 v and it was found that for several days 0.25 ma/ft^2 was sufficient to hold the potential at −0.77 v. During the next 18 months the current density varied between 0.1 and 0.5 ma/ft^2 except for one occasion when it went to 1 ma/ft^2 when the power failed over a weekend. This resulted in a pinhole through the natural coating as evidenced by a spot of rust. The coating soon re-formed over this spot and the current again gradually lowered until, between the 52d and 55th months of exposure it varied between 0.1 and 0.25 ma/ft^2 with the potential around −1.0 v. At these relatively low-current densities no attempt was then made to reduce the current further but it was obviously possible to do so, as will be shown later, in view of the potential.

An experience with specimen No. 2 was also rather enlightening. After 42 months exposure, the zinc anode was disconnected and the potential of the specimen measured at intervals during a period of 8 hr. Prior to opening the circuit the protective current was 0.5 ma/ft^2. Immediately after breaking the anode circuit, the potential of the specimen was

−0.96 v and after 30 min it was −0.83 v. After 1 hr without protective current, the potential was still −0.78 v and after 6½ hr it was −0.62 v with no visible evidence of rusting. The protective current was left off over the weekend. After 64 hr the potential was −0.665 v and two small spots of rust were evident on the coated surface, otherwise there was no evidence of corrosion. The rust was brushed off and the specimen put back into the solution under protection by the zinc. Over the weekend, although no measurements were made, the potential probably rose to a value somewhat more noble than −0.62 v and then when breakdown of the points on the surface occurred, the potential gradually drifted in the more electro-negative direction. A similar potential drift in the noble direction was noted on steel specimens in soils [8] after protective currents were removed and then a reversed trend in potential drift as corrosion again commenced.

A repetition of the foregoing experiment followed by polarization measurements was conducted on specimen No. 2 after 56 months total exposure time. At this time, the galvanic current had decreased to 0.1 ma/ft² from a value of 0.5 ma/ft² on the previous occasion. Within a few sec after opening the galvanic circuit the potential of the steel was −0.92 v at which time a cathodic polarization curve was obtained, The polarization was rather rapid, $\Delta V/\Delta I$ being 1000 mv/ma from 0 to 1 ma/ft². After running the curve, the potential of the specimen which had been left on open circuit drifted to −0.77 v in 2½ hr, and after 3½ hr the potential was −0.75 v. Twenty-one hours later, the potential was −0.64 v and there was no visible evidence of corrosion. Cathodic polarization curve A, figure 2, was obtained at this time. This was the first of a series of curves taken on this specimen during the following 36 days to show how damage of the coating affected the polarization, and the effect on polarization of removing the specimen from the salt water, esposing it to the indoor atmosphere for 12 days and then putting it back into the same water again.

Curve B, figure 2, shows the polarization of specimen No. 2 after 45 hr without protective current when the first visible evidence of rust appeared about 2.5 in. below the waterline, or around 1 in. below the lower edge of the tape. Curve C, was obtained after 5 days without protective current and then the specimen was removed from the water in order to scrape off some of the coating about 3 in. below the lower edge of the tape. The coating was removed in the form of a 0.2 in. wide band encircling the rod. Curve D, obtained the next day, shows the effect of the coating removal on the polarization. Curve E, was obtained after 12 days without protective current, no additional corrosion being visible other than on the two areas just mentioned. On the 14th day without protective current, this specimen was removed from its corrosive medium and exposed to the air for 12 days with the other two specimens. Just prior to putting specimen No. 2 back into the salt water, a little dilute hydrochloric acid was placed on a small area of the coating. Gas evolution, indicative of a carbonate coating, was observed. The specimen was then rinsed under running water and returned to the salt water from which it had been removed. The next day, curve F, figure 2, was obtained. There was some visible evidence of rust on the area touched by the acid the previous day. During the next 10 days there was no evidence of increased corrosion. On the 36th day without cathodic protection the final cathodic polarization curve, G, was obtained. After stabilization of the specimen potential, an anodic polarization curve was run. The specimen was then removed from the water for a spectrographic analysis of the natural coating formed during the 57 months of exposure and for reweighing of the specimen after removal of the coating. The anodic polarization was purposely left until the end of the experiment to avoid the possibility of disturbing the coating. The significance of the polarization curves will be discussed later.

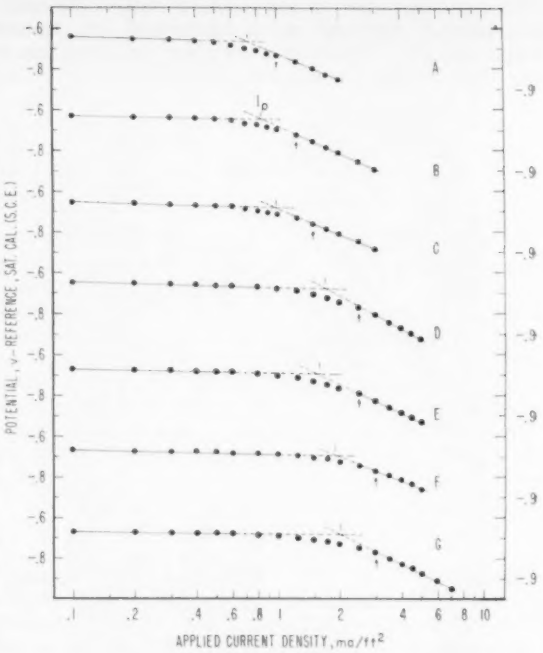

FIGURE 2. *Cathodic polarization of an inorganically coated steel specimen, No. 2, in a 3 percent sodium chloride solution, as affected by progressively damaging the coating during a period of 36 days without cathodic protection.*

Polarization rates $\Delta V/\Delta I$, mv/ma, through the range of applied current (density ×0.1) indicated by the arrows are as follows: A, 940; B, 808; C, 707; D, 520; E, 504; F, 320 and G, 353.

Similar polarization studies were made on specimen No. 3 except that no attempt was made to intentionally disturb the natural coating. After 55 months exposure, the protective current on specimen No. 3 was 0.1 ma/ft² and a quick reading of its potential upon removing the current gave −1.05 v. After the circuit had remained open for 5 min, the potential was still −0.98 v. A potential-time study was then

carried out by use of the potentiometer-recorder. After 35 min without protective current, the potential was −0.97 v. Note the relatively slow decay in potential as compared with that observed in a similar experiment, previously described, after 33 months exposure. After 24, 48, 72, and 96 hr, the potentials were −0.89 v, −0.81 v, −0.81 v, and −0.76 v, respectively. The potential continued to drift in the electropositive direction until on the 9th day without protective current, the potential was −0.65 v with no visible corrosion. Cathodic polarization curves obtained on specimen No. 3 during this initial 9-day period without protective current showed that the polarization rate (designated $\Delta V/\Delta I$) was relatively high in comparison with that observed on the corroding specimen No. 1.

The protective current from the rectifier was again applied to specimen No. 3 and left on for 12 days. Within 4 hr, the potential was −0.84 v and the current density 0.3 ma/ft². After 7 days, the current density was 0.03 ma/ft², the potential −0.90 v. On the 10th day, the applied voltage from the rectifier was reduced to 1.33 v between anode and cathode. On the 12th day, the potential of the specimen was −0.85 v and the protective current density was 0.02 ma/ft². Cathodic polarization from this potential revealed $\Delta V/\Delta I$ as being 3400 mv/ma between 0 and 0.5 ma/ft² of applied current density. On the 12th day the protective current was removed and the specimen left without protection. After 24, 48, and 96 hr, the specimen potential was, −0.83 v, −0.80 v, and −0.76 v, respectively. After the second 9-day period without protection specimen No. 3 was removed from the salt water and exposed to the air in the laboratory for 12 days. This was followed by 11 additional days of exposure without protection to the same salt water from which it had been removed. Cathodic polarization curves were obtained during the two 9-day periods preceding exposure to the air and during the following 11-day period. The polarization runs were made at times when some corrosion could have been taking place, that is, when the specimen potential was electropositive to −0.77 v as shown by a previous study [9]. These cathodic curves are shown in figure 3. Curve A, was obtained on the 4th day, curve B, on the 9th day of the initial 9-day period, and curves C, D, and E during the second 9-day period preceding air exposure. Curves F and G cover the final 11-day period of exposure to the salt water. On the final day of salt water exposure, an anodic polarization curve was also obtained on specimen No. 3, after which it was removed from the salt water, washed under running water and permitted to air dry. This was followed by a spectrographic analysis of the coating, quantitative analysis for carbonates in the coating and finally, removal of the coating and reweighing.

The anodic polarization curves obtained on the final day that specimens Nos. 2 and 3 were exposed are shown in figure 4. The eventual superiority of the coating on specimen No. 3 as compared with that on specimen No. 2 is shown by the higher polarization rate of specimen No. 3. This will be discussed in more detail later in the paper.

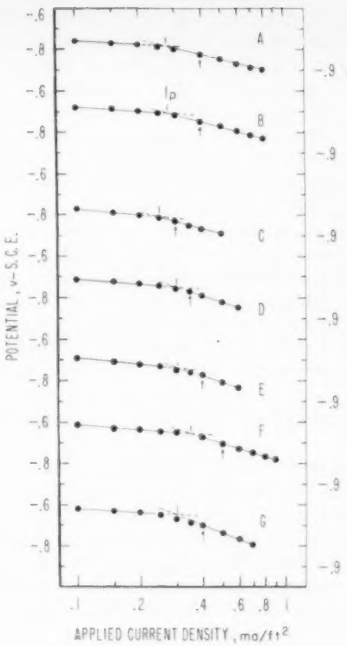

FIGURE 3. *Cathodic polarization of an undistrubed inorganically coated steel specimen, No. 3, in a 3 percent sodium chloride solution for 29 days without cathodic protection.*

Polarization rates, mv/ma, are as follows: A, 2100; B, 2400; C ,2670; D, 2570; E 2600; F, 1960; G, 2500.

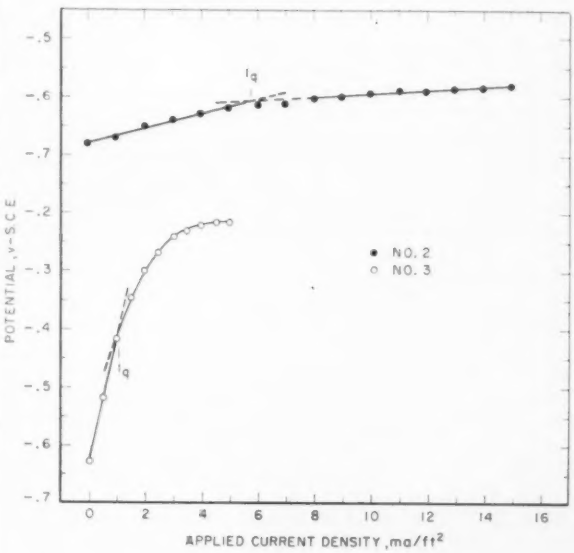

FIGURE 4. *Anodic polarization of specimens Nos. 2 and 3 on the final day of exposure corresponding with the time when curves G (figs. 2 and 3) were obtained.*

In order to compare the polarization of specimens No. 2 and 3 having inorganic coatings with that of the unprotected specimen, No. 1, the curves shown in figure 5 were obtained. Curves A and B were run while the specimen was covered with the thick accumulation of rust, curve A before removing the rod for exposure to the atmosphere for 12 days, curve B after the rod had been back in the salt water for 11 days following atmospheric exposure. Curves C through H were obtained on the same specimen during a 14-day exposure period after removing all the corrosion products and reexposing to the same solution. The specimen was weighed before and after the 14-day exposure period and anodic curves (fig. 6) were obtained to permit comparison of the calculated and actual weight losses during the period.

4. Interpretation of the Polarization Data

The purpose of the discussion which follows is to show how the applied currents associated with changes-in-slope in polarization curves (usually referred to as breaks) are related to the actual polarization over a specific range of the applied current (cathodic current here, because cathodic control predominated) and to show the relation between these data and the rates of corrosion. Similar relationships, with some variation, were previously shown for steel corroding in soils [10]. The significance of the slopes of polarization curves in relation to rates of corrosion has since been discussed by others, namely, Simmons [11], Skold and Larson [12], and Stern [13].

Curves A and B, figure 5 were the only cathodic polarization curves obtained on specimen No. 1 (corroding freely) during the long exposure period, and while the specimen was covered with a thick adherent deposit of rust accumulated during almost 4 yrs of continuous exposure. Figure 7 shows the 3 specimens after 56 months of exposure to the salt water. The corrosion products on No. 1 are evident in the photograph. Reweighing of specimen No. 1 after the final cleaning revealed a weight loss of 11,835 mg during the intervening 1,356 days of exposure beginning after 12 months. Using the electrochemical equivalent ($K=2.8938\times10^{-4}$ g/coulomb) and assuming a corrosion efficiency of 100 percent, the average corrosion current density was calculated to be 3.5 ma/ft². It will be recalled that the average corrosion current density was 4.6 ma/ft² for the first 12 months. A dropping off of the corrosion rate with the passing of time is indicated. For this reason curves C through H, figure 5, and D through G, figure 6, were obtained to provide data on the corrosion rate of the clean steel rod during the first 14 days of exposure. The anodic curves, figure 6, are plotted on rectangular coordinate paper in order to permit a more accurate estimation of the current I_g, than was possible on logarithmic coordinates. The data shown in table 1 were obtained from figures 5 and 6 and are used to calculate [10] the weight loss over the 14-day period of exposure. The corrosion current decreased with time, being down to 6.8 ma/ft² after 10 days of exposure. The weight loss (299 mg) as calculated from the cathodic and anodic polarization curves compares reasonably well with the actual weight loss (280 mg).

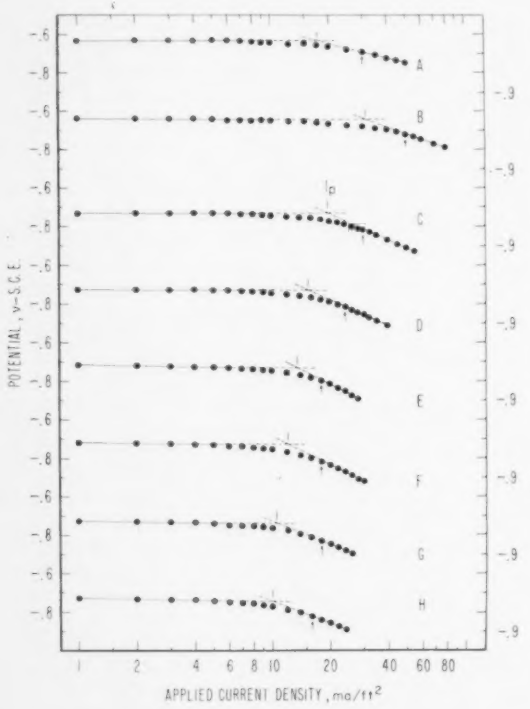

FIGURE 5. *Cathodic polarization of a bare steel specimen, No. 1, in a 3 percent sodium chloride solution.*

Curves A and B, after almost 4 years of exposure with 12 days of atmospheric exposure between polarization runs. Curves C through H, the same specimen after removing all corrosion products and exposing again to the same solution for 14 days. Polarization rates mv/ma are as follows: A, 21; B, 16; C, 29; D, 40; E, 47; F, 56; G, 58; H, 59.

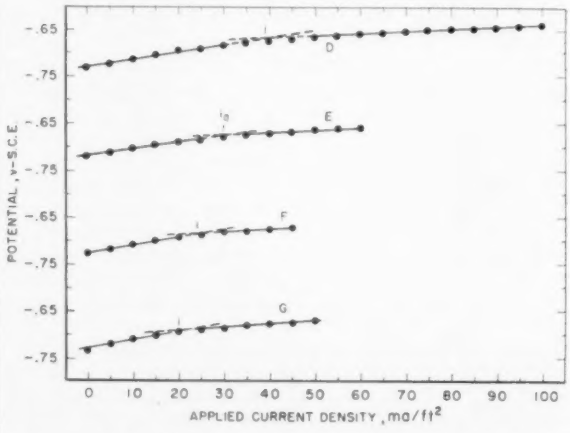

FIGURE 6. *Anodic polarization of specimen No. 1 during the 14 day exposure period mentioned in figure 5.*

Curves D, E, F, and G (fig. 5). were obtained on the same day, respectively, as curves D, E, F, and G (fig.5).

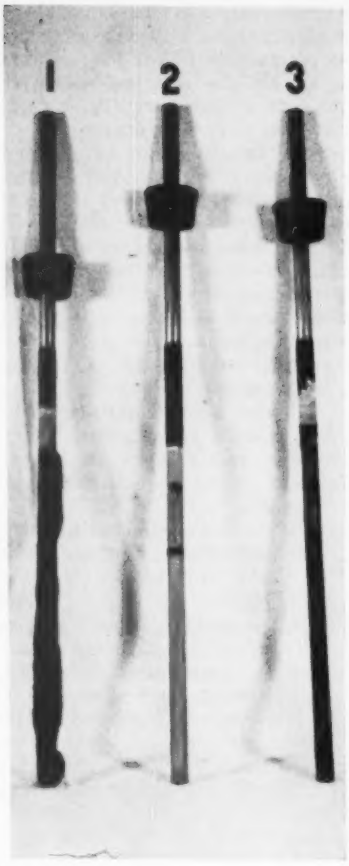

FIGURE 7. *Appearance of steel specimens Nos. 1, 2, and 3 before final cleaning.*

Rust spots account for most of the weight loss on specimen No. 2. The dark appearance below the tape on No. 3 is not rust but the color of the inorganic coating.

TABLE 1. *Weight loss on specimen No. 1 caused by corrosion in 14 days*

Calculations from polarization data (figs. 5 and 6)

Exposure time	Polarizing current [a] at break in curve		Corrosion [b] current i_o	Weight loss	
	Cathodic, I_p	Anodic, I_q		Calculated [c] cumulative	Actual
Days	*ma*	*ma*	*ma*	*mg*	*mg*
1	1.95 C	4.9 [d]	1.4	35	----------
2	1.55 D	3.9 D	1.1	66	----------
4	1.35 E	3.0 E	0.93	116	----------
7	1.20 F	2.4 F	.80	180	----------
10	1.05 G	2.0 G	.68	234	----------
14	1.00 H	1.9 [e]	.65	299	280

[a] Measured values (density ×0.1)—The capital letter following value of current designates the curve in fig. 5 or fig. 6 from which the value is obtained.

[b] $i_o = I_p I_q/(I_p+I_q)$.

[c] Weight loss (g) $= Kti$, where $K = 2.8938 \times 10^{-4}$ g per coulomb, $i = i_o$ = average current (amperes) for the period t in seconds) between successive readings. For the period before the initial polarization run, the initial value of i_o was taken as average.

[d] Based on the ratio I_q/I_p of the 2d day.

[e] Based on the ratio I_q/I_p of the 10th day.

The high values of I_p (curves A and B, fig. 5) are not consistent with the corrosion rate, which presumably was at its lowest value when the data for these curves were obtained. Of course, there is no way of knowing what the corrosion current actually was at the time, except that it should be about equal to the average value (3.5 ma/ft²) previously calculated, based on the assumption that the corrosion rate was relatively stable for a long time. The answer does not lie in a change to anodic control, because an anodic polarization curve (not shown), obtained after curve B, showed that cathodic control predominated. It appears as though more work ought to be done to determine the effects of a heavy accumulation of corrosion products on polarization of the basis metal.

After 56 mo exposure and before finally completing the experiment it was decided, as previously mentioned, to leave specimen No. 2 without protective current, observe the effect of scratches in the coating on polarization and possibly measure the actual corrosion which had occurred. The polarization data for specimen No. 2 are shown in figures 2 and 4 and the corrosion calculations based on these data in table 2. The only other time in almost 5 yr of exposure that this specimen was subject to any corrosion was for a portion of the 3-day period after 42 mo of exposure. Based on subsequent measurements (table 2), the weight loss because of corrosion during this period was probably less than 5 mg. The weight loss calculations are based mainly on the cathodic polarization currents, I_p, as the anodic curve (fig. 4) showed that the control was cathodic. Use of the ratio $i_o = 0.73\ I_p$ seems reasonable, in view of the data (table 1) obtained on specimen No. 1. Thus, for all practical purposes, in view of the agreement between actual and calculated weight losses, increases in I_p were indicative of increases in corrosion rate. This was reflected in curve D (fig. 2) as a result of a scratch in the coating purposely made on the preceding day. There was also some indication that exposure to the atmosphere for 12 days or the disturbance of the coating by a drop of dilute acid just prior to immersion increased the corrosion current (curve F).

The cathodic polarization curves (fig. 3) for specimen No. 3 cover three periods when there was no protective current. Although no corrosion was visible at any time during these periods, and no attempt was made to scratch the coating, the potentials at zero current (substantially the same as those shown for the lowest current on the abscissa) are electropositive to the protective potential −0.77 v and hence it was assumed that the possibility of corrosion, however slight, did exist. This does not imply that the potentials per se gave proof of corrosion, but that the potentials (fig. 3) were in the same range as were the potentials of specimen No. 2 (fig. 2), when corrosion was known to be taking place. Thus, No. 3 was in the salt water for 29 days without protective current and for 21 days it is assumed, on the basis of the potential, that some corrosion could have occurred. During the almost 5 yr that this specimen was under cathodic protection, there was only one

TABLE 2. *Weight loss on specimen No. 2 resulting from corrosion due to scratches in the coating*

Corrosion is calculated from the polarization data (figs. 2 and 4).

Exposure time	Polarizing current [a] at break in curve		Corrosion [b] current i_o	Weight loss	
	Cathodic I_p	Anodic I_q		Calculated [c] cumulative	Actual
Days	*ma*	*ma*	*ma*	*mg*	*mg*
1	0.072A	----------	0.053	1.3	----------
2	.084B	----------	.061	2.7	----------
5	.098C	----------	.071	7.6	----------
6	.17D	----------	.12	10.0	----------
12	.16E	----------	.12	28.00	----------
14	(d)	----------	----------	34.0	----------

The specimen was removed from the salt water on the 14th day and put back in again on the 26th day. Corrosion during this interim (12 days) was considered as negligible.

27	.19F	----------	.14	37.5	----------
37	.20G	0.55 [e]	.15	75.0	70

[a] Measured values (density ×0.1). The capital letter following a value of current designates the curve (fig. 2) from which the value is obtained.
[b] $i_o = I_p I_q/(I_p + I_q)$, based on I_q/I_p ratio for the 37th day or $i_o = 0.73\ I_p$.
[c] Same as footnote [c], table 1.
[d] Used 0.16 ma for I_p.
[e] From fig. 4.

occasion, over a weekend, when the current accidentally went off, as described in the previous section. The only anodic polarization curve on specimen No. 3 was obtained on the last day of exposure and is shown in figure 4. Based on this curve and curve G (fig. 3), the ratio I_q/I_p=approx. 3, and therefore, $i_o = 0.75\ I_p$. Using the value I_p=0.03 ma (specimen area = 0.1 ft^2) from figure 3 as the average value for 21 days and calculating as previously, the calculated weight loss was about 12 mg. The actual weight loss during the 5 yr was 35 mg. The only visual evidence of corrosion on the cleaned specimen was on the lower-half of the taped area and also above the tape, where salt had crystallized and penetrated the oil film. As the calculated corrosion would not include the area above the tape which was out of the solution, the calculated value seems to be quite reasonable.

It is known from experience that there are times when it is difficult to observe significant breaks in polarization curves. The relative importance of cathodic and anodic polarization curves in estimating rates of corrosion was discussed several years ago [10]. It was observed that, for steel in soils, a relation existed between the rate of polarization ($\Delta V/\Delta I$ resulting from externally applied current) and the applied current I_p (at the break in curve). It was also shown that both of these factors were related to the instantaneous rates of corrosion. The most useful values of ΔV seemed to be those potential changes which occurred in a range of applied currents of the order of I_p or slightly larger.

Simmons [11] found that inhibitors could be evaluated by $\Delta E/\Delta I$ (called $\Delta V/\Delta I$ in this paper) from polarization curves. Small current densities caused changes in potential on exposed steel of 100 mv and more. In figures 2 and 3 of Simmon's paper are shown cathodic curves for steel in salt water with and without the inhibitor $Na_2\ CrO_4$. We noted that in both of Simmon's figures the changes in potential of the d-c null curves, from the lowest currents to the values at the breaks (corresponding to our I_p values), are about equal. As these currents were of the relative magnitude of 10 to 1, Simmon's conceded this to be the relative magnitude of the corrosion currents which were either comparable in magnitude or less than the currents at the breaks in his curves. Thus, the ratios $\Delta E/\Delta I$ for these data were in the reverse order, namely 1 to 10.

Skold and Larson [12] showed that an empirical relation existed between the slopes ($\Delta E/\Delta I$) of polarization curves for low values of applied current and the corrosion rates of steel in fresh water as determined by weight losses. They first tried correlating the breaks in polarization curves with corrosion rates but abandoned this in favor of the slope method. It is believed that the use of a null circuit is necessary for the detection of breaks in polarization curves obtained with a 3000 ohm-cm solution such as was used by Skold and Larson. Nevertheless, their straight line relationship on logarithmic coordinates between corrosion rate and $\Delta E/\Delta I$ seems to have considerable merit. This has been further substantiated by the data reported in this paper.

Stern [13] has published the theoretical basis for the method of Skold and Larson. He has stressed the importance of applying polarizing currents which are smaller than the presumed corrosion currents in order to avoid marked polarization with resultant possible changes in the inherent rates of corrosion. Apparently, the inherent rates of corrosion observed in the present study were unaffected by the applied currents which at the end of a run were often 4 times the magnitude of the corrosion currents. This is also true of previous studies [7, 9] where controls subjected to reasonable amounts of polarization lost no more weight than those on which no polarization runs were made. Possibly the short polarizing time (10 to 15 min) is beneficial in negating this tendency.

The polarization data (figs. 2 to 6 incl.) were plotted from the strip chart records for additional interpretation and condensation. Furthermore, on the logarithmic current scale, the straight line portion of the cathodic curve, for applied currents larger than I_p, becomes helpful in estimating $\Delta V/\Delta I$. The values of $\Delta V/\Delta I$ shown in figures 2, 3, and 5 were calculated from changes in potential between zero applied current and the currents indicated by the arrows (beginning of straight line) where all local action corrosion is presumed to have ceased. Figure 8 shows the relation between $\Delta V/\Delta I$ and corresponding values of I_p for the 3 specimens. It is interesting to note that the plot of these parameters on the logarithmic coordinates results in a slope close to the theoretical value of minus one mentioned by Stern [13], although he considered corrosion current instead of the current I_p. Thus, figure 8 suggests, at least for steel in aqueous solutions, that a fairly constant ratio exists between the corrosion current and the current I_p. The calculations of weight loss in tables 1 and 2 are to some extent based on this premise. The small variations in the ratio i_o/I_p may be attributed to errors in selecting the break current I_q,

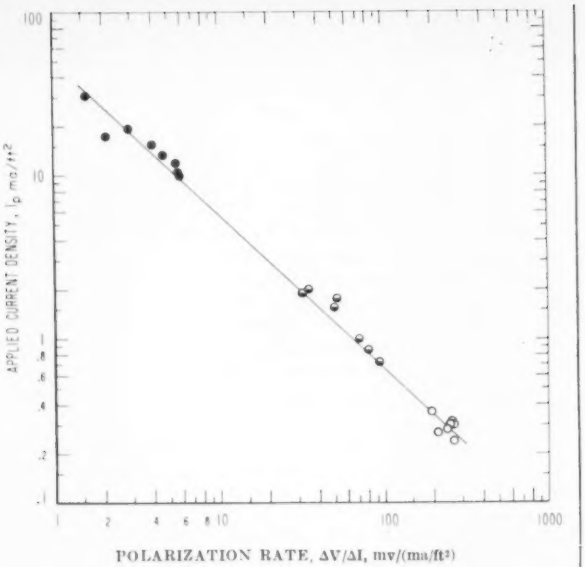

FIGURE 8. *Relationship during cathodic polarization of steel specimens Nos. 1, 2, and 3 between the current, I_p, at the break and the polarization rate, $\Delta V/\Delta I$, on logarithmic coordinates.*

●, Specimen No. 1 (fig. 5); ◒, No. 2 (fig. 2); ○, No. 3 (fig. 3).

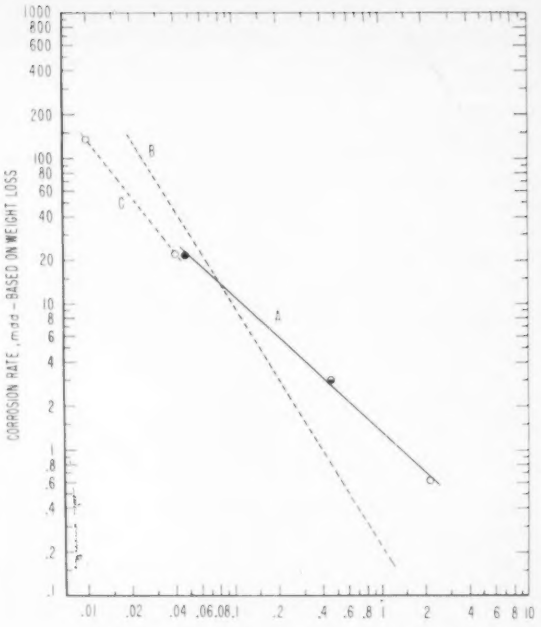

FIGURE 9. *Logarithmic relationship between actual corrosion (weight loss) and cathodic polarization rate of steel.*

Curve A (NBS), ● Specimen No. 1, ◒ No. 2, ○ No. 3 all in about 35 ohm-cm solution. Curves B and C [Skold and Larson] in 3000 ohm-cm water and 350–850 ohm-cm solution, respectively.

from the anodic polarization curves. The selection of I_q is more subject to error than I_p when the corrosion reaction is under cathodic control It is fortunate though that the accuracy with which the corrosion current can be calculated depends chiefly on the more significant curve which also lends itself to the better interpretation. In a case of corrosion under anodic control, this would be the anodic curve.

In order to further compare the data (fig. 8) with that of Skold and Larson, the actual weight losses of specimens 1 and 2 (tables 1 and 2) and the calculated weight loss of specimen 3 were related to the polarization rates $\Delta V/\Delta I$ in their units of measurement (fig. 9). The NBS weight losses, even though for only 3 specimens, carry considerable significance because of their range. The values are time-averaged and cover time periods of 14, 25, and 21 days, respectively, for specimens Nos. 1, 2, and 3. The calculated weight loss was used for No. 3 because, as previously stated, the actual value (35 mg) consisted chiefly of corrosion loss which occurred outside of the electrolyte and therefor could not be accounted for by the polarization measurements. Curves B and C were drawn from the data (fig. 1) of Skold and Larson [12]. Curve B covers approximately their range of data in the 3000 ohm-cm water and curve C is based on the mean value of each of two groups of their data. Curves B and C are subject to some resistance error, B more than C, as mentioned by Skold and Larson and also by Stern [13] and therefore have greater negative slopes than has the NBS curve, A.

5. Nature of the Coatings

After 57 months of exposure, approximately 50 mg of coating was taken from specimens Nos. 2 and 3 for analysis. The results of the spectrochemical analyses are shown in table 3. The coating of specimen No. 2 consisted mainly of carbonates (27% CO_3) and silicates associated with calcium, magnesium, iron, and zinc. As the coating was almost white in appearance, the iron content was probably at the lower limit of the indicated range. The coating on specimen No. 3 was primarily in the form of carbonates (56% CO_3) combined with decreasing amounts of calcium, magnesium, and iron, in that order. Some silicate was also present. The zinc and silicates apparently constitute the chief differences in coating composition of the two specimens. The coating of specimen No. 2 had both of these elements in considerable proportion, whereas, the coating on specimen No. 3 did not, it being chiefly calcium carbonate with minor amounts of magnesium carbonate and iron oxide. It was estimated that during the 57 months about 300 liters of city water, which accounted for the formation of the coatings, were poured into each specimen jar to replace the water lost by evaporation. A composite mineral analysis of the city water (District of Columbia) for the year 1958 (avg) is shown in table 4.

593949—61——3

The saline solution surrounding specimen No. 2 probably had a zinc ion concentration corresponding to the solubility product of zinc carbonate or hydroxide. Carbonates were evident as a sediment in the container. A sediment of carbonates was also very noticeable in the jar containing specimen No. 3.

The alkaline reactions that occur on the surface of steel during cathodic protection result in precipitates which either adhere to the metal surface as a coating or drop as a sediment. Some of the possible reactions are:

$$Ca^{++} + HCO_3^- + OH^- \rightarrow CaCO_3 + H_2O$$
$$Mg^{++} + HCO_3^- + OH^- \rightarrow MgCO_3 + H_2O$$
$$Fe^{++} + HCO_3^- + OH^- \rightarrow FeCO_3 + H_2O$$
$$Zn^{++} + HCO_3^- + OH^- \rightarrow ZnCO_3 + H_2O$$
$$2\,Fe^{+++} + 6(OH)^- \rightarrow Fe_2O_3 + 3\,H_2O$$
$$Mg^{++} + 2\,(OH)^- \rightarrow Mg(OH)_2$$
$$Zn^{++} + 1/n(SiO_3H_2)n + 2(OH)^- \rightarrow ZnSiO_3 + 2\,H_2O$$
$$Zn^{++} + 2(OH)^- \rightarrow Zn(OH)_2$$

As a result of the foregoing reactions, the compounds formed can recombine and form other molecular compounds. The proportion of any one compound in the composition of the precipitate depends upon its solubility and the constituents of the solution. Based on table 3, the coating on specimen No. 2 was, in addition to calcium carbonate, probably zinc silicate. It is believed that the large amount of silicates in the coating of specimen No. 2 can be attributed to the zinc in solution from the anode. This conclusion is reinforced by the general knowledge that zinc is effective in precipitating silicates out of solution. The relative absence of silicates in the coating on specimen No. 3 can only be attributed to the relative absence of zinc, as the solutions were similar, but a carbon rather than zinc anode was used for cathodic protection.

TABLE 3. *Results of spectrochemical analyses of coatings formed on specimens nos. 2 and 3*

Element	Specimen		Element	Specimen	
	No. 2	No. 3		No. 2	No. 3
Ag	VW	T	Li	T	T
Al	M	W	Mg	S	S
B	T	----	Mn	M	W
Ba	W	W	Na	M	M
Ca	VS	VS	Ni	W	VW
Cd	W	----	Pb	M	W
Co	VW	----	Pt	VW	----
Cr	W	VW	Si	VS	M
Cu	M	W	Sr	M	W
Fe	S	S	Ti	VW	----
K	VW	VW	Zn	S	M

NOTE: In general, VS means greater than 10%; S, 1 to 10%; M, 0.1 to 1.0%; W, 0.01 to 0.1%; VW, 0.001 to 0.01%; T, 0.0001 to 0.001%; ----, not detected.

The mechanism of electrophoresis may be a contributing factor in the formation of the coatings. Such a hypothesis would necessarily involve the attraction of positively-charged colloidal particles to the cathode. Although a highly conductive solution, such as 3 percent NaCl, is not a favorable environment for electrophoresis to take place, it is believed that over a long period of time the contribution of the mechanism to the formation of the coating, although perhaps taking place slowly, might be a significant factor. Thus, the formation of coatings on specimens Nos. 2 and 3 may then be attributed to two factors, first, the precipitation of relatively insoluble compounds, such as carbonates, silicates, and others in physical contact with the specimen surfaces and, second, the electrophoretic deposition of colloidal particles in the pores of the coating.

A cathodically protected surface promotes conditions favorable for the precipitation of carbonates, phosphates, hydroxides, and silicates. If the protective current is excessive as the coating forms, the alkalinity around the uncoated areas will promote additional precipitation farther from the cathode surface because of the diffusion of hydroxide away from the cathode. On the other hand, a reduction of the protective current, consistent with the protective potential requirement, would tend to lessen this diffusion. For the formation of a compact coating, the volume and mass of insoluble colloidal particles might also be considered. It is believed that both volume and mass of the colloids increase with time during the precipitation process. Excessive alkalinity around the cathode areas, for example as a result of too much current, will promote this increase because the precipitation begins further away from the cathodic areas. This will result in two unfavorable effects, first, a slowing down of the migration of colloids toward the cathode and, second, the inability of the larger colloids which do arrive at the cathode to fill in the pores of the coating already in the formative stage. On the other hand, lower alkalinity in the porous or uncoated areas, as a result of reduced current, will result in smaller colloidal particles arriving at the surface, better penetration of the pores and hence a more compact coating. This condition is approached by reducing the protective current to the optimum value (consistent with protective potential) for cathodic protection.

The foregoing discussion might be evaluated by considering the properties of the inorganic coatings which were actually formed on specimens Nos. 2 and 3. During the first 24 months of exposure, the coating on No. 2 apparently was superior to that on No. 3, as evidenced by the heavier coating on the former.

TABLE 4. *Mineral analysis of District of Columbia water supply—mg/liter*

Total solids	Loss ign.	SiO_2	Ca	Cl	CO_2	F^-	Fe	HCO_3	Mg	Mn	NO_2	NO_3	SO_4	Alk. $CaCO_3$	Tot. hard $CaCO_3$	N.C.H. $CaCO_3$
157	37	5.9	31.7	10.0	2.1	1.00	.026	78	6.5	0	0	0.73	37.3	64	106	42

It was also observed that the protective current density on No. 3 was several times greater than on No. 2. Current densities were about the same the following year and after 24 months the weight of coating formed on No. 2 was at least 4 times that on No. 3 (25 mg). However, during the period between the 33d and 57th month of exposure the protective current to specimen No. 3 was progressively lowered qy reducing the applied voltage to that value which brought the potential of the specimen to −0.77 v. AEentually the current to No. 3 was smaller than that to No. 2, and the polarization of No. 3 was accomplished at a smaller current density than the polarization of No. 2 (fig. 8).

When the specimens were being cleaned for final reweighing, the coating on No. 3 was observed to be considerably more adherent than that formed on No. 2, even after subjecting the specimens to cathodic cleaning (1 amp/ft^2) for 2 hr. The coating on No. 2 was scraped off rather easily with a brass scraper but that formed on No. 3 had to first be hammered loose by tapping. Unfortunately, no accurate comparison of coating weights can be given, but based on the weight of a portion (500 mg) of the coating removed from No. 3, it was conservatively estimated that the coating formed on No. 3 weighed about 1000 mg and its thickness was about 0.010 in. Thus, the thickness, adherence, and protective value of the coating apparently increased after lowering the protective current to the optimum value as determined by the potential of the specimen.

6. References

[1] Speller, Corrosion, causes and prevention, 500 (McGraw Hill Book Co., Inc., New York, N.Y., 1926).

[2] Evans, Metallic corrosion, passivity and protection, p. 574, (Butler and Tanner, Ltd., London, England, (1937).

[3] K. H. Logan, The protection of pipes against soil action, Trans. Electrochem. Soc. **64,** 137 (1933).

[4] Irving A. Denison, Corrosion of galvanized steel in soils, J. Research NBS **49,** 299 (1952) RP2366; Corrosion **9,** 132 (1953).

[5] T. P. Hoar, private communication, January 1951.

[6] Uhlig, Corrosion Handbook (John Wiley & Sons, Inc., New York, N.Y. 1948); John M. Pearson, Fundamentals of cathodic protection, p. 933.

[7] W. J. Schwerdtfeger, Current and potential relations for the cathodic protection of steel in a high resistivity environment, J. Research NBS **63C,** 37 (July–Sept. 1959); Corrosion **16** (May 1960).

[8] W. J. Schwerdtfeger, and O. N. McDorman, Potential and current requirements for the cathodic protection of steel in soils, J. Research NBS **47,** 104 (1951) RP2233; Corrosion **8,** 391 (1952).

[9] W. J. Schwerdtfeger, Current and potential relations for the cathodic protection of steel in salt water, J Research NBS **60,** 153 (1958) RP2833; Corrosion **14,** 446t (Oct. 1958).

[10] W. J. Schwerdtfeger, and O. N. McDorman, Measurement of the corrosion rate of a metal from its polarizing characteristcs, J. Electrochem. Soc. **99,** 407 (1952).

[11] E. J. Simmons, Use of the Pearson bridge in corrosion inhibitor evaluation, Corrosion **11,** 255t (June 1955).

[12] R. V. Skold, and T. E. Larson, Measurement of the instantaneous corrosion rate by means of polarization data, Corrosion **13,** 139t (Feb. 1957).

[13] Milton Stern, A method for determining corrosion rates from linear polarization data, Corrosion **14,** 440t (Sept. 1958).

(Paper 65C3—68)

JOURNAL OF RESEARCH of the National Bureau of Standards—C. Engineering and Instrumentation
Vol. 65C, No. 3, July–September 1961

Calibration of Inductance Standards in the Maxwell-Wien Bridge Circuit*

Thomas L. Zapf

(February 28, 1961)

This paper discusses the errors from residuals in the Maxwell-Wien bridge and the effect of these on the measurement of inductors in a bridge not having a Wagner ground. Particular attention is given to the use of substitution methods for accurate measurements and especially to the "equal-substitution" (comparison) method, which can yield excellent precision in the calibration of inductance standards.

1. Introduction

Self inductors and mutual inductors can be constructed to have inductance that is computable from their geometry and dimensions. Although the inductance of certain inductors having measurable mechanical dimensions and simple geometrical form can be computed with excellent accuracy, such inductors are not often used as reference standards for inductance measurements. In practice, inductance measurements are more conveniently made with reference to noncomputable reactances in the form of compact and stable reference standards of inductance or capacitance. Accurate values of inductance can be determined by comparing the reactance of the inductor with the reactance of either standard capacitors or standard inductors by use of appropriate bridge circuits. However, the most precise measurement of an unknown quantity (in this case inductance) is made by comparing it with a standard of like kind and magnitude, the small difference being measured by a corresponding small change in one element of the bridge circuit. When comparison methods are used, it is often possible to reduce the detrimental effects of residuals in the measuring circuit to such an extent that the precision of comparison is much better than the accuracy with which the calibration standard is known.

The Maxwell-Wien bridge circuit has long been used for the accurate measurement of inductance. For measurements of best accuracy with any alternating-current bridge circuit, even for comparison measurements, it is necessary to consider the effects of residuals, the ways of reducing these effects, and the handling of corrections to offset the net errors.

2. Maxwell-Wien Bridge

A bridge circuit originally developed by J. C. Maxwell [1] [1] for use with ballistic detectors was adapted by M. Wien [2] for a-c measurements. For many years the circuit has been used widely by standardizing laboratories for measurements of inductance. Figure 1 shows a schematic of a well-shielded Maxwell-Wien bridge with Wagner arms for elimination of errors resulting from current diverted to ground through leakage impedances. The inductance, L, to be measured is placed in series with a resistance, r_L. If the components of the bridge arms shown in figure 1 were pure, the inductance measured when the bridge is balanced would be

$$L=CR_PR_S, \tag{1}$$

and to obtain the balance it is necessary that

$$\frac{R}{R_S}=\frac{R_P}{r_L}. \tag{2}$$

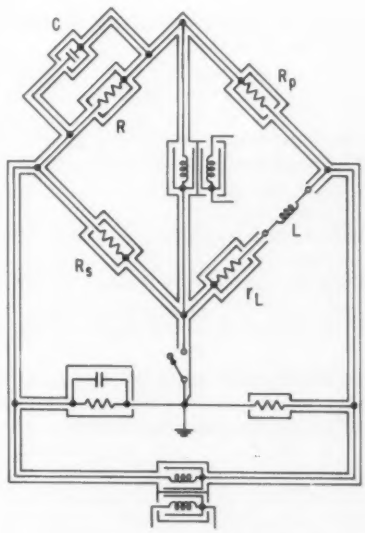

FIGURE 1. *The Maxwell-Wien bridge circuit with complete shielding and a Wagner ground.*

*Contribution from the Radio Standards Laboratory, National Bureau of Standards, Boulder, Colo.

[1] Figures in brackets indicate the literature references at the end of this paper.

In practical situations it is not possible to obtain completely pure components. The residuals in the components contribute to the systematic errors, and it is necessary to analyze the circuit sufficiently to correct for these errors or to determine the maximum uncertainty in the results if the errors are neglected. Figure 2 shows the components of figure 1 with the addition of appropriate residual components, but without the Wagner arms. For example, the series resistor, r_L of figure 1, in the inductance arm is represented in figure 2 by a pure resistance, r_L, in series with an inductance, l_L. The inductance, l_L, is a lumped constant that may be either positive or negative depending upon the relative magnitudes of inductive and capacitive effects. Although lumped constant residuals are not independent of frequency, the lumped constant concept provides a useful equivalent circuit at low frequencies. The other resistive components are similarly represented by a pure resistance and an effective series inductance. The variable capacitance, C, is presumed to contain an effective series resistance, r. The resistance R_L in figure 2 is the equivalent series resistance of the inductor.

3. Equation of Balance

The impedances of the four bridge arms are

$$Z_{RC}=\frac{[(R+j\omega l)(1+\omega^2r^2C^2)}{1+\omega^2r^2C^2+\omega C(\omega rC+j)(R+j\omega l)}, \tag{3}$$

$$Z_P=R_P+j\omega l_P, \tag{4}$$

$$Z_L=R_L+r_L+j\omega(L+l_L), \tag{5}$$

and

$$Z_S=R_S+j\omega l_S. \tag{6}$$

The derivation of eq (3) is given in the appendix. When the bridge is balanced

$$Z_{RC}Z_L=Z_PZ_S. \tag{7}$$

After the multiplication indicated by eq (7) is performed, the equation of imaginary components can be written

$$\begin{aligned}(1+\omega^2r^2C^2)[R(L+l_L)+(R_L+r_L)l-R_Sl_P-R_Pl_S]\\ =C[RR_PR_S+\omega(RR_Pl_S+RR_Sl_P+R_PR_Sl)\omega rC\\ -\omega^2(Rl_Pl_S+R_Pll_S+R_Sll_P)-\omega^3ll_Pl_S\omega rC].\end{aligned} \tag{8}$$

Considerable simplification of eq (8) is possible if the residuals are expressed as time constants and dissipation factors, as follows. Let

$$\omega rC=D_C, \tag{9}$$

$$\frac{l}{R}=\tau_R, \tag{10}$$

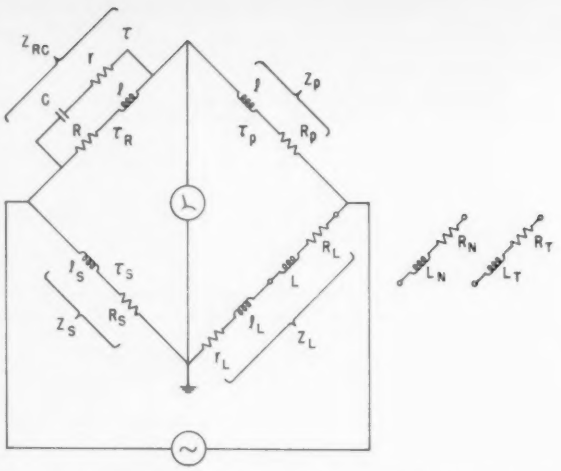

FIGURE 2. *The Maxwell-Wien bridge circuit showing the residuals in the arms as lumped constants.*

$$\frac{l_P}{R_P}=\tau_P, \tag{11}$$

and

$$\frac{l_S}{R_S}=\tau_S. \tag{12}$$

With negligible error it will be found that

$$\begin{aligned}L=CR_PR_S[1-\omega^2(\tau_P\tau_S+\tau_R\tau_P+\tau_R\tau_S)-D_C^2\\ +\omega(\tau_P+\tau_S+\tau_R)D_C-\omega^3\tau_P\tau_S\tau_RD_C]\\ -(R_L+r_L)\tau_R+\frac{R_PR_S}{R}(\tau_P+\tau_S)-l_L,\end{aligned} \tag{13}$$

and a convenient simplification results if the small terms in brackets are replaced by the symbol K. Then the equation of balance becomes

$$L=CR_PR_S(1+K)-(R_L+r_L)\tau_R+\frac{R_PR_S}{R}(\tau_P+\tau_S)-l_L, \tag{14}$$

where

$$\begin{aligned}K=-\omega^2(\tau_P\tau_S+\tau_R\tau_P+\tau_R\tau_S)-D_C^2\\ +\omega(\tau_P+\tau_S+\tau_R)D_C-\omega^3\tau_P\tau_S\tau_RD_C.\end{aligned} \tag{15}$$

4. Effect of Stray Capacitance

Before analyzing this equation in detail it is profitable to consider the effect of stray capacitance across the terminals of the inductor. Such capacitance can be introduced by the leads connecting the inductor to the bridge (see fig. 3). For this analysis, whatever capacitance exists within the case of the inductor is considered not a part of C_S, but rather part of the inductor. It should be understood that this internal shunt capacitance contributes to the

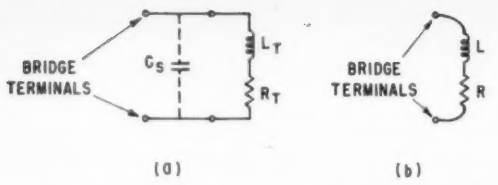

FIGURE 3. *The inductor under test,* L_T, *is connected to bridge terminals with leads having stray capacitance,* C_S, *between them.*

The bridge measures the equivalent inductance, L, which differs from L_T because of the stray capacitance.

effective series inductance measured at the terminals of the inductor, thereby causing the effective series inductance to vary with frequency to some extent.

Figure 3a shows the equivalent series inductance under test, L_T, in series with the internal resistance of the inductor, R_T. The stray capacitance, C_S, external to the inductor is in parallel with L_T and R_T. The bridge measurement does not completely separate these elements but indicates the effective inductance, L, as shown in figure 3b. The effective series inductance, L_T, at the terminals of the inductor is related to the measured value, L, at the ends of the leads by the approximation

$$L_T \approx L\left(1-\omega^2 L_T C_S+\frac{R_T^2 C_S}{L_T}+\omega^2 R_T^2 C_S^2\right). \quad (16)$$

The derivation of eq (16) is given in the appendix. The last three terms in parentheses constitute the small correction terms resulting from stray capacitance. The first and the last of these vary as the square of the frequency. The last term is usually much the smaller of the two in practical situations. The second correction term is not dependent upon frequency and must never be overlooked as a source of error in measurements of the highest accuracy. For example, in the measurement of a 10 h inductor having an internal resistance of 10,000 ohms, at the end of a coaxial cable having a capacitance of 100 pf, the error from neglecting the second correction term is 0.01 h, equivalent to 0.1 percent of the quantity measured. Often the first correction term is significant while the other terms are negligible, and the effective series inductance then can be written

$$L_T \approx L(1-\omega^2 L_T C_S). \quad (17)$$

However, in this paper both the first and second correction terms will be carried in the analysis to follow.

5. Substitution Methods

The existence of the residuals and the consequent correction terms in eqs (14) and (16) are detrimental to good accuracy for residuals are often very difficult to measure or estimate to better than an order of magnitude. To eliminate the effect on measurements of some of these residuals, substitution methods are used. For example, if a standard inductor of equal nominal value is substituted for the test inductor and the difference of inductance is measured by changing C and r_L (or R) slightly, then the residuals in the resistance arms of the bridge have negligible effect on the measurement. Also, the effect of the stray capacitance across the inductor under test or across the standard inductor is much reduced. The standard inductor must be very accurately known, however.

If accurate measurements of large inductors are contemplated and a shorting plug of negligible, or relatively small, inductance is substituted for the test inductor, C_S must be reduced to a negligible value by complete shielding, and a Wagner ground should be used. The effect of the residual, l_L, in the resistor, r_L, is eliminated by this method only if l_L is the same for the two conditions of balance.

The latter method, in which a relatively small inductance replaces the inductor under test, can be designated the "zero-substitution" method to distinguish it from the "equal-substitution" method, in which the test inductor is replaced by a standard of equal nominal inductance.

A general formula for inductance measurements by substitution methods with the Maxwell-Wien bridge may be derived from the two balance equations, the first with the inductor, L_T, in the circuit, and the second with a standard, L_N, in its place. If the small correction terms represented by K in eq (14) are constant for both conditions of balance and if C_S is changed only slightly (to C_{SN}) when the standard inductor or shorting plug is connected, then with certain justifiable approximations

$$L_T = L_N+(C-C_N)R_P R_S[1-\omega^2(L_T+L_N)C_S+K] -\omega^2 L_T L_N(C_S-C_{SN}) +(R_T^2-R_N^2)C_S-(l_L-l_{LN}). \quad (18)$$

The derivation of eq (18) is given in the appendix. This equation is useful in showing the effect of uncertainties in the magnitude of circuit components on the determination of inductance.

If good quality components are used and the bridge is well designed, the time constants that contribute to K will be small. However, K cannot be determined with certainty and is somewhat variable (dependent upon actual circuit constants). The uncertainty in K sets an ultimate practical limit to the accuracy of measurement of inductance by the Maxwell-Wien bridge.

6. Zero-Substitution Method

When the zero-substitution method is employed the small inductance, L_N, need not be accurately known, but the capacitor, C, and the resistance product, $R_P R_S$, must be known with better accuracy than that desired for the inductance, L_T. It is possible to construct very small inductances that are computable from geometry and dimensions. A shorting bar between two terminals has a finite inductance

that can often be calculated or estimated well enough to serve as the "zero-reference", L_N, for bridge measurements of inductors of much larger magnitude. If the measured inductance is defined as the increase in inductance when a shorting-link or switch associated with the inductor is manipulated in a specified manner, then the actual inductance of the short circuit, L_N, is immaterial. The term $(l_L - l_{LN})$ can be minimized if the resistance, r_L, is inductance compensated; i.e., if designed so that the effective series inductance remains constant as the resistance is varied. The uncertainties in this term may limit the accuracy of measurement of small inductors. If C_S is not extremely small, it is evident that the uncertainty in C_S can have a significant effect on the accuracy of measurement by this method. In eq (18) the term in brackets containing C_S can become objectionably large when large values of inductance are being measured. For example, if the inductance being measured is approximately 10 h, if $C_S = 100$ pf ± 10 pf, and if $\omega = 10{,}000$ radians per second, then $\omega^2 L C_S = 0.10 \pm 0.01$. Thus the correction term is 10 percent of the measured inductance, and the measurement uncertainty is 1 percent from this cause alone, disregarding the probable lack of validity of the assumptions (when the correction terms are so large) that were used to derive eq (18). The effect of capacitance C_S thus places a definite limitation on the accuracy which can be obtained by the zero-substitution method with a grounded bridge. In order to obtain better accuracy when $\omega^2 L$ is large it is necessary to use the "equal-substitution method" (described below) or to resort to separate shielding on the inductor leads with an ungrounded bridge using Wagner arms. This latter possibility involves considerations beyond the scope of this paper.

7. Equal-Substitution Method

If an accurately known standard inductance, L_N, is substituted for the test inductor, L_T, the capacitance, C, and the resistance product, $R_P R_S$, need not be so accurately calibrated. Between the two conditions of balance the only circuit components changed are C and r_L, both by small amounts. The residuals D_C and l_L are essentially unchanged in this case, and all the other residuals are identical for both conditions of balance. For the equal-substitution method the general eq (18) can be rewritten with negligible additional error as

$$L_T = L_N + (C - C_N) R_P R_S (1 - 2\omega^2 L_T C_S + K) - \omega^2 L_T^2 (C_S - C_{SN}) + (R_T^2 - R_N^2) C_S - (l_L - l_{LN}). \quad (19)$$

In eqs (18) and (19) the stray capacitances, C_S and C_{SN}, are not considered to be exactly equal; however, it is expected that they will be maintained nearly equal. The importance of this, even in equal-substitution measurements, is evident from eq (19). In the comparison of 10 h inductors at an angular frequency of 10,000 radians per second, if the difference $C_S - C_{SN}$ is only 1 pf, then $\omega^2 L_T^2 (C_S - C_{SN})$ is 0.01 h. This error of 0.1 percent shows the importance of maintaining C_S nearly constant during the substitution.

The term $(l_L - l_{LN})$ can be reduced to a minimum by employing an adjustable resistor, r_L, having inductance compensation. Uncertainties in this term may limit accuracy if the resistances of the test and standard inductors differ greatly, and the inductance compensation of the resistor, r_L, is inadequate. The adjustable resistor is in series with the inductor and is connected to the grounded corner of the bridge as shown in figure 2. If, instead, this resistor were connected to the ungrounded end of the inductance arm of the bridge, the capacitance to ground from the several decades of this resistor would shunt the inductor, and as the resistance is varied to accommodate inductors having different internal resistance the change in stray capacitance would cause an error that would be difficult to correct. If one end of the resistor is grounded, and if care is taken to keep the resistance as low as possible, the capacitance to ground within the resistor merely shunts the resistance, contributing to the effective residual inductance, l_L, which is generally insignificant.

The term $(R_T^2 - R_N^2) C_S$ deserves special attention because it is directly dependent upon the effective series resistances of the inductors. As an example of the effect of this term, consider that, in the measurement of a 10 h inductor, $R_T = 10{,}000$ ohms, $R_N = 8{,}000$ ohms, and $C_S = 100$ pf. Then the term $(R_T^2 - R_N^2) C_S = 0.0036$ h, nearly 0.04 percent of the quantity measured. This correction, being independent of frequency (if skin effect may be neglected) exists even at low frequencies, at which most of the other correction terms are negligible.

If the time constants, τ_P, τ_S, and τ_R, are 1 μsec or less and D_C is 0.001 or less (these are conservative but reasonable estimates for commercially available components), and the angular frequency is 10,000 radians per second, the magnitude of K is less than 0.0003. For a 1 percent difference in inductors, if this term were neglected the resulting error would be only 3 ppm of the measured inductance.

Thus, the equal-substitution method can be employed without the necessity of using a Wagner ground providing care is taken to keep the stray capacitance, C_S, reasonably small and nearly constant and to apply corrections to the measured values to offset errors resulting from the difference in the internal resistances of the inductors.

8. Effect of Frequency Difference

It has been assumed that the frequency of the a-c supply is stable. If the frequency, ω_N, when the standard inductor is in the circuit is not equal to the frequency, ω, when the test inductor is connected, there can be an error resulting from the stray capacitance, C_S. A difference of frequency between the test balance and the standard balance will necessitate the addition of the term

$$-C_S L_T L_N (\omega^2 - \omega_N^2)$$

to the right side of eq (18), and since $\omega \approx \omega_N$ in any practical case, this can be factored to produce

$$-2\omega C_S L_T L_N(\omega - \omega_N).$$

Since $L_T \approx L_N$ for the equal-substitution method, the additional term to be added to eq (19) is

$$-2\omega C_S L_T^2(\omega - \omega_N).$$

If $\omega = 10{,}000$ radians per second, $\omega_N = 10{,}010$ radians per second (a 0.1% difference), and $C_S = 100$ pf, for the measurement of a 10 h inductor by the equal-substitution method the magnitude of the correction term is 0.002 h, an error of 0.02 percent. It is important to realize that this analysis of the effect of frequency variation does not account for the change of effective series inductance with frequency resulting from eddy currents, skin effect, or distributed capacitance within the inductors.

9. Calibration of Inductors

In recent years standard inductors having good stability have become available in a wide range of nominal values. These have made accurate measurements by the equal-substitution method feasible and convenient. Several complete sets of standards are maintained in the laboratories of NBS both at Washington and at Boulder, and are used regularly for calibrating similar standards submitted for certification. The values assigned to NBS working standards ultimately depend upon a computable inductor or capacitor.

The equal-substitution method can be utilized with a variety of a-c bridge circuits. The essential requirements are that the bridge have good short-time stability, adequate resolution, and means for externally equalizing the storage factor (Q) of the inductors being compared. An advantage of the equal-substitution method is the lessened need for accuracy of adjustment of the bridge components because the bridge is used merely to measure small differences. A number of commercially available bridges embody the Maxwell-Wien bridge circuit to which the analysis given in this paper is primarily devoted. It is almost invariably necessary, however, to improve their resolution by adding a calibrated variable capacitor in parallel with those built into the bridge.

The resistor, r_L, is partially inductance compensated and is connected in series with the cable connecting the inductors to the bridge. It has been determined that the existing variations of inductance are negligible relative to the inductance being measured by this method. This resistor may be regarded as serving the purpose of externally equalizing the Q of the standard and test inductors.

It is seldom necessary to apply a correction for the term $(R_T^2 - R_N^2)C_S$ in eq (19). On rare occasions when this term is significant, a crude measurement of R_T and R_N is adequate.

The resistance product (range) in the bridge is set so that the difference between the test and the standard inductors can be accommodated by adjustment of the externally connected variable capacitor and resistor, the other bridge controls being left unchanged.

The analysis of errors in the Maxwell-Wien bridge circuit described in this paper was carried out as part of the investigation of the feasibility of adopting the equal-substitution method for the rapid and convenient measurement of inductance.

The use of the equal-substitution method for the precise comparison of inductors at the Electronic Calibration Center, NBS, Boulder, Colo., was instigated by Chester Peterson, NBS, Washington, D.C. The author is indebted to Mr. Peterson for helpful comments and suggestions pertaining to this paper.

10. Appendix: Derivation of Equations

Equation (3) is derived from the equation of the impedance of Z_C and Z_R in parallel.

$$\frac{1}{Z_{RC}} = \frac{1}{R+j\omega l} + \frac{\omega C}{\omega r C - j}$$

$$= \frac{1}{R+j\omega l} + \frac{\omega C(\omega r C + j)}{\omega^2 r^2 C^2 + 1}$$

$$= \frac{1+\omega^2 r^2 C^2 + \omega C(\omega r C + j)(R+j\omega l)}{(R+j\omega l)(1+\omega^2 r^2 C^2)}.$$

Therefore

$$Z_{RC} = \frac{(R+j\omega l)(1+\omega^2 r^2 C^2)}{1+\omega^2 r^2 C^2 + \omega C(\omega r C + j)(R+j\omega l)}.$$

Equation (8) is obtained by substituting eqs (3), (4), (5), and (6) into eq (7), giving

$$(1+\omega^2 r^2 C^2)(R+j\omega l)[(R_L+r_L)+j\omega(L+l_L)]$$
$$= [1+\omega^2 r^2 C^2 + \omega C(\omega r C + j)(R+j\omega l)]$$
$$(R_P+j\omega l_P)(R_S+j\omega l_S),$$

from which the equation of imaginary components is

$$(1+\omega^2 r^2 C^2)[R(L+l_L)+(R_L+r_L)l - R_S l_P - R_P l_S]$$
$$= C[RR_P R_S + \omega(RR_P l_S + RR_S l_P + R_P R_S l)\omega r C$$
$$-\omega^2(Rl_P l_S + R_P l l_S + R_S l l_P) - \omega^3 l l_P l_S \omega r C].$$

Equation (16) describes the effect of stray capacitance. Figure 3a represents an inductor, L_T, having an internal resistance, R_T, connected to the bridge terminals by a cable having shunt capacitance, C_S.

The impedance of this circuit, Z, is derived as follows

$$\frac{1}{Z}=\frac{1}{R_T+j\omega L_T}+j\omega C_S,$$

$$Z=\frac{(R_T+j\omega L_T)(1-\omega^2 L_T C_S-j\omega R_T C_S)}{(1-\omega^2 L_T C_S+j\omega R_T C_S)(1-\omega^2 L_T C_S-j\omega R_T C_S)},$$

$$Z=\frac{R_T+j\omega[L_T(1-\omega^2 L_T C_S)-R_T^2 C_S]}{(1-\omega^2 L_T C_S)^2+\omega^2 R_T^2 C_S^2}.$$

In the equivalent circuit shown in figure 3b

$$Z=R+j\omega L,$$

and from the two preceding equations it is evident that

$$L=\frac{L_T(1-\omega^2 L_T C_S)-R_T^2 C_S}{(1-\omega^2 L_T C_S)^2+\omega^2 R_T^2 C_S^2}$$

and, with negligible error,

$$L=\frac{L_T\left(1-\omega^2 L_T C_S-\dfrac{R_T^2 C_S}{L_T}\right)}{(1-2\omega^2 L_T C_S+\omega^2 R_T^2 C_S^2)}.$$

It should be noted that the discarded term, $\omega^4 L_T^2 C_S^2$, in the denominator is always much smaller than the term, $2\omega^2 L_T C_S$, which is usually much smaller than 1 in practical inductance measurements at low audiofrequencies. Since the terms in parentheses, other than 1, are small, this equation can be solved for L_T and simplified by neglecting higher order terms.

$$L_T\approx L\left(1-\omega^2 L_T C_S+\frac{R_T^2 C_S}{L_T}+\omega^2 R_T^2 C_S^2\right).$$

Equation (18) is obtained from the following two equations which are derived from eq (14) modified according to eq (16)

$$L_T=CR_P R_S\left(1-\omega^2 L_T C_S+\frac{R_T^2 C_S}{L_T}\right)(1+K)$$
$$-(R_L+r_L)\tau_R+\frac{R_P R_S}{R}(\tau_P+\tau_S)-l_L$$

and

$$L_N=C_N R_P R_S\left(1-\omega^2 L_N C_{SN}+\frac{R_N^2 C_{SN}}{L_N}\right)(1+K)$$
$$-(R_{LN}+r_{LN})\tau_R+\frac{R_P R_S}{R}(\tau_P+\tau_S)-l_{LN}.$$

In eq (15) it will be noted that at the higher frequencies the first term in K is the largest term, and that at lower frequencies all terms in K are small and often negligible. The first term in K is independent of D_C, which may vary slightly between the two conditions of balance; hence, the assumption that K is constant is justifiable. In the above equations since

$$CR_P R_S\approx L_T$$

and

$$C_N R_P R_S\approx L_N$$

and

$$(R_L+r_L)\approx(R_{LN}+r_{LN})$$

$CR_P R_S R_T^2 C_S/L_T\approx R_T^2 C_S$ and

$$C_N R_P R_S R_N^2 C_{SN}/L_N\approx R_N^2 C_{SN}.$$

Therefore,

$$L_T-L_N=[(C-C_N)R_P R_S-R_P R_S\omega^2(CL_T C_S$$
$$-C_N L_N C_{SN})+R_T^2 C_S-R_N^2 C_{SN}](1+K)-(l_L-l_{LN}).$$

The factor $(CL_T C_S-C_N L_N C_{SN})$ can be expanded as follows:

$$(CL_T C_S-C_N L_N C_{SN})=(C-C_N)(L_T C_S+L_N C_{SN})$$
$$+C_N L_T C_S-CL_N C_{SN}.$$

If C_S and C_{SN} can be reduced to zero, this factor becomes zero, and the equation is greatly simplified. However, if C_S is not zero, but if C_S approximately equals C_{SN},

$$CL_T C_S-C_N L_N C_{SN}=(C-C_N)(L_T+L_N)C_S$$
$$+C_N L_T C_S-CL_N C_{SN}$$

and

$$L_T-L_N=\{(C-C_N)R_P R_S[1-\omega^2(L_T+L_N)C_S]$$
$$-R_P R_S\omega^2(C_N L_T C_S-CL_N C_{SN})$$
$$+(R_T^2-R_N^2)C_S\}(1+K)-(l_L-l_{LN}),$$

and with negligible error the substitution $C_N R_P R_S=L_N$ and $CR_P R_S=L_T$ can be made in the small correction terms. The second term in braces can be reduced to $-\omega^2 L_T L_N(C_S-C_{SN})$. If the terms under consideration are not relatively small, the approximations are not valid.

Neglecting second order terms, the above equation can be simplified, giving eq (18):

$$L_T=L_N+(C-C_N)R_P R_S[1-\omega^2(L_T+L_N)C_S+K]$$
$$-\omega^2 L_T L_N(C_S-C_{SN})+(R_T^2-R_N^2)C_S-(l_L-l_{LN}).$$

11. References

[1] J. C. Maxwell, A treatise on electricity and magnetism, 1st ed., **2**, 377–379 (1873), or 3d ed., Art. 778.
[2] Max Wien, Ann. der Phys., **44**, 689–712 (1891).
[3] H. L. Curtis, Electrical Measurements, 113–117, McGraw-Hill Book Co., Inc., New York, N.Y. (1937).

(Paper 65C3–69)

JOURNAL OF RESEARCH of the National Bureau of Standards—C. Engineering and Instrumentation
Vol. 65, No. 3, July–September 1961

Calibration of Loop Antennas at VLF[1]

A. G. Jean, H. E. Taggart, and J. R. Wait

(February 21, 1961)

A technique and the equipment used for the precise determination of field strength of signals received from VLF transmitters is described. The equipment, which is battery-operated, contains provisions for the reception of VLF signals and the generation of standard fields to an accuracy of 5 percent. Both the receiving and transmitting antennas are loops. The field strength is determined in terms of a quasi-static magnetic field with the two loop antennas positioned coaxially at a spacing of approximately two meters. Although the technique was developed for use at VLF, it can be used at higher frequencies for calibrating loop antennas, generators, and voltmeters, and for determining effective heights of antennas, or similar applications.

1. Introduction

With the increased use of the very low frequency portion of the radio spectrum, an urgent need exists for the accurate calibration of receiving antennas operating in this frequency range. Conventional methods of calibrating loop antennas require that they be placed in a radiation field. In other words, the separation between the test source and the receiving antenna is large compared to the wavelength. At VLF this requirement becomes impractical; for example, the wavelength at 10 kc/s is 30 km. A test source placed at distances greater than this may require several kilowatts of power to provide a signal that will compete with the atmospheric noise level.

It is suggested by Greene [1951] that a free space radiation field could be simulated adequately at the receiving antenna if the test source were also a loop antenna and placed coaxially with, and close to, the receiving loop antenna which is to be calibrated. The magnitude of the equivalent radiation field at the receiving loop antenna is then calculated in terms of the geometry and configuration of the two loops. Such an equation has been stated by Greene [1951] without proof.

It is the purpose of this paper to investigate the general applicability of Greene's equation, to outline a technique used for the precise and accurate determination of field strength using this equation, and finally to describe the equipment used to perform these measurements.

2. Theoretical Basis

The necessary equations for calibrating a loop receiving antenna with a coaxial test transmitting loop are first considered. The distance of separation is arbitrary, and the dimensions of the loops are assumed small compared to the wavelength. The situation is illustrated in figure 1.

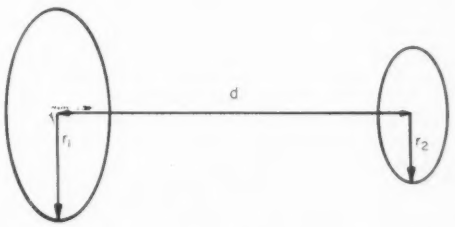

FIGURE 1. *Simplified view of two coaxial loops.*

The actual value of the voltage v induced in the receiving loop may be expressed in terms of the maximum equivalent electric field, E_f, that would exist in a free-space radiation field. The relationship for an electrically small loop is simply

$$v=j\beta\pi r_2^2 E_f, \qquad \text{where } \beta=\frac{2\pi}{\lambda}, \tag{1}$$

but $v=IZ_m$, where Z_m is the mutual impedance between the loops. Where all dimensions are electrically small and currents in the loop are constant, we have exactly

$$Z_m=(2\pi r_2)\frac{j\mu\omega}{\pi k}\left(\frac{r_1}{r_2}\right)^{\frac{1}{2}}\left[\left(1-\frac{k^2}{2}\right)K(k)-E(k)\right] \tag{2}$$

$$=j\mu\omega\frac{\pi r_2}{16}\left(\frac{r_1}{r_2}\right)^{\frac{1}{2}}\times k^3\left(1+\frac{3}{4}k^2+\frac{75}{128}k^4+\ldots\right), \tag{3}$$

where $k=\left[\frac{4r_1r_2}{(r_1+r_2)^2+d^2}\right]^{\frac{1}{2}}$ and r_1 and r_2 are the transmitting and receiving loop radii, respectively, and d is their center-to-center separation. $K(k)$ and $E(k)$ are elliptic integrals as tabulated by Dwight [1947]. The above equation for Z_m may be obtained from a number of different sources, including Smythe [1950] who gives a formula for the ϕ-component of the

[1] Contribution from Central Radio Propagation Laboratory and Radio Standards Laboratory, National Bureau of Standards, Boulder, Colo.

vector potential, A_ϕ, of a loop carrying a constant current I. The mutual impedance Z_m is then calculated by integrating $E_\phi = -j\omega A_\phi$ around the receiving loop. The length of this path is $2\pi r_2$.

Thus,

$$E_f \cong \frac{60\pi r^2 I}{[d^2+(r_1+r_2)^2]^{3/2}} \times \left[1+\frac{3}{4}k^2+\frac{75}{128}k^4+\ldots\right]. \quad (4)$$

Neglecting terms in the series above k^2, it is seen that this expression can be reduced as follows

$$\frac{1+\frac{3}{4}k^2}{[d^2+(r_1+r_2)^2]^{3/2}} \cong \frac{1+3\frac{r_1r_2}{d^2}+\text{terms in}\left(\frac{r_1r_2}{d^2}\right)^2}{[d^2+r_1^2+r_2^2+2r_1r_2]^{3/2}}$$

$$\cong \frac{1}{[d^2+r_1^2+r_2^2]^{3/2}} \times \left[1+\text{terms in}\left(\frac{r_1r_2}{d^2}\right)^2\right]. \quad (5)$$

The last expression is the denominator in Greene's equation [1951]. If both loops have radii comparable to d, the quantity k is not small compared to unity, and higher terms must be retained in the series. At higher frequencies where d/λ cannot be neglected compared to unity, a correction factor may be applied which is the ratio of the coaxial magnetic field of a small loop at wavelength λ to the infinite wavelength case. This is known to be $1+j2\pi d/\lambda$ and has a magnitude

$$\left[1+\left(\frac{2\pi d}{\lambda}\right)^2\right]^{\frac{1}{2}},$$

as stated by Greene [1951]. It is strictly valid for $d>>r_1$, but it is only a minor second order correction at medium frequencies and is completely negligible at VLF.

Equation (4) is valid for determining the equivalent free-space electric field strength if r_1, r_2, and d are electrically small compared to λ. Since this equation is strictly valid only in free-space, the effects of neighboring objects have been verified experimentally by moving metallic objects of various sizes near the loop antennas and observing the effects on the system. If the nearest sizable objects are separated from the loops by approximately two to three times the loop spacing, d, the resulting error will be less than about 1 percent. The measurements should not be performed in a shielded room, and the measurement site should be free of large metallic objects such as overhead power lines or similar objects.

3. Calibration Procedure

Two basic methods are applicable to the measurement of field intensity [IRE Standards, 1942]; one is the standard-antenna method, and the other is the standard-field method. In the former a standard receiving antenna is used so that the voltage produced in it by a field of given intensity and polarization may be computed. The usual voltage measured is not the open-circuit antenna voltage but is related to it through a voltage transfer ratio. It is sometimes difficult to determine this voltage transfer ratio to a high degree of accuracy.

In the standard-field method, a standard field is set up by a local transmitting arrangement, and the field at the receiving antenna is computed from the dimensions of the receiving and transmitting antennas, the separation distance between the antennas, and the current in the transmitting loop. In this technique the equipment consists of a suitable receiver equipped with a meter to indicate the relative strength of the received field. The strength of the received field is determined by comparing the receiver output voltage produced by the field under measurement with the voltage produced by a standard field.

Each of the basic methods offers certain advantages and disadvantages dependent upon the application. In the case under consideration, the standard-field method was adopted because of the straightforward calibration method which can be evolved using coaxial loop antenna arrangements as discussed above.

The calibration equipment is represented in figure 2; that to the left is used to receive and indicate the relative amplitudes of fields, while that to the right is used to produce VLF fields of appropriate frequency and amplitude. In calibrating, the deflection of the receiver output meter in response to the unknown VLF field is obtained with the receiving loop in the plane of propagation. The receiving loop is then rotated 90° to minimize the receiver response to this field. The transmitting loop is positioned coaxially with the receiving antenna at a separation distance of 1 or 2 m. Without changing the receiver tuning or sensitivity, the frequency and output of the signal generator are adjusted to reproduce the same receiver output meter indication that was obtained in response to the unknown VLF field. The equivalent value of the radiation field incident at the receiving antenna is calculated from eq (4) above in terms of the antenna radii, their separation distance, and the RF current in the transmitting antenna. The strength of the unknown field is equal to the equivalent radiation component of the locally generated field.

In figure 2, the "Metering Equipment" block is symbolic of the method used to determine the RF current in the transmitting loop. The technique is represented in detail in figure 3. Balanced RF voltages, obtained from the RF signal generator and Balun (balanced-to-unbalanced transformer), are

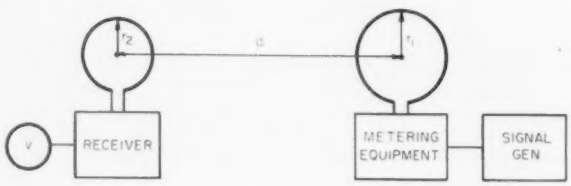

FIGURE 2. *Block diagram of the loop antenna calibration system.*

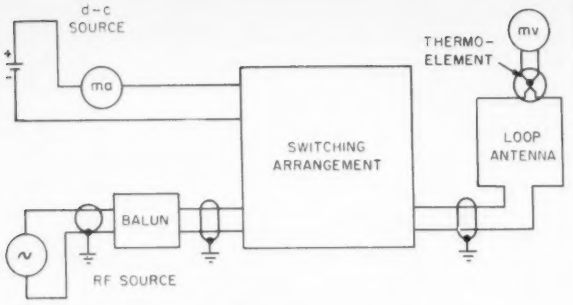

FIGURE 3. *Calibration of the transmitting loop antenna.*

connected to the single-turn unshielded transmitting loop. A vacuum thermoelement is mounted in the top-center of the transmitting loop as indicated. The RF current introduced into the loop flows through the thermocouple heater element. The d-c output voltage of the thermoelement is indicated by the d-c millivoltmeter. The RF current is then disconnected from the loop antenna and replaced by a direct current. The direct current is adjusted to produce the same thermoelement d-c output voltage that was attained in response to the RF current. Since equal values of rms RF current and direct current produce equal thermoelement output voltages, the value of direct current read from the milliammeter, figure 3, is used in eq (4) in calculating the field strength at the receiving loop antenna.

An RF micropotentiometer [2] [Selby, 1953] was incorporated into the calibration equipment to provide an accurate source of RF voltages. The arrangement used for calibrating the micropotentiometer and establishing known RF voltages is shown in figure 4. The thermoelement of the micropotentiometer is the same type used in the transmitting loop. The switching arrangement indicated permits either RF or direct current to flow through the thermoelement and the micropotentiometer resistor element. To establish an accurately known RF voltage across the micropotentiometer, the current required to produce the desired voltage is calculated. A direct current of this magnitude (as indicated by the milliammeter) is caused to flow through the thermocouple and resistor element of the micropotentiometer. The d-c output of the thermoelement in response to the direct current is observed. An RF current of appropriate frequency is then substituted for the direct current and adjusted in magnitude to produce the same thermoelement output voltage that was obtained in response to the direct current. The required RF voltage then exists across the resistive element of the micropotentiometer. The micropotentiometer, having an internal impedance of a few milliohms, is usually used to calibrate equipment having input impedances ranging from 50 ohms upwards. In such cases, the standard voltage across the micropotentiometer is not significantly altered when the equipment under calibration is connected.

[2] This is simply a low-impedance source of RF voltage adjustable from 1 to $10^5 \mu v$

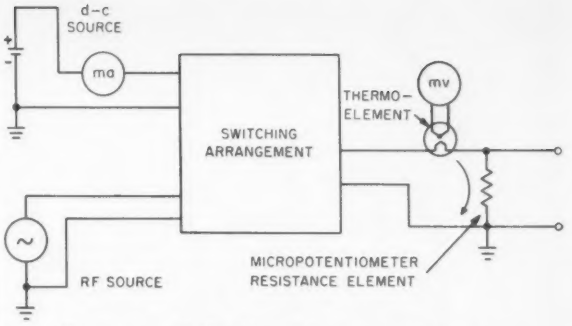

FIGURE 4. *Calibration of the micropotentiometer.*

4. Description of Equipment

A photograph of the prototype of the field intensity and calibration equipment is given in figure 5. As viewed from left to right, the individual items are: The receiving loop antenna shown connected by a cable to a box containing a balanced-to-unbalanced electrostatically shielded transformer. The third unit from the left is a transistorized VLF receiver. The next item is a commercially made transistorized VLF signal generator. The transmitting loop antenna is shown mounted on a supporting pedestal with the input terminals near the bottom and the thermoelement and its output at the top. The small box in front and to the right of the transmitting loop contains a transistorized final amplifier for the signal generator. The large box at the extreme right is the calibration unit containing the laboratory type d-c milliammeter and d-c millivoltmeter, the micropotentiometer, switching circuits, etc. A photograph of a collapsible frame to support the transmitting loop antenna (to the left) and the receiving antenna (to the right) is shown in figure 6. The spacing between the loop antennas in this photograph is 2 m. The framework is made of short sections of tubing which may be disassembled into a "bundle of sticks" for easy transport.

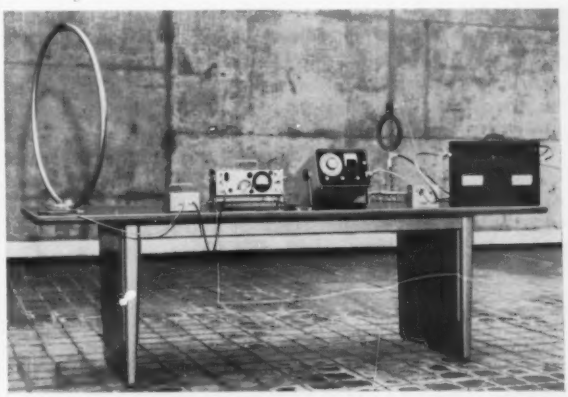

FIGURE 5. *Field intensity and calibration equipment.*

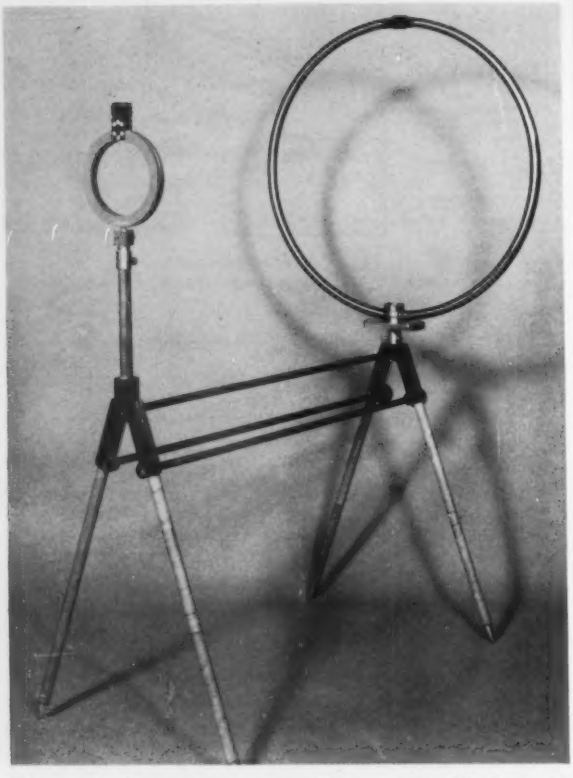

FIGURE 6. *Loop antennas mounted on a collapsible frame for field use.*

Although all of the equipment shown is battery-operated and has been used in field work, no serious effort was made to minimize the size or weight of this prototype equipment. Obvious improvements could be made, such as reducing the diameter of the receiving loop and the input transformer, positioning the final amplifier within the signal generator, miniaturizing the calibration unit, etc.

The receiving loop antenna is electrostatically shielded and balanced with respect to ground. The input transformer is a balanced-to-unbalanced unit with an electrostatic shield betweeen the primary and secondary windings. A high degree of balance was achieved in the loop input circuit to minimize undesirable unbalanced currents.

The transistorized, battery-operated VLF receiver shown in the photograph is an early model developed at NBS. An improved model has since been developed which has a sensitivity of about 100 μv/m and a bandwidth adjustable from 40 to 400 c/s. The receiver is tunable from 14.5 kc/s to 22 kc/s and is provided with a voltmeter to indicate the relative amplitude of received signals. In the experiment cited, voltmeter readings were made during intervals when station NLK was transmitting a steady carrier signal. It is intended to describe this receiver in a future publication.

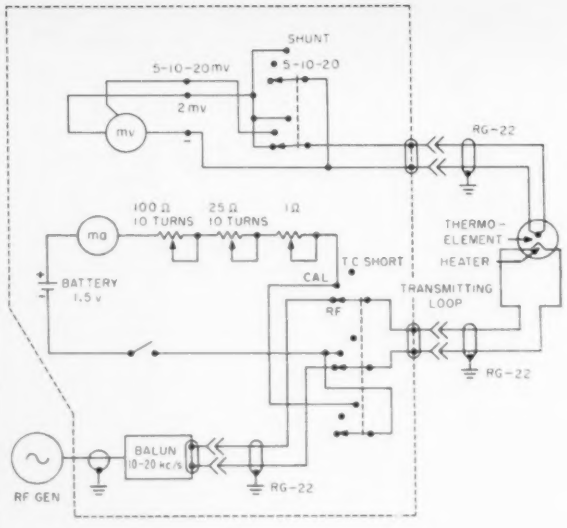

FIGURE 7. *Schematic of calibration unit.*

A schematic diagram of the calibration unit is shown in figure 7. The apparatus for the generation of standard fields (represented in fig. 3) and for the calibration of the micropotentiometer (represented in fig. 4) are combined in this unit. The d-c milliammeter and millivoltmeter are high quality laboratory instruments with accuracies of 0.5 percent. Thermoelements of 5- to 100-ma capacity were used in the micropotentiometers, which enabled standard voltages to be generated within a range of 100 to 50,000 μv with an accuracy of better than 3 percent. This type of thermoelement when calibrated with direct current can be used as a current-measuring device up to 300 Mc/s to an accuracy within 1 percent.

The transmitting loop consists of a single-turn unshielded loop with a 100 ma thermoelement mounted in the top-center. The balun transformer has a voltage unblance that is less than 2 percent of the balanced output voltage, and an insertion loss that is less than 0.3 db. This system can be used to establish standard fields with excellent precision and an accuracy that is better than 5 percent.

The transmitting and receiving loop antennas, with radii of approximately 0.1 and 0.35 m, respectively, were spaced 2.0 m from each other. Under these conditions the bracketed series in eq (4) yields a correction factor of approximately 1.028. This represents an increase of approximately 3 percent over the value of the field if the correction is neglected.

The equipment described in this paper was designed to measure field strengths in the range from 230 to 23,000 μv/m at frequencies between 15 and 20 kc/s. The range of frequency coverage can be extended by proper selection of the balun transformer, the signal generator, and the receiver. The micropotentiometer can be used over a voltage range of 1 μv to 200 mv at frequencies up to 300 Mc/s.

The ranges of operation of this equipment can be extended in frequency and amplitude for use in other applications. Excellent precision is obtained with this system with an accuracy not before attainable. All calibrations are performed with direct current. This eliminates many sources of error, and the d-c measuring instruments can readily be checked against reliable d-c working standards. This unit was recalibrated after an extensive field trip, and the calibration of the instruments did not vary more than 0.2 percent.

5. References

Dwight, H. B., Tables of integrals and other mathematical data, Revised edition (MacMillan Co., New York, N.Y., 1947).

Greene, F. M., Calibration of commercial field strength meters at the National Bureau of Standards, NBS Circ. 517 (Dec. 1951).

IRE Standards on radio-wave propagation, Measuring Methods (1942).

Selby, M. C., R. F. Micropotentiometers, Radio-Electronic Engineering (Oct. 1953).

Smythe, W. R., Static and dynamic electricity (McGraw-Hill Book Co., Inc., New York, N.Y., 1950).

(Paper 65C3–70)

JOURNAL OF RESEARCH of the National Bureau of Standards—C. Engineering and Instrumentation
Vol. 65C, No. 3, July–September 1961

Location of the Plane of Best Average Definition With Low Contrast Resolution Patterns

Francis E. Washer and William P. Tayman

(April 28, 1961)

The plane of best average definition is located for each of several airplane-camera lenses using two types of low contrast test pattern and two emulsions. A low contrast pattern composed of dark lines on a light background and the reverse pattern consisting of light lines on a dark background are used. The results of measurement indicate that the position of the plane of best focus and the numerical magnitudes of the root mean product mean $\sqrt{R_s T_s}$ value of the resolving power are not significantly affected by this reversal of contrast In addition, the results obtained using low contrast targets are compared with those obtained with high contrast targets. Hence the position of the selected focal plane remains invariant although the values of the measured resolving power are substantially higher for the high contrast targets.

1. Introduction

In specifications dealing with airplane mapping cameras, great emphasis is placed upon the photographic resolving power of the lenses used in the camera. The method of measurement to be used in evaluating the resolving power is usually described in careful terms, with the type of test chart, the characteristics of the registering emulsion, the physical conditions of test, and the manner of reporting results all given in detail. A 1950 military specification, MIL–STD–150 [1] [1] attempted to establish standard practices in the evaluation of lens performance. A recent revision of this comprehensive specification, MIL–STD–150A [2] was issued in 1959. At the Washington meeting of the International Society of Photogrammetry in 1952, a specification dealing with the calibration of photogrammetric cameras was adopted for trial and discussion [3].

At the time the International Specification for the calibration of photogrammetric cameras was drawn, it was not possible to standardize on a single type of resolving power chart. Consequently several were listed as suitable for use; these include the three-line chart used by the U.S. Air Force [2], the Cobb two-line chart used in Great Britain and the annulus chart used in Canada [4]. These charts were of low contrast except that the three-line chart of the Air Force was provided in both high and low contrast versions. The three-line chart of the National Bureau of Standards [5] was not included as it has been available for only a few months prior to the drawing of the specification and its properties were not widely known.

In the eight years that have passed since the adoption of this specification, agreement on a single test chart has not yet developed. A few publications have appeared [6, 7] that permit an estimate of the differences likely to be found in comparing various types of charts.

Because of the differences that exist among the various test charts used in various laboratories, a study was initiated at the National Bureau of Standards in which the values of resolving power for the same group of lenses were determined for a variety of test charts, target contrasts, and emulsions. The results of this study should be useful in estimating the probable values of resolving power that would be obtained for a lens with a given type of chart when results are available for the same lens with a different type of chart.

This is the concluding portion of a three part investigation. The results for the first part dealing with various indices and methods used in locating the plane of best average definition have been reported in Photogrammetric Engineering [8]; the results for the second part which comprises results for lone-line, short-line, and annular charts are reported in J. Research NBS [9]. The results of the third part which deals with variations arising from differences in target contrast for two emulsions are reported in the present paper.

Measurements of photographic resolving power at the National Bureau of Standards are customarily made using a long-line three line high contrast test chart having dark lines on a light background with the images registered on a high contrast emulsion which has a higher resolving power than the emulsion commonly used in aerial photography. In many other calibration laboratories, the tendency is to use test charts having light lines on a dark background

[1] Figures in brackets indicate the literature references at the end of this paper.

with the images registered on a medium contrast emulsion with resolving power comparable to that being currently used in aerial photography.

In the present study, values are obtained for two emulsions and three targets of differing contrast. Results are given for four lenses of types commonly used in photogrammetric cameras.

2. Method of Measurement

2.1. Test Camera

The National Bureau of Standards precision lens testing camera [10] was used in making the negatives from which the values of resolving power are determined. Its construction and mode of operation simplify the process of evaluating the resolving power of a lens in a series of focal planes spaced at definite intervals along the optical axis. The precision lens testing camera is equipped with 10 collimators spaced at 5° intervals and spanning the range from 0° to 45°. Resolving power test charts placed in the focal plane of the collimators and imaged by the lens under test permit the study of quality of imagery for a series of focal planes of the test lens. By using one type of chart in 5 of the 10 collimators (designated the odd-numbered collimators) spaced at 10° intervals and another type in the remaining five collimators (designated the even-numbered collimators) it is possible by proper manipulation of the various controls to record the imagery of a lens under test on a single photographic plate for each of two types of chart in the same series of focal planes for the same angular separations, β, from the axis of the lens under test.

2.2. Test Charts

Three types of test chart are used in the present investigation. All three are based upon the NBS resolution chart of 1952 but differ in contrast between the lines and spaces. Each chart has the same range of sizes of the test object with the size proceeding in a geometric progression with $\sqrt[4]{2}$ (or 1.1892) as the common ratio. The same size test chart is used in the various collimators so that it is necessary to apply the "cos" and "cos^2" corrections to images formed off-axis. The various types are described in the following section.

a. High Contrast Test Chart (HDL)

This is a composite chart based upon the NBS resolution test chart of 1952 which is described in detail in NBS Circular 533 [5]. It is a long-line three line chart with dark lines on a light background. The difference of log luminance between the dark lines and the light background exceeds 2.0.

b. Low Contrast Test Chart (LDL)

This chart is identical in all respects to that described in (a) except that the contrast is low between the dark lines and the light background. The difference of log luminance between the dark lines and the light background is 0.20 $\pm$0.02.

c. Low Contrast Test Chart (LLD)

This chart is identical to that described in (b) except that the contrast is reversed, that is, the difference in log luminance between the light lines and the dark background is 0.20 $\pm$0.02.

2.3. Test Negative

In making the test negative, the lens under test is initially so alined that its optical axis is parallel to and approximately coincident with the axis of the collimated beam emergent from the first collimator. The lens is adjusted along the bench to a location such that the collimated beam at 40° from the axis fills the front aperture of the lens under test as viewed through the lens at an inclination of 40° from the axis. The plate holder is adjusted to a position such that the front surface of the emulsion is in the plane of best visual axial focus for the central row of images to be registered on the plate. The plate holder is then moved to a position 1.05 mm nearer to the lens, where an exposure is made by illuminating the reticles in odd-numbered collimators, which thus records the imagery on the plate at 10° intervals for the range of angles from β=0° to β=40°. This process is repeated with the plate moved 0.15 mm farther from the lens until 15 exposures have been made with the last for the plane 1.05 mm farther from the lens than the position of best visual axial focus. Between each exposure, the plate holder is also moved downward by an amount sufficient to avoid superposition of successive rows of images. The foregoing operation registers the imagery for the long-line high contrast patterns on the plate. The plate holder is then returned to its initial position for which the emulsion surface is 1.05 mm nearer to the lens than the plane of best visual axial focus; the plate is displaced sidewise in its holder approximately 12 mm; and the entire bench on which the camera is mounted is rotated on its pivot by 5° so that the axis of the lens is now parallel to and nearly coincident with the axis of the collimated beam emergent from the second collimator. The foregoing procedure is then repeated with the exception that exposures are made by illuminating the reticles in the even-numbered collimators, which again registers imagery on the plate at 10° intervals for the range of angles from β=0° to β=40°. This process registers the imagery for the long-line low contrast patterns on the plate. The exposed plate is then processed to form the finished negative from which values of resolving power for tangential lines (T_β) and radial lines (R_β) are determined.

All exposures are made with the reticles illuminated by light from tungsten lamps with Wratten K–3 filters between the light source and test charts. Neutral filters are used to adjust the intensity of the light reaching the plate so that the final resulting optical density of each image on the negative is approximately the same for all values of β. The two types of photographic plates used in this work were Eastman Spectroscopic VF which has a fine grained panchromatic emulsion and Eastman Super Panchro Press, Type C. The plates were developed for 3 min. in D–19 developer at 68 °F.

2.4. Reading the Negative

The negative images were examined with a microscope using powers ranging from 30 to 50×. The criteria for considering a particular line pattern to be the finest resolved were that all coarser patterns were resolved and that the number of lines in a given pattern was the same as that of the corresponding pattern in the object.

3. Results of Measurements

The results of measurement on four wide-angle lenses are reported and analyzed in this study. Two lenses, designated Nos. 1 and 5, are essentially distortion-free; the other two, designated 7 and 8, have moderate amounts of distortion. Measurements of resolving power were made at 10° intervals from 0° to 40°.

Negatives were made with both VF and SP emulsions for each of three target contrasts for each of the four lenses. The measured equivalent focal length for the plane of best visual axial focus was the same for each emulsion and each type of target pattern. The maximum range of change in measured equivalent focal length did not exceed ± 0.02 mm for a given type of lens.

The results of measurement are shown graphically in figures 1 and 2. The values of the geometric mean resolving power $\sqrt{R_\beta T_\beta}$ are shown plotted against the separation, Δf, from the plane of best visual axial focus. Positive values of Δf denote positions of the image plane farther from the lens than the plane of best visual axial focus. In figure 1, values of $\sqrt{R_\beta T_\beta}$ obtained with VF emulsion are shown for values of β ranging from 0° to 40°. The lowest frame in each column shows values of the root mean product mean [8] $\sqrt{\overline{R_\beta T_\beta}}$ versus Δf. The curves, numbered 1, show the results obtained with the high contrast target having dark lines on a light background. The curves, marked 2, show the results for the low contrast target having dark lines on a light background. The curves, marked 3, show results for the low contrast targets having light lines on a dark background. In figure 2, comparable results are shown for the same four lenses using SP emulsion.

Values of $\sqrt{R_\beta T_\beta}$ are shown in these graphs as this quantity is of primary interest in evaluating the image forming qualities of a lens intended for use in an airplane mapping camera. In two earlier papers [8, 9], values of R_β and T_β are shown for lens No. 1.

4. Location of the Plane of Best Average Definition

The plane of best average definition was located for each set of conditions by the maximum value of the index $\sqrt{\overline{R_\beta T_\beta}}$. The plane so located is likely to be slightly farther from the lens than that located by graphical analysis [8]. For the purposes of the present paper, the use of the maximum of $\sqrt{\overline{R_\beta T_\beta}}$ is satisfactory. The values of the index $\sqrt{\overline{R_\beta T_\beta}}$ for the range of Δf extending from 0.45 mm nearer to the lens to 0.30 mm farther from the lens than the plane of best visual axial definition is shown in table 1 for the four lenses for all of the various conditions. The values listed are the averages for several runs ranging from 1 to 6. The total number of runs for the high contrast target is equal to the sum of the runs for the two low contrast targets. This occurs because a single negative always contains a record of the imagery for the high contrast target and for one of the two low contrast targets. In table 1 the underlined value of the index in each column is the maximum for the indicated set of conditions.

5. Comparison of Results Obtained With the Three Charts

The principal points to be considered in the analysis of the results of measurement are possible differences in the location of the focal plane for the various conditions, the reduction in average resolving power that may result from such differences, relative magnitudes of average resolving power for the two emulsions and effects of contrast. These are discussed in the present section.

5.1. Relative Positions of Focal Plane

The relative positions of the focal plane for the various conditions are indicated for the four lenses in table 1. The displacements for each of the contrasts and emulsions from the focal plane of best average definition for the high contrast target using VF emulsion of the corresponding planes are shown in table 2. It is clear from this table, that differences in contrast of target have little or no effect upon the location of the focal plane of best average definition for either emulsion. Only in the case of the low contrast target having light lines on a dark background (LLD) used with SP emulsion is there any indication of a possible effect on the location of the focal plane and even in this instance the apparent shift may be a result of random error.

On the average, the plane of best average definition for the various contrasts appear to be 0.15 mm nearer to the lens for the SP emulsion than is the corresponding plane for VF emulsion. This difference is small and may be real. However, it would be unlikely to present serious cause for concern in the locating of the plane of best average definition. It is likely that the average plane selected using VF emulsion will be satisfactory if this plane be used for photography with SP emulsion. Likewise the plane selected using SP emulsion would be reasonably satisfactory for photography with VF emulsion.

5.2. Reduction in Resolving Power From the Maximum

If the differences in the relative location of the focal plane are regarded as genuine, it is instructive to determine the magnitude of the effect of these differences on resolving power under the various

TABLE 1. *Variation of $\sqrt{R_\beta T_\beta}$ with separation, Δf, from the plane of best visual axial focus for four lenses*

Values of $\sqrt{R_\beta T_\beta}$ in lines per millimeter are given for two emulsions and three target contrasts. The columns, designated HDL, show values obtained with a high contrast target having dark lines on a light background. The columns, designated LDL, show values for a low contrast target having dark lines on a light background. The columns, designated LLD, show values obtained with a low contrast target having light lines on a dark background. The maximum values of $\sqrt{R_\beta T_\beta}$ are underlined. The number of test negatives used in each set of determinations is shown in the row marked *n*.

	Values of $\sqrt{R_\beta T_\beta}$ for lens No. 1 obtained with emulsion					
	VF			SP		
n	2	1	1	3	1	2
Δf	HDL	LDL	LLD	HDL	LDL	LLD
mm						
−0.45	39.3	27.2	25.2	20.0	14.6	13.5
−.30	42.0	28.9	27.8	22.2	15.3	13.8
−.15	46.4	31.3	28.3	22.9	15.4	13.7
.00	48.6	32.4	28.7	21.8	14.9	13.5
.15	48.4	29.3	26.6	19.4	12.7	11.8
.30	38.6	23.2	23.2	15.6	11.1	10.4

	Values of $\sqrt{R_\beta T_\beta}$ for lens No. 5 obtained with emulsion					
	VF			SP		
n	3	2	1	6	3	3
Δf	HDL	LDL	LLD	HDL	LDL	LLD
mm						
−0.45	30.1	22.2	22.3	19.8	14.4	13.1
−.30	34.6	26.0	24.8	21.8	15.1	14.5
.15	39.8	27.6	27.2	23.4	15.6	14.1
.00	42.2	28.8	27.2	22.8	15.2	13.8
.15	42.1	26.8	28.3	21.4	13.5	12.6
.30	36.6	23.0	23.4	17.6	11.7	10.8

	Values of $\sqrt{R_\beta T_\beta}$ for lens No. 7 obtained with emulsion					
	VF			SP		
n	4	2	2	2	1	1
Δf	HDL	LDL	LLD	HDL	LDL	LLD
mm						
−0.45	42.6	31.6	29.6	24.6	16.1	14.3
−.30	46.5	33.0	29.8	24.8	16.4	14.3
−.15	48.1	33.0	30.0	24.5	16.2	14.0
.00	46.8	32.3	29.2	23.6	16.2	13.9
.15	43.4	27.2	27.4	21.5	13.9	12.4
.30	36.5	24.2	23.4	17.9	12.8	11.1

	Values of $\sqrt{R_\beta T_\beta}$ for lens No. 8 obtained with emulsion					
	VF			SP		
n	3	1	2	2	1	1
Δf	HDL	LDL	LLD	HDL	LDL	LLD
mm						
−0.45	34.5	28.0	24.2	21.4	13.3	13.2
−.30	36.7	28.3	26.6	21.5	13.3	13.2
−.15	37.4	28.8	26.4	21.7	13.7	12.9
.00	38.9	27.8	25.9	21.0	13.4	12.5
.15	37.4	25.5	24.4	18.8	11.7	11.6
.30	33.2	23.2	21.6	17.2	10.8	10.9

TABLE 2. *Location of the focal plane of best average definition with respect to that obtained for a high contrast target using VF emulsion for four lenses*

Results are given for VF and SP emulsion and for two types of low contrast target. The symbols in the colmn heading are defined in table 1. A negative value of Δf indicates a position of a selected focal plane nearer to the lens than that selected for the high contrast target using VF emulsion. The focal plane of best average definition is determined by the maximum value of $\sqrt{R_\beta T_\beta}$.

Lens	Separations, Δf, in millimeters from plane of best average definition obtained with high contrast target for emulsion					
	VF			SP		
	HDL	LDL	LLD	HDL	LDL	LLD
1	0.00	0.00	0.00	−0.15	−0.15	−0.30
5	.00	.00	.15	−.15	−.15	−.30
7	.00	.00	.00	−.15	−.15	−.15
8	.00	−.15	−.30	−.15	−.15	−.30
Average	0.00	−0.04	−0.04	−0.15	−0.15	−0.26

TABLE 3. *Effect on average resolving power, $\sqrt{R_\beta T_\beta}$ for various contrast targets produced by using focal plane of best average definition obtained with VF emulsion for the high contrast target*

Values of the reduction from the maximum are given in percent for four lenses using VF and SP emulsions for one high and two low contrast targets. The meanings of the symbols heading the columns are as given in the caption of table 1.

Lens	Reduction in % of $\sqrt{R_\beta T_\beta}$ from its maximum for					
	VF emulsion			SP emulsion		
	HDL	LDL	LLD	HDL	LDL	LLD
1	0.0	0.0	0.0	4.8	3.2	2.2
5	.0	.0	3.9	2.6	2.6	4.8
7	.0	.0	0.0	1.2	1.2	2.1
8	.0	3.5	2.6	3.2	2.2	5.3

conditions. For example, one may select the focal plane of best average definition for high contrast targets with VF emulsion and then use this focal plane for photography under all conditions of contrast for both emulsions. This has been done and the effects on resolving power for the other conditions are shown in table 3. From this table it is clear that for 3 of the 4 lenses, there is no reduction in resolving power when using VF emulsion for the low contrast target having dark lines on a light background (LDL) while there is a 3.5 percent loss in the case of lens No. 4. For the low contrast target having light lines on a dark background, the change is zero for two lenses and reductions of 3.9 and 2.6 percent are shown for the other two. When SP emulsion is used, reductions in resolving power ranging from 1.2 to 5.3 percent occur, with the reduction under 3 percent in 7 of 12 instances. One can expect a 3 percent variation in the magnitude of $\sqrt{R_\beta T_\beta}$ on the basis of observational error, hence in only five of the twelve cases is the reduction in resolving power in excess of the probable observational error.

If the plane of best average definition for the high contrast target using SP emulsion is taken as a reference plane, values of the reductions in resolving power can be determined for the other condition.

The values of these reductions are shown in table 4. For this condition, the reduction is zero for the low contrast target (LDL) with SP emulsion. For the VF emulsion, the reduction is under 3 percent in 5 of 12 cases and does not exceed 5.6 percent for any of the remainder.

5.3. Relative Magnitude of the Resolving Power

From figures 1 and 2, it is apparent that the resolving power for VF emulsion is higher than that for SP emulsion for all values of β ranging from 0° to 40°. It is moreover clear that this is true for all three conditions of contrast. It is not possible to determine a numerical value of the ratio of the resolving powers that would be invariant for all values of β and all values of Δf. Accordingly, average values of the ratios based upon the values of $\sqrt{R_\beta T_\beta}$ shown in table 1 have been determined for each lens and are shown in table 5. In table 5, the ratios of average resolving power for the two emulsions and three contrasts with respect to the average resolving power for the high contrast target obtained with SP emulsions for four lenses. From the average values of the ratios given in this table, an estimate can be made of the probable value of other ratios that are of interest. For example, values of resolving power obtained with the low contrast target are approximately two-thirds of that obtained with the high contrast target for either of the two emulsions.

TABLE 4. *Effect on average resolving power, $\sqrt{R_\beta T_\beta}$ for various contrast targets produced by using focal plane of best average definition obtained with SP emulsion for the high contrast target*

Values of the reduction from the maximum are given in percent for four lenses using VF and SP emulsions for one high and two low contrast targets. The meanings of the symbols heading the columns are as given in the caption of table 1

Lens	Reduction in % of $\sqrt{R_\beta T_\beta}$ from its maximum for					
	VF emulsion			SP emulsion		
	HDL	LDL	LLD	HDL	LDL	LLD
1	4.5	3.4	1.4	0.0	0.0	0.7
5	5.6	4.2	3.9	.0	.0	2.8
7	3.3	0.0	0.7	.0	.0	0.0
8	3.8	.0	.8	.0	.0	2.3

TABLE 5. *Ratios of average resolving powers for two emulsions and three targets of various contrasts*

Ratios are given showing the relative magnitude of the average resolving power obtained under specified conditions to that obtained with a high contrast target on SP emulsion. Values are given for four lenses, using two emulsions and three contrasts. Values of the averages are given together with the average probable error $\overline{PE}_a$ of a single determination. The meanings of the symbols heading the columns are as given in the caption of table 1.

Lens	Ratios of average resolving powers for					
	VF emulsion			SP emulsion		
	HDL	LDL	LLD	HDL	LDL	LLD
1	2.17	1.42	1.32	1.00	0.69	0.63
5	1.77	1.22	1.21	1.00	.67	.62
7	1.93	1.32	1.24	1.00	.67	.59
8	1.80	1.33	1.23	1.00	.63	.63
Average	1.92	1.32	1.25	1.00	0.66	0.62
$\overline{PE}_a$ (%)	±6.9	±4.0	±2.8	----------	±2.6	±2.1

5.4. Effect of Reversed Contrast

In many specifications that require measurements of resolving power of lenses with low contrast targets, it is stipulated that the test chart shall consist of light lines on a dark background. This is so specified because of the belief that the use of a target having dark lines on a light background will result in lower measured values of resolving power than would be found with a target of opposite contrast because of the effect of veiling glare [3]. In figures 1 and 2, the curves marked 2 show values of $\sqrt{R_\beta T_\beta}$ as a function of Δf for the low contrast target having dark lines on a light background; the curves marked 3 show values of $\sqrt{R_\beta T_\beta}$ as a fraction of Δf for a low contrast target having light lines on a dark background. It is noteworthy that in most instances, the curve marked 2 lies slightly above the curve marked 3. Even if one ascribes the difference to experimental error, it is improbable that such error could reduce all of the observed values of curve 2 below those for curve 3. From these results, it is clear that the values of resolving power obtained using targets having dark lines on a light background are not lower than those obtained using targets having light lines on a dark background when the difference in log luminance between line and background is 0.2.

It seems probable, therefore, that when resolving power tests are made using transparent charts located in the focal plane of collimators, the use of light lines on a dark background will not, in general, yield higher values of the resolving power than will the use of dark lines on a light background. In this case, the values of resolving power are not noticeably reduced by the effect of veiling glare. Although veiling glare may affect the values of resolving power on the axis which may be the case for lens No. 5 in figure 2, it is not likely to do so for extra-axial imagery. The effect of veiling glare possibly would be more pronounced in using resolution targets on a range rather than in collimators which may account for the prevalence of the specification of targets having light lines on a dark background.

6. Conclusion

In this study, the effect of contrast upon choice of a focal plane has been investigated using four lenses, two target contrasts, and two emulsions. Analysis of the results of measurement leads to the following conclusions.

(1) For either of the two emulsions used, the choice of focal plane of best average definition is not affected by differences in contrast between lines and background in the target.

(2) When a lens images targets where the difference in log luminance between lines and background equals 0.20, the values of measured resolving power are not significantly affected by reversal of target contrast. In other words, low contrast targets with either dark lines on a light background or light lines on a dark background will yield substantially the same measured values of average resolving power for a given lens.

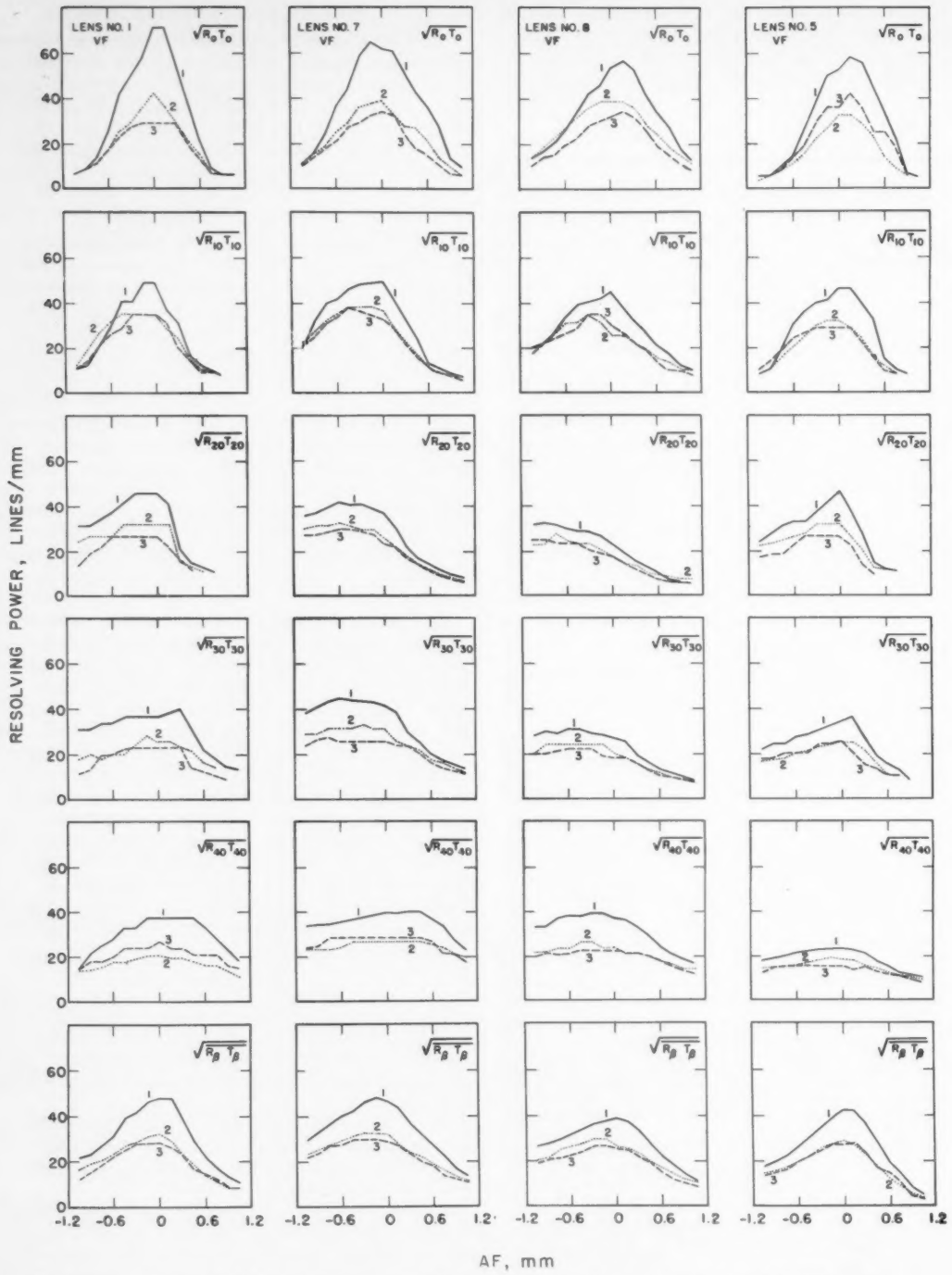

FIGURE 1. *Average resolving powers versus position of the image plane for four lenses with VF emulsion.*

Values of the average resolving power $\sqrt{R_\beta T_\beta}$ are shown at 10° intervals from 0° to 40°. The lowest box in each column shows values of $\sqrt{R_\beta T_\beta}$. Curve 1 shows the result obtained with a high contrast target having dark lines on a light background with contrast between lines and background greater than 2.0 on a density scale. Curve 2 shows the results for a low contrast target (0.2 difference of log luminance between lines and background), having dark lines on a light background. Curve 3 shows results obtained for a low contrast target (0.2 difference of log luminance between lines and background) but having light lines on a dark background. The zero of abscissas marks the position of best visual axial focus, and positive values of Δf indicate positions farther from the lens.

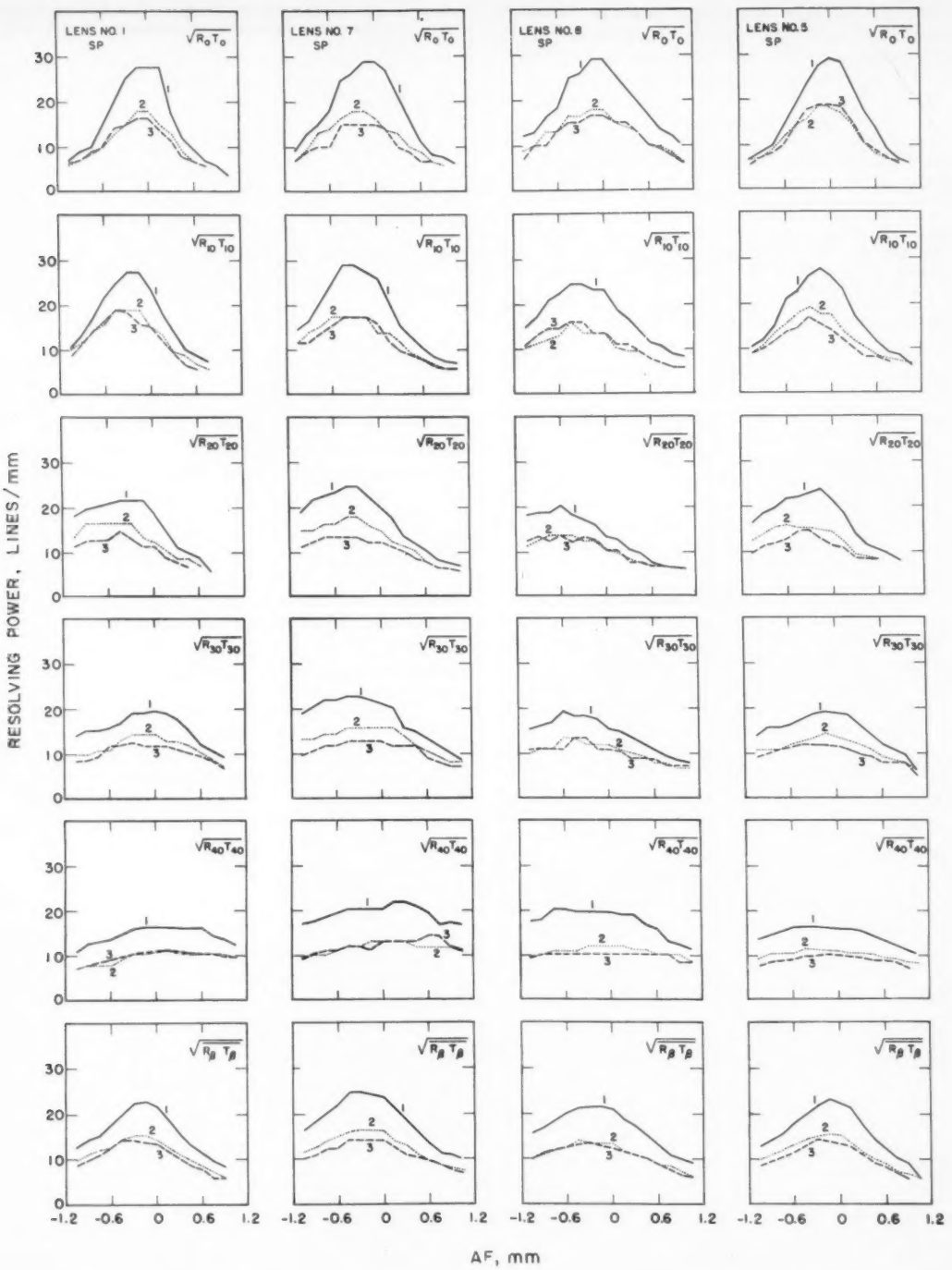

FIGURE 2. *Average resolving power versus position of the image plane for four lenses with SP emulsion.*

Values of the average resolving power $\sqrt{R_\beta T_\beta}$ are shown at 10° intervals from 0° to 40°. The lowest box in each column shows values of $\sqrt{R_\beta T_\beta}$. Curve 1 shows the results obtained with a high contrast target having dark lines on a light background with contrast between lines and background greater than 2.0 on a density scale. Curve 2 shows the results for a low contrast target (0.2 difference of log luminance between lines and background), having dark lines on a light background. Curve 3 shows results obtained for a low contrast target (0.2 difference of log luminance between lines and background) but having light lines on a dark background. The zero of abscissas marks the position of best visual axial focus, and positive values of Δf indicate positions farther from the lens.

The authors express their appreciation to other members of the staff of the National Bureau of Standards for assistance during this work and in particular to E. C. Watts who prepared the illustrations.

7. References

[1] Military Standard MIL–STD–150, Photographic Lenses, 23 Oct. 1950.
[2] Military Standard MIL–STD–150A, Photographic Lenses, 12 May 1959.
[3] Report of Commission I, International Society of Photogrammetry Specification of methods of calibrating photogrammetric cameras, Photogrammetria X, 85 (1953–1954).
[4] L. E. Howlett, Photographic resolving power, Canadian Journal of Research **24A**, 15–40 (1946).
[5] F. E. Washer and I. C. Gardner, Method for determining the resolving power of photographic lenses, NBS Circ. 533 (1953).
[6] F. H. Perrin and J. H. Altman, Studies in the resolving power of photographic emulsions, J. Opt. Soc. Am. **43,** 780 (1953).
[7] P. Hariharan, Resolving power of photographic emulsions, J. Opt. Soc. Am. **46,** 315 (1956).
[8] F. E. Washer and W. P. Tayman, Location of the plane of best average definition for airplane camera lenses, Photogrammetric Engineering XXVI, 475 (1960).
[9] F. E. Washer and W. P. Tayman, Variation of resolving power and type of test pattern, J. Research NBS **64C**, 209 (1960).
[10] I. C. Gardner and F. A. Case, Precision camera for testing lenses, J. Research NBS **18,** 449 (1937).

(Paper 65C3-71)

JOURNAL OF RESEARCH of the National Bureau of Standards—C. Engineering and Instrumentation
Vol. 65C, No. 3, July–September 1961

Influence of Temperature and Relative Humidity on the Photographic Response to Co^{60} Gamma Radiation*

Margarete Ehrlich

(January 24, 1961)

At relative humidities close to a hundred percent, bare film packets are unsatisfactory for personnel dosimetry, regardless of temperature. Sealed polyethylene bags afford considerable protection from excessive humidity.

1. Introduction

Fading characteristics of the photographic latent image are known to depend on the type of emulsion, the temperature, humidity, and chemical contamination of the atmosphere, as well as on the type of radiation exposure [1].[1] Because of the variety of conditions under which photographic personnel dosimeters are presently used, and because of the long periods of time over which they are carried, a knowledge of the fading characteristics of the photographic latent image is of considerable importance in personnel dosimetry.

Early fading studies performed at the National Bureau of Standards on the latent image formed with X-rays were carried out over a period of only one week; all films were exposed at laboratory temperatures to low-energy X-radiation and then stored for the prescribed length of time at about 25 °C and 45 percent relative humidity [2]. More recently, Ziegler and Chleck [3] carried out fading studies over a period of 90 days, on films exposed at laboratory temperatures and stored at temperatures between 27 and 34 °C, either in air without humidity control, or in a dry atmosphere of argon. Tomoda et al. [4, 5] did latent-image fading studies on several types of X-ray film exposed at laboratory temperatures and stored up to 30 days at 30° C at relative humidities between 40 and 75 percent.

The aim of the present study was to determine the response of one type of the more widely used dosimeter films under conditions simulating as closely as possible the temperatures and relative humidities that may be encountered during its use in personnel dosimetry. The films were used in their original packets, which had been sealed commercially into polyethylene bags. For the irradiation, one set of packets was removed from the polyethylene bags, the other set remained protected. All film packets were exposed to Co^{60} gamma radiation of low intensity for a period of about 1 month under 1 of 12 different combinations of atmospheric temperature and relative humidity. After completion of the exposures, all film packets were enclosed in polyethylene and placed in a refrigerator. About 5 days later they were developed according to conventional procedure, along with control films exposed at room temperature.

*The work was supported by the U.S. Atomic Energy Commission.

[1] Figures in brackets indicate the literature references at the end of this paper.

Tomoda found that different film types behaved similarly under his experimental conditions [5]. The experimental conditions employed here differ from those of Ziegler and Chleck and also from those of Tomoda, who exposed at room temperature and heated the films after exposure. However, it is reasonable to assume that different types of film will also behave similarly under the conditions of the present experiment. Therefore, the results obtained here for one dosimeter film should be applicable to other film types as well.

2. Experimental Technique

A sealed Co^{60} source with an activity of about 50 μc was placed in the center of a spiral array of lead-enclosed wooden supports, each holding a sealed glass jar containing a small amount of saturated salt solution that produced a known relative humidity within the jar. Four different relative humidities were obtained by using lithium chloride, magnesium chloride, sodium chloride, and potassium sulfate, listed in the order of increasing values of relative humidities. The exact humidity value for each of the three temperatures used was taken from the data of Wexler and Hasegawa [6]. At the temperatures employed for the experiments, the amount of solutes present in the gaseous phase was negligible.

Each glass jar contained two film packets, one bare and one sealed in a polyethylene bag. The packets were supported by small clamps glued to the inside of the jar lids. The walls of the jars were thick enough to establish electronic equilibrium for Co^{60} radiation at the inner wall surface. They absorbed about 2 percent of the incident Co^{60} gamma rays.

A total of 24 jars was used. The source-to-jar distances were chosen in such a way as to yield 5 different film exposures at each of the 4 different relative humidities; also 1 jar at each relative humidity was shielded from the radiation.

The entire setup was placed in a room whose temperature was held as closely as possible at a constant value for 1 month. About 5 days after completion of the exposure, the films were developed in Kodak Liquid X-ray Developer for 5 min at 20 °C, along with "control films". The control films were exposed at room temperature to the radiation from a stronger Co^{60} source about 4 days prior to develop-

ment; all control packets were enclosed in polyethylene and were supported from the lids of dry jars during the exposures which lasted for 1 to 30 min. The same procedure was followed for 3 consecutive months, during which the exposure room was maintained at 3 different temperatures.

3. Results

The table shows the net densities (i.e., the densities above base and fog) obtained at the 4 different exposure levels and for each of the 12 exposure conditions; the listed values were taken from curves of the plotted experimental data. The uncertainty in the exposures is estimated to be less than 10 percent, while that in the density readings is less than 0.02 density units. The tabulation enables the reader to plot, for purposes of comparison, one characteristic curve for each exposure condition. However, comparisons should be made only between the densities obtained at one temperature, since only the films exposed at the same temperature were developed simultaneously.

The table also lists the photographic sensitivities relative to the sensitivity of the controls for all exposure conditions.[2] At 5.5 °C all sensitivities but those obtained at 98.3 percent relative humidity were within 10 percent of the values for the controls. However, at 98.3 percent relative humidity, the sensitivity was considerably lower. At this high humidity, the film exposed in a polyethylene bag to 0.25 *r* reached the same density as the film exposed to 1.0 *r* in a bare packet. The 12-percent difference between the sensitivity of the controls and that obtained at 98.3 percent relative humidity with the film packets inside the polyethylene bags may be real, inasmuch as polyethylene is not entirely impermeable to water vapor.

[2] Photographic sensitivity is here defined as the reciprocal of the exposure in *r* required for a given density. The sensitivity values used for the tables are averages of the sensitivities determined at the density levels 0.2 and 0.5.

At 19.8 °C, the influence of high humidity was even more pronounced. Here, 0.5 *r* given to a film in a bare packet in an atmosphere of 97.2 percent relative humidity produced no measurable density above background, while at lower relative humidities the bare films showed a tendency to fog. The sensitivity of the films exposed in polyethylene-enclosed packets was not significantly different from that of the control.

At 32.5 °C, there was a significant increase in the sensitivity of all films, as much as 30 percent for films protected from atmospheric changes. This was to be expected on the basis of the kinetics of the photographic process [7]. However, superimposed on this effect was, in the case of the bare packets, the effect of the varying atmospheric conditions. As a result, the films exposed in bare packets at relative humidities up to 75.6 percent showed an additional sensitivity increase of up to 15 percent. At a relative humidity of 96.5 percent, the films were tightly stuck to adjacent films contained in the same packets. During the process of separation, they were damaged considerably. The undamaged portions of the exposed films were fogged to a degree that made evaluation impossible. The density of the corresponding unexposed film, although higher than that of the film in the protected packet, was measurable. The density of the heated, unexposed film from the packet protected by polyethylene was not appreciably higher than that of the unexposed control film, which had been kept at room temperature.

4. Conclusions

Regardless of temperature, bare film packets cannot be used for satisfactory personnel dosimetry in areas where prolonged exposure to relative humidities close to a hundred percent are expected. Such high relative humidities cause physical damage to the film packets; moreover, at low temperatures,

Change in film response with temperature and relative humidity

Temperature	Relative humidity	Net density for exposure of the jars to								Relative sensitivity	
		0.10 *r*		0.25 *r*		0.50 *r*		1.00 *r*			
		Bare	Plastic	Bare	Plastic	Bare	Plastic	Bare	Plastic	Bare	Plastic
°C	%										
5.5±3.5	13.9±1	0.02	0.04	0.08	0.09	0.22	0.22	0.46	0.43	1.00	1.05
	34.5±2	.03	.03	.10	.10	.23	.23	.44	.44	.98	.98
	75.1±0.6	.03	.03	.09	.09	.21	.21	.45	.45	.96	.96
	98.3± .7	[a]0	.02	[a]0	.09	[a].02	.19	[a].09	.40	very low	.88
			[c].03		[c].09		[c].22		[c].46		[c]1.00
19.8±0.5	12.4±0.5	0.03	0.03	0.10	0.08	0.19	0.16	0.42	0.37	1.11	0.98
	33.5± .5	.03	.03	.08	.07	.16	.15	.37	.35	1.00	.93
	75.5± .6	.03	.03	.10	.08	.21	.18	.44	.39	1.16	1.02
	97.2± .5	[a]0	.03	[a]0	.09	[a]0	.17	[a].025	.38	very low	1.02
			[c].03		[c].07		[c].17		[c].38		[c]1.00
32.5±1	11.7±0.5	0.06	0.03	0.12	0.10	0.27	0.23	0.54	0.49	1.45	1.29
	32.6± .5	.04	.04	.12	.12	.21	.21	.44	.44	1.22	1.22
	75.6± .7	.06	.03	.13	.08	.26	.20	.49	.40	1.38	1.07
	96.5± .5	[a]1.70	.06	[a]1.68	.12	[a]1.75	.22	[a]1.85	.44	[a,b]>4	1.22
			[c].02		.08		[c].18		[c].37		[c]1.00

[a] The films stuck to adjacent films during exposure and had to be forced apart with a knife.
[b] Numerical evaluation impossible.
[c] Controls, exposed at laboratory temperature in dry jars.

they produce excessive fading of the latent image and, at high temperatures, are the cause of emulsion fogging.

Personnel badge calibrations are usually made at normal laboratory temperatures, regardless of the ambient temperatures at which the personnel badges are to be used. When the temperatures are higher during use, one expects the personnel exposures to be overestimated. This error is less when the film packets that are to be used in the personnel badges are sealed in polyethylene bags. Thus, although polyethylene is not completely impermeable to water vapor, it does provide a considerable measure of protection to photographic film exposed under conditions of excessive atmospheric humidity.

5. References

[1] See, for instance, P. Demers, Les émulsions nucléaires, principes et applications, Ionographie, pp. 186–194, Les Presses Universitaires de Montréal (1958).

[2] W. L. McLaughlin, M. Ehrlich, Nucleonics **12,** 34–36 (1954).

[3] C. A. Ziegler, D. J. Chleck, Health Physics **4,** 32–34 (1960).

[4] Y. Tomoda, N. Nakamura, J. Soc. Sci. Phot. Japan, **21,** 16–19 (1958).

[5] Y. Tomoda, J. Soc. Sci. Phot. Japan, **22,** 12–17 (1959); see also abstract in Phot. Sci. and Eng. **4,** 59 (1960).

[6] A. Wexler, S. Hasegawa, J. Research NBS **53,** 19–26 (1954).

[7] For the influence of temperature on the latent image formed by X-rays, see, for instance, M. Ehrlich, Photographic Dosimetry of X- and Gamma Rays, NBS Handbook 57 (1954).

(Paper 65C3–72)

JOURNAL OF RESEARCH of the National Bureau of Standards—C. Engineering and Instrumentation
Vol. 65C, No. 3, July–September 1961

Publications of the National Bureau of Standards*

Selected Abstracts

Evaluation of the NBS Unit of resistance based on a computable capacitor, R. D. Cutkosky, *J. Research NBS* **65A** (*Phys. and Chem.*) *No. 3, 147 (May–June 1961) 75 cents.*
An evaluation of the unit of resistance maintained at the National Bureau of Standards, based on the prototype standards of length and time, is described. The evaluation is based on a nominally one-picofarad capacitor whose value may be calculated from its mechanical dimensions to high accuracy. This capacitor is used to calibrate an 0.01-microfarad capacitor. A frequency-dependent bridge involving this capacitor establishes the value of a 10^4-ohm resistor. Comparison of that resistor with the bank of one-ohm resistors maintaining the NBS unit of resistance establishes that this unit is

$$\Omega_{BU} = 1.000002_3 \text{ ohms} \pm 2.1 \text{ ppm.}$$

The indicated uncertainty is an estimated 50 percent error of the reported value based on the statistical uncertainty of the measurements and allowing for known sources of possible systematic errors other than in the speed of light, and assuming that the speed of light is $c = 2.997925 \times 10^{10}$cm/sec.

Digital methods for the extraction of phase and amplitude information from a modulated signal, R. S. Lawrence, J. L. Jespersen, and R. C. Lamb, *J. Research NBS* **65D** (*Radio Prop.*) *No. 4, 351 (July-August 1961) 75 cents.*
A description is given of three digital methods which have been used to recover amplitude and phase information from a modulated sinusoidal signal sampled at equal intervals of not more than one-sixth of a period. The first method, the "zero-crossing" method, is economical of computer time and, for modulation which is not too deep and does not contain frequencies near the carrier frequency, accurately recovers the phase and amplitude modulation. The second method the "filter" method, is more laborious but it gives better accuracy and will operate with deeper and more rapid modulation. The third method, a statistical approach, will work with severly overmodulated signals, but it yields only a statistical summary of the modulation. The methods were designed specifically for analysis of radio-star scintillation records but they may be applied to many other modulated signals.

Development of high-temperature strain gages, J. W. Pitts and D. G. Moore, *NBS Mono. 26 (1961) 20 cents.*
A summary is presented of a research program aimed at the improvement of high-temperature strain gages of the electrical resistance type. Potential ceramic and metal components were evaluated and a gage was devised that was based on these evaluations. This gage (NBS 5B) was flexible and easy to install; however, it lacked resistance stability at higher temperatures. In an attempt to minimize this deficiency, ceramic cements were developed that showed greater electrical resistivity than had been previously observed in the range 800 to 1,800 °F; also, a technique was devised for increasing the resistance to ground by applying a fired-on ceramic coating to the grid of a specially developed unbacked gage.
A study was made of the cause of the erratic response of cemented gages that had not been preheated prior to use. There were strong indications that the erratic response was caused mostly by the rapid decrease in resistance that accompanied structural changes in the cement.

Precision measurement and calibration, S. F. Booth: **Electricity and electronics,** *NBS Handb. 77, Vol. I (1961) $6.00;* **Heat and mechanics,** *Vol. II (1961) $6.75;* **Optics, metrology, and radiation,** *Vol. III (1961) $7.00.*
This Handbook is a compilation of the more important National Bureau of Standards publications over a period of years, dealing with precision measurement and the calibration of standards. The publications, originally issued as circulars, research papers, chapters of books, and articles in scientific periodicals, were selected for inclusion in the Handbook on the basis of their having, in the past, best served the needs of scientists in specialized fields of measurement. It is intended to serve as a quick reference source for workers in the field of standards, and also as a textbook and aid to scientists and engineers in standards laboratories. The list of specific titles included in each volume is given in the Table of Contents of that volume. Because the three volumes are sold separately, the subject index and authors' index are complete and identical in each volume.

Units of weight and measure (United States customary and metric) definitions and tables of equivalents, L. V. Judson, *NBS Misc. Publ., 233 (1960) 40 cents.*
The units of length, area, volume, capacity, and mass in the United States are defined. Tables of interrelation and tables of equivalents for these units in the metric system and in the U.S. customary system are given. All values in the text and in the tables have been revised to be in accord with the Federal Register announcement of July 1, 1959, an announcement entitled "Refinement of Values for the Yard and Pound" in accordance with an agreement among the directors of National Standards Laboratories of English-speaking nations to obtain uniformity in precise measurements involving the yard and the pound. The long tables were all recomputed on an automatic computer and printer. Material on the status of the metric system in the United States was deleted as not being germane to the main purpose of the publication. The tables showing interrelation (1 to 999 units) between bushels and hectoliters were deleted. A more complete table (0.01 to 19.99 units) showing equivalents of inches in millimeters has been added. This is a revision of Miscellaneous Publications 214.

Report of the 45th national conference on weights and measures 1960, *NBS Misc. Publ. 235 (1960) 75 cents.*
A report of the proceedings of the forty-fifth National Conference on Weights and Measures, held in Washington, D.C., June 6, 7, 8, 9, and 10, 1960, and attended by state, county, and city weights and measures officials. 159 pages.

The sample, the procedure, and the laboratory, W. J. Youden, *Anal. Chem.* **32,** *No. 13, 23A–37A (Dec. 1960).*
Statistics is accorded a place in the activities of analytical chemists because analysts are interested in tracking down the sources of error in their determinations. Uniformity of the material samples, the inherent capacity of a procedure to give precise results free from systematic errors and the careful adherence of the analyst to the prescribed procedure are all involved in the final result. When different laboratories analyse the same materials the results usually show much greater discrepancies than that found for determinations made by one laboratory.
This paper describes (1) a logical breakdown of the analytical error into meaningful components; and (2) a graphical method for presenting the results that clearly differentiates between random and systematic errors.

Evaluation of resistance strain gages at elevated temperatures, R. L. Bloss, *Am. Soc. Testing Materials Proc.* **1,** *No. 1, 9–15 (Jan. 1961).*
To satisfy the need for strain measurements at elevated temperatures a number of types of "high temperature" strain gages are available. A comprehensive evaluation of these gages is needed because of the lack of available information on their performance and because of difficulty which has been encountered in their use. A facility for conducting such an evaluation is described. Typical results obtained during evaluation tests are given to show the capability of the equipment, to point out some of the problems encountered in the use of these gages, and to illustrate the need for comprehensive gage evaluation prior to use. The results shown are only indicative of the performance of the particular gage tested. Significantly different results might be obtained from other gage types.

Techniques in calorimetry. I. A noble-metal thermocouple for differential use, E. D. West, *Rev. Sci. Inst.* **31,** *No. 8, 896–897 (Aug. 1960).*
The application of a noble-metal thermocouple to problems of the observation and control of temperature differences in calorimetry is described. For a couple of gold-40%-palladium and platinum-10%-rhodium dE/dT is 37 to 57 microvolts/°C from 25° to 1100°C. The uncertainty in the temperature difference measured by a 20-junction thermopile in a nearly isothermal region is less than 0.4 millidegrees.

Evaluation of micrometer and microscopical methods for measuring thickness of floor coverings, E. Horowitz, J. Mandel, R. J. Capott, and T. H. Boone, *ASTM Bull.* **1,** *No. 2, 99–102 (Feb. 1961).*
The dial micrometer and microscopical (optical) methods for measuring the thickness of floor coverings were evaluated in an interlaboratory study of four samples having wearing layer thicknesses in the range 5.5 to 22 mils. The data are analyzed statistically in terms of three parameters: (1) The overall average, μ; (2) the slope of the straight line obtained by plotting the average results of a given participant versus the corresponding grand average of all the participants, β; and (3) the scatter of the individual results about the straight line, $V(\eta)$. With experienced personnel, there is no significant difference in the results obtained by the two methods; the grand averages agree to within 0.04 mils. Using four replicate measurements the standard deviations for the micrometer and optical methods are 1.15 and 1.19 mils, respectively. The measurement of thickness does not appear to be affected by different diameter pressure feet between the limits of 0.10 and 0.25 inches when the load on the pressure foot is maintained between 18.6 and 22.4 lb/in^2.

Standards and testing, the key to quality, B. E. Foster, *Eng. Bull., Purdue Univ.* **XLIV,** *No. 6, 54–62 (Nov. 1960).*
Measurement standards, dimensional standards, quality standards, and construction standards are briefly discussed. The advantages of quality standards in furnishing guidance to the selection of materials, in promoting uniformity of materials purchased, and from the contractural standpoint are brought out. The importance of testing is emphasized.

An analysis of the accumulated error in a hierarchy of calibrations, E. L. Crow, *IRE Trans. Instrumentation* **I-9,** *No. 2, 105–114 (Sept. 1960).*
Calibrations of many types are performed in a hierarchy of calibration laboratories fanning out from a national standard. Often the statement is made that the accuracy of each echelon of the hierarchy should be 10 times the accuracy of the immediately following echelon. The validity of such statements is examined by deriving formulas for the total error accumulated over the entire sequence when systematic and random errors may occur in each echelon, and by determining how a given total error may be achieved at minimum total cost under reasonable assumptions for the form of the cost-error functions.

A recommended standard resistor-noise test system, G. T. Conrad, Jr., M. Newman, and A. P. Stansbury, *IRE Trans. Component Parts,* **CP-7,** *No. 3, 71–88 (Sept. 1960).*
This paper describes a recommended standard resistor noise test system, with the theroy of operation given in considerable detail. The system provides for the measurement of a definitive resistor noise quality Index. This Index, the "microvolts-per-volt" Index, is a modified form of the "conversion gain" index formerly used at NBS. The Index is a decibel expression for the number of microvolts of noise per volt of applied dc voltage transmitted in a frequency decade. A practical example is given to illustrate how the Index may be used to calculate the magnitude of current noise generated by fixed resistors in a given application. To complete the example, the combined effects of thermal noise, tube noise, and current noise are then considered.
A description is also given of an existing test set which is based upon specifications associated with the recommended measuring system. The full specifications for this set are given and distinctive design features are discussed. The simple operation of the test set and the computation of the Index are carefully explained.

A transfer instrument for the intercomparison of microwave power meters, C. F. Engen, *IRE Trans. Instrumentation* **I-9,** *No. 2, 202–208 (Sept. 1960).*
In the intercomparison of two microwave power standards, or in the calibration of a microwave power meter by means of a second or "standard" power meter, the measurement of microwave impedance has played a major role.
Through an extension of the reflectometer concept it is now possible to devise a four arm junction which, when properly adjusted, makes possible the intercomparison or calibration of such power meters with little or no regard for their impedance characteristics. In addition, the method is substantially independent of the impedance discontinuity which may be present at the input flange or connector. This latter result is of particular value in coaxial systems.

Propagation of error in a chain of standards, A. G. McNish and J. M. Cameron, *IRE Trans. Instrumentation* **I-9,** *No. 2, 101–104 (Sept. 1960).*
Methods for dealing with errors developed in individual laboratories in a chain of standardizing laboratories must be considered with respect to the end result. It is shown that if a large number of laboratories is involved in the chain the most satisfactory results are obtained by regarding the total error of the chain as the root of the sum of the squares of the errors of the individual laboratories. If only a few laboratories are involved it is safer, and satisfactory too, to add the individual errors.

Other NBS Publications

Journal of Research 65A (Phys. and Chem.) No. 2 (March–April 1961) 75 cents.
Mass spectra of some deuteroethanes. E. I. Quinn and F. L. Mohler.
Heats of hydrolysis and formation of potassium borohydride. W. H. Johnson, R. H. Schumm, I. H. Wilson, and E. J. Prosen.
Heat of combustion of borazine $B_3N_3H_6$. M. V. Kilday, W. H. Johnson, and E. J. Prosen.
Thermodynamic properties of thorium dioxide from 298 to 1,200 °K. A. C. Victor and T. B. Douglas.
Calculated energy dissipation distribution in air by fast electrons from a gun source. J. E. Crew.
Vitrons as flow units in alkali silicate binary glasses. L. W. Tilton.
Tetragermanates of strontium, lead, and barium of formula type AB_4O_9. C. R. Robbins and E. M. Levin.

Journal of Research 65A (Phys. and Chem.) No. 3 (May–June 1961) 75 cents.
International practical temperature scale of 1948. Text revision of 1960. H. F. Stimson.
Evaluation of the NBS unit of resistance based on a computable capacitor. R. D. Cutkosky. (See above abstract.)
Wavelengths and intensities in the first spectrum of bromine, 2000 to 13000 A. J. L. Tech and C. H. Corliss.
Torsional resonance vibrations of uniform bars of square cross section. W. E. Tefft and S. Spinner.

Infrared studies of aragonite, calcite, and vaterite type structures in the borates, carbonates, and nitrates. C. E. Weir and E. R. Lippincott.

Dielectric properties of polyamides: polyhexamethylene adipamide and polyhexamethylene sebacamide. A. J. Curtis.

Heat of formation of calcium aluminate monocarbonate at 25 °C. H. A. Berman and E. S. Newman.

Thermodynamic constants for association of isomeric chlorobenzoic and toluic acids with 1,3-diphenylguanidine in benzene. M. M. Davis and H. B. Hetzer.

Heats of combustion and formation of trimethylborane, triethylborane, and tri-*n*-butylborane. W. H. Johnson, M. V. Kilday, and E. J. Prosen.

Pyrolysis of linear copolymers of ethylene and propylene. S. Straus and L. A. Wall.

Pyrolysis of fluorocarbon polymers. L. A. Wall and S. Straus.

Preparation of fluoro- and bromofluoroaryl compounds by copyrolysis of bromofluoroalkanes. L. A. Wall, J. E. Fearn, W. J. Pummer, and R. E. Lowry.

Thermal stability of polydivinylbenzene and of copolymers of styrene with divinylbenzene and with tribinylbenzene. S. Straus and S. L. Madorsky.

Conformations of the pyranoid sugars. IV. Infrared absorption spectra of some fully acetylated pyranoses. R. S. Tipson and H. S. Isbell.

A standard for the measurement of the *p*H of blood and other physiological media. V. E. Bower, M. Paabo, and R. G. Bates.

Journal of Research 65B (Math. and Math. Phys.) No. 2 (April–June 1961) 70 cents.

Optimal approximation for functions prescribed at equally spaced points. H. F. Weinberger.

Truncations in the method of intermediate problems for lower bounds to eigenvalues. N. W. Bazley and D. W. Fox.

Comparison theorems for symmetric functions of characteristic roots. M. Marcus.

Some properties of the empirical distribution function of a random process. M. M. Siddiqui.

Another extension of Heinz's inequality. M. Marcus.

Mean motions in conditionally periodic separable systems. J. P. Vinti.

Some boundary value problems involving plasma media. J. R. Wait.

A new decomposition formula in the theory of elasticity. J. H. Bramble and L. E. Payne.

Pointwise bounds in the Cauchy problem of elastic plates. L. E. Payne.

Journal of Research 65D (Radio Prop.) No. 4 (July-August 1961) 75 cents.

Almost fifty years of URSI. J. H. Dellinger.

Power density requirements for airglow excitation by gyrowaves. V. A. Bailey.

On the validity of some approximations to the Appleton-Hartree formula. K. Davies and G. A. M. King.

Amplitude and angular scintillations of the radio source Cygnus-A observed at Boulder, Colorado. R. S. Lawrence, J. L. Jespersen, and R. C. Lamb.

Digital methods for the extraction of phase and amplitude information from a modulated signal. R. S. Lawrence, J. L. Jespersen, and R. C. Lamb. (See above abstract.)

Comparison between mode theory and ray theory of VLF propagation. H. Volland.

Antenna coupling error in direction finders. C. W. Harrison, Jr.

The electrically short antenna as a probe for measuring free electron densities and collision frequencies in an ionized region. R. W. P. King, C. W. Harrison, Jr., and D. H. Denton, Jr.

Effect of multiple atmospheric inversions on tropospheric radio propagation. F. H. Northover.

A few observations of the perturbations in the phase of the low-frequency ground wave. J. M. Ross and J. E. Kirch.

Smooth earth diffraction calculations for horizontal polarization. L. E. Vogler.

On the theory of mixed-path ground-wave propagation on a spherical earth. J. R. Wait.

Atomic energy levels in crystals, J. L. Prather, NBS Mono. 19 (1961) 60 cents.

Climatic charts and data of the radio refractive index for the United States and the world, B. R. Bean, J. D. Horn, and A. M. Ozanich, Jr., NBS Mono. 22 (1960) $2.00.

A spectrophotometric atlas of the spectrum of CH from 3000A to 5000A, A. M. Bass and H. P. Broida, NBS Mono. 24 (1961) 20 cents.

Measurement of absorbed dose of neutrons, and of mixtures of neutrons and gamma rays, NBS Handb. H75 (1961) 35 cents.

Medical X-ray protection up to three million volts, NBS Handb. H76 (1961) 25 cents.

Report of the International Commission on Radiological Units and Measurements (ICRU) 1959, NBS Handb. H78 (1961) 65 cents.

Quarterly radio noise data—June, July, August 1960, W. Q. Crichlow, R. T. Disney, and M. A. Jenkins, NBS TN18–7 (PB151377–7) (1960) $1.75.

Quarterly radio noise data, September, October, November 1960, W. Q. Crichlow, R. T. Disney, and M. A. Jenkins, NBS TN18–8 (PB151377–8) (1961) $1.75.

VHF radio propagation data for Cedar Rapids-Sterling, Anchorage-Barrow, and Fargo-Churchill test paths April 1951 through June 1958, G. R. Sugar and K. W. Sullivan, NBS TN79 (PB161580) (1960) $4.00.

Bibliography of tropospheric radio wave scattering, R. L. Abbott, NBS TN80 (PB161581) (1960) $2.25.

A survey of spread-f, F. M. Glover, NBS TN82 (PB161583) (1960) $1.75.

The NBS meteor-burst propagation project—a progress report, C. E. Hornback, L. D. Brayfogle, and G. R. Sugar, NBS TN86 (PB161587) (1960) $1.25.

A theoretical study of sporadic-E structure in the light of radio measurements, K. Tao, NBS TN87 (PB161588) (1961) $1.25.

Prolonged space-wave fadeouts in tropospheric propagation, A. P. Barsis and M. E. Johnson, NBS TN88 (PB161589) (1961) $2.00.

Some ceramic dielectrics with a very low temperature coefficient of capacitance, S. Marzullo and E. N. Bunting, J. Am. Ceram. Soc. **43,** No. 11, 609, (Nov. 1960).

Vibration-rotation bands of H_2O, E. D. Tidwell and E. K. Plyler, J. Opt. Soc. Am. **50,** No. 12, 717–720 (Dec. 1960).

Nuclear magnetic resonance in tantalum metal, J. I. Budnick and L. N. Bennett, J. Phys. Chem. Solids **16,** No. 1/2, 37–38 (Jan. 12, 1960).

The relation of $h_{max}F2$ to M(3000)F2 and H_pF2, J. W. Wright and R. E. McDuffie, J. Radio Research Lab. **7,** No. 32, 409–420 (July 1960).

8-quinolinol precipitation of the elements, J. I. Hoffman, Chem. Anal. **49,** No. 4, 126 (Dec. 1960).

Dipole moments of hydrocarbons, D. R. Lide, Jr., J. Chem. Phys. **33,** No. 6, 1879 (Dec. 1960).

Collection of ions produced by alpha particles in air, Z. Bay and N. H. Seliger, Phys. Rev. **120,** No. 1, 141–143 (Oct. 1, 1960).

A test of a procedure for easy estimation of representative monthly electron density profiles for the ionosphere, J. W. Wright, J. Geophys. Research **65,** No. 10, 3215–3217 (Oct. 1960).

A method for efficiently providing low temperature liquids on a large scale to an accelerated experimental program, A. K. Stober, Proc. 10th Intern. Congress of Refrigeration, Copenhagen, Denmark **1,** No. 1, 17–18 (Pergamon Press Ltd., London, England, 1959).

Seasonal variations in the twilight enhancement of [OI] 5577, L. R. Megill, P. M. Jamnick and J. E. Cruz, J. Atmospheric and Terrest. Phys. **18,** 309–314 (Aug. 1960).

Synthetic mica, A. V. Valkenburg, Book, Encyclopedia of Chemical Technology, p. 480–487 (Interscience Encyclopedia, Inc., New York, N.Y., 1960).

Nonresonant microwave absorption and relaxation frequency at elevated pressures, A. A. Maryott and G. Birnbaum, J. Phys. Chem. **64,** No. 11, 1778–1780 (Nov. 1960).

Precipitation of the elements on addition of aqueous ammonia to their clear solution, J. I. Hoffman, Chem.-Anal. **49,** No. 3, 94 (Sept. 1960).

Low scatter high current gas target for D-D neutrons, A.

C. B. Richardson, Rev. Sci. Inst. **31,** No. 11, 1202–1203 (Nov. 1960).

The heat of combustion of dicyanoacetylene, G. T. Armstrong and S. Marantz, J. Phys. Chem. **64,** 1776–1777 (1960).

Errors in dielectric measurements due to a sample insertion hole in a cavity, A. J. Estine, and H. E. Bussey, IRE Trans. Microwave Theory and Tech. **MTT–8,** No. 6, 650–653 (Nov. 1960).

Ensemble method in the theory of irreversibility, R. Zwanzig, J. Chem. Phys. **33,** No. 5, 1338–1341 (Nov. 1960).

Determination of pentosans. Interlaboratory comparison of the aniline acetate, orcinol, and bromination methods, W. K. Wilson and J. Mandel, Tappi **43,** No. 12, 998–1004 (Dec. 1960).

A research for geomagnetic singular days, C. Warwick, T. Pohrte, and H. MacDonald, J. Geophys. Research **65,** No. 9, 3013–3015 (Sept. 1960).

Letter to editor of Revue Des Matériaux (first), E. S. Newman and H. A. Berman, Revue Des Matériaux C, No. 540, 231 (Dec. 1, 1960).

Geomagnetic storms and the space around the earth, S. Chapman, Nature **187,** No. 4740, 824–827 (Sept. 3, 1960).

On the theory of the critical point of a simple fluid, M. S. Green, J. Chem. Phys. **33,** No. 5, 1403–1409 (Nov. 1960).

Some implications of slant-E_s, E. K. Smith and R. W. Knecht, Polar Atmosphere Symp., Part 2, Ionospheric Section, Oslo, Norway, July 2–8, 1956, p. 195–204 (Pergamon Press, Inc., New York, N.Y., 1957).

Mismatch errors in microwave phase shift measurements, G. E. Schafer, IRE Trans. Microwave Theory and Tech. **MTT–8,** No. 617–622 (Nov. 1960).

Residual arc spectra of seventy elements diluted in copper, C. H. Corliss, W. F. Meggers and B. F. Scribner, Book, Colloquium Spectroscopicum Internationale **VIII,** 119–121 (1959).

The rotational constants of hydrogen chloride, E. K. Plyler and E. D. Tidwell, Z. Elektrochem. **64,** No. 5, 717–720 (Feb. 1960).

The minima of cyclic sums, K. Goldberg, J. London Math. Soc. 35, 262–264 (1960).

Normal approximation to the chi-square and non-central F probability functions, N. C. Severo and M. Zelen, Biometrika **47,** No. 3 & 4, 411–416 (1960).

Microtechnique for the infrared study of solids, diamonds, and sapphires as cell materials, E. R. Lippincott, F. E. Welsh, and C. E. Weir, Anal. Chem. **33,** 137–143 (Jan. 1961).

Definitions relating to metals and metalworking, M. R. Meyerson and S. J. Rosenberg, Am. Soc. Metals Handb. **1,** 1–41 (1961).

Stress-rupture tests at 1350° F on type 304 stainless steel, W. D. Jenkins, W. A. Willard and W. J. Youden, ASTM Bull. **1,** No. 2, 104–108 (Feb. 1961).

Paratellurite, a new mineral from Mexico, G. Switzer and H. E. Swanson, Am. Mineralogist **45,** 1272 (Nov.–Dec. 1960).

The nature, cause, and effect of porosity of electrodeposits VI. Note on a magnetic method of detecting corrosion currents, F. Ogburn and W. H. Roberts, Plating **48,** No. 2, 168–169 (Feb. 1961).

The height of maximum luminosity in an auroral arc, F. E. Roach, J. G. Moore, E. C. Bruner, Jr., H. Cronin, and S. M. Silverman, J. Geophys. Research **64,** No. 11, 3575–3580 (Nov. 1960).

Physical metallurgy and mechanical properties of materials: Ductility and the strength of metallic structures, J. M. Frankland, J. Eng. Mech. Div. Proc. Am. Soc. Civil Eng. **86,** No. EM 6, 45–52 (Dec. 1960).

Cryogenic impurity adsorption from hydrogen, M. J. Hiza, Chem. Engr. Progress **55,** No. 10, 68–71 (Oct. 1960).

Nomenclature for standards of radioactivity, A. G. McNish, Intern. J. Appl. Radiation and Isotopes **8,** 145–146 (Jan. 1960).

Lithium, M. R. Meyerson, Am. Soc. for Metals Handbook **1,** 1213 (1961).

Tensile cryostat for the temperature range 4° to 300° Kelvin, R. M. McClintock and K. A. Warren, ASTM Bull. **1,** No. 2, 95–98 (Feb. 1961).

A radio-frequency permittimeter, R. C. Powell and A. L. Rasmussen, IRE Trans. Instrumentation **I–9,** No. 2, 179–184 (Sept. 1960).

Subgroups of the modular group and sums of squares, H. Newman, Am. J. Math. **82,** No. 4, 761–778 (Oct. 1960).

Phase equilibria in the system cadmium oxide-niobium oxide, R. S. Roth, J. Am. Ceram. Soc. **44,** No. 1, 49–50 (Jan. 1961).

Redetermination of the chromium and nickel solvuses in the chromium-nickel system, C. J. Bechtoldt and H. C. Vacher, Trans. Metallurgical Soc., Am. Inst. Mining Engrs. **221,** 14–18 (Feb. 1961).

A modulated subcarrier technique of measuring microwave phase shifts, G. E. Schafer, IRE Trans. Instrumentation **I–9,** No. 2, 217–219 (Sept. 1960).

Hydrogen-bonding in calcium-deficient hydroxyapatites, A. S. Posner, J. M. Stutman, and E. R. Lippincott, Nature **188,** No. 4749, 486–487 (Nov. 1960).

Hydrogen sulfide precipitation of the elements from 0.2–0.5 normal hydrochloric acid, J. I. Hoffman, Chemist Analyst **50,** No. 1, 30 (Mar. 1961).

Dielectric constant and dielectric loss of TiO_2 (Rutile) at low frequencies, R. A. Parker and J. H. Wasilik, Phys. Rev. **120,** No. 5, 1631–1637 (Dec. 1960).

Generating functions for formal power series in non-commuting variables, K. Goldberg, Proc. Am. Math. Soc. **11,** No. 6, 988–991 (Dec. 1960).

Tests for regression coefficients when errors are correlated, M. M. Siddiqui, Ann. Math. Stat. **31,** No. 4, 929–938 (Dec. 1960).

Application of the method of polarized orbitals to the scattering of electrons from hydrogen, A. Temkin and J. C. Lamkin, Phys. Rev. **121,** No. 3, 788–794 (Feb. 1961).

On the absorption spectrum of CF_2 and its vibrational analysis, D. E. Mann and B. A. Thrush, J. Chem. Phys. **33,** No. 6, 1732–1734 (Dec. 1960).

Standards and measurements of microwave surface impedance, skin depth, conductivity and Q, H. E. Bussey, IRE Trans. Instrumentation **I–9,** No. 2, 171–175 (Sept. 1960).

Plating gun bores, V. A. Lamb and J. P. Young, Ordnance **XLV,** No. 245, 725–727 (Mar.–Apr. 1961).

Integrated starlight over the sky, F. E. Roach and L. R. Megill, Astrophys. J. **133,** No. 1, 228–242 (Jan. 1961).

Low temperature static seals using elastomers and plastics, D. H. Weitzel, R. F. Robbins, G. R. Bopp, and W. R. Bjorklund, Rev. Sci. Inst. **31,** No. 12, 1350–1351 (Dec. 1960).

Electrodeposition of metals from nonaqueous media, A. Brenner, Encyclopedia of Chemical Technology, 2nd Suppl., 315–324 (Interscience Encyclopedia 1960).

FM and SSB radiotelephone tests on a VHF ionospheric scatter link during multipath conditions, J. W. Koch, W. B. Harding, and R. J. Jansen, IRE Trans. Commun. Systems **CS–8,** No. 3, 183–186 (Sept. 1960).

Absolute measurement of temperatures of microwave noise sources, A. J. Estin, C. L. Trembath, J. S. Wells, and W. C. Daywitt, IRE Trans. Instrumentation **I–9,** No. 2, 209–213 (Sept. 1960).

Electron scattering in high magnetic field, A. H. Kahn, Phys. Rev. **119,** No. 4, 1189–1192 (Aug. 1960).

Measurement of reflections and losses of waveguide joints and connectors using microwave reflectometer techniques, R. W. Beatty, G. F. Engen, and W. J. Anson, IRE Trans. Instrumentation **I–9,** No. 2, 219–226 (Sept. 1960).

Microwave spectrum of cis-difluoroethylene, V. W. Laurie, J. Chem. Phys. **34,** No. 1 (Jan. 1961).

Surface roughness of gold castings, J. J. Barone, R. L. Huff, and G. Dickson, Dental Progr. **1,** No. 2, 78–84 (Jan. 1961).

The sensitivity of photographic film to 3-mev neutrons and to thermal neutrons, M. Ehrlich, Health Phys. **4,** 113–128 (1960).

A prototype rubidium vapor frequency standard, R. J. Carpenter, E. C. Beaty, P. L. Bender, S. Saito, and R. O. Stone, IRE Trans. Instrumentation **I–9,** No. 2 (Sept. 1960).

Low even configurations in the first spectrum of thorium (Th I), R. E. Trees, Physica **26,** 353–360 (1960).

Comparison measurements with intensity standards for high energy bremsstrahlung, J. S. Pruitt and W. Pohlit, Z. Naturforschung **15b,** No. 9, 617–619 (1960).

High-dispersion spectra of Jupiter, C. C. Kiess, C. H. Corliss and H. K. Kiess, Astrophys. J. **132,** No. 1, 221–231 (July 1960).

Propagation of electromagnetic waves along a thin plasma sheet, J. R. Wait, Can. J. Phys. **38,** 1586–1594 (1960).

Preparation and properties of aromatic fluorocarbons, W. J. Pummer and L. A. Wall, J. Chem. Engrs. Data **6,** No. 1, 76–78 (Jan. 1961).

Stability of thermoset plastics at high temperatures, S. L. Madorsky and S. Straus, Modern Plastics **38,** 134–140 (Feb. 1961).

Immiscibility and the system lanthanum oxide boric-oxide, E. M. Levin, C. R. Robbins, and J. L. Waring, J. Am. Ceram. Soc. **44,** No. 2, 87–91 (Feb. 1961).

On the properties of the vapor pressure curve, E. H. Brown, Cryogenics **1,** No. 1, 37–40 (Sept. 1960).

Absorption and scattering of photons by holmiun and erbium, E. G. Fuller and E. Hayward, Proc. Intern. Conf. Nuclear Structure, 761–766 (Kingston, Canada, 1960).

Spectroscopy of fluorine flames. I. Hydrogen-fluorine flame and the vibration-rotation emission spectrum of HF, D. E. Mann, B. A. Thrush, D. R. Lide, J. J. Ball, and N. Acquista, J. Chem. Phys. **34,** No. 2, 420–431 (Feb. 1961).

**Publications for which a price is indicated (except for NBS Technical Notes) are available only from the Superintendent of Documents, U.S. Government Printing Office, Washington 25, D.C. (foreign postage, one-fourth additional). Technical Notes are available only from the Office of Technical Services, U.S. Department of Commerce, Washington 25, D.C. (Order by PB number). Reprints from outside journals and the NBS Journal of Research may often be obtained directly from the authors.*

UNITED STATES
GOVERNMENT PRINTING OFFICE
DIVISION OF PUBLIC DOCUMENTS
WASHINGTON 25, D.C.

OFFICIAL BUSINESS

PENALTY FOR PRIVATE USE TO AVOID
PAYMENT OF POSTAGE, $300
(GPO)

JOURNAL OF RESEARCH of the National Bureau of Standards Vol. 65C, No. 3 July–September 1961
C. Engineering and Instrumentation

Contents

	Page
Prediction of symptoms of cavitation. Robert B. Jacobs.	147
Heating and cooling of air flowing through an underground tunnel. B. A. Peavy.	157
Stress-corrosion cracking of the AZ31B magnesium alloy. Hugh L. Logan.	165
Coatings formed on steel by cathodic protection and their evaluation by polarization measurements. W. J. Schwerdtfeger and Raul J. Manuele.	171
Calibration of inductance standards in the Maxwell-Wien bridge circuit. Thomas L. Zapf.	183
Calibration of loop antennas at VLF. A. G. Jean, H. E. Taggart, and J. R. Wait.	189
Location of the plane of best average definition with low contrast resolution patterns. Francis E. Washer and William P. Tayman.	195
Influence of temperature and relative humidity on the photographic response to Co^{60} gamma radiation. Margarete Ehrlich.	203
Publications of the National Bureau of Standards.	207

For sale by the Superintendent of Documents, U.S. Government Printing Office, Washington 25, D.C. Price 75 cents (single copy)
Subscription price: $2.25 a year; 50 cents additional for foreign mailing.
UNITED STATES GOVERNMENT PRINTING OFFICE, WASHINGTON 1961